Inclusive *b*-jet production cross section measurement at LHCb

Alessandro Camboni

Inclusive b-jet production cross section measurement at LHCb

Alessandro Camboni

Departament d'Estructura i Constituents de la Matèria
Facultat de Física
Universitat de Barcelona

Memòria per a optar al títol de
Doctor en Física
per la Universitat de Barcelona

11 de Febrer de 2013

Directors de tesi:
Eugeni Graugés Pous
Cédric Potterat

Programa de Doctorat de Física de l'EEES

A Carlo e Mariella.
E a Riccardo:

Prus bellus ant a essi is bisus tuus de pipiu,
prus bellu at a essi a ddus lompi cun is fortzas tuas.

Acknowledgements

This achievement has been made possible thanks to the contribution of many people, they all deserve my gratitude.

I'm especially grateful to my advisor Eugeni, the first person I met in Barcelona (it was kind of an imprinting!) and who never ceased to guide and encourage me during this challenging climb. I'm equally thankful to my co-advisor Cédric for working with me side by side many times (I raise the first cup of that great Potterat wine bottle to you!). I thank you both for all you have taught me and for convincing me every time that my work were deserving. It is safe to say I would not have achieved all that I have without you.

A big credit goes to Marco Musy, who led me for a significant part of the journey. Thank you for your big effort and patience in showing me the route.

I would like to say a big thanks to Lluís Garrido, the Boss, to make my wish possible, believing in me y por recordarme siempre que "hay que ponerse las pilas!", gràcies per això també!

My gratitude goes also to Clara Matteuzzi and Marcin Kucharczyk, who shared with me the most of the analysis: thank you a lot for all I have learned with you and for the enthusiasm and passion you put into our work.

I cannot fail to mention the fruitful, enthusiastic and sometimes "hot" discussions with Ricardo Graciani y Hugo Ruiz: thank you very much for your helpful collaboration to the successful outcome of this work.

Grazie sincero a Xavi Vilasis, por traer su buen humor al despacho del CERN e per las tantas *muertes por penne* en la Meyrinoise!

El pensamiento siguiente va a los amigos y compañeros de viaje, quien también han tenido un papel importante en el desarrollo de este trabajo.

Gracias a Ricci, por su disponibilidad constante, por comerse el marrón del SPD y por sus increibles tortillas y empanadas. A Albert, por sus inmensos conocimientos sobre cosas frikis, y quien cualquier cosa haga es un crack (las pistas de fútbol lo han perdido demasiado prematuramente tras el sacrificio de órganos importantes). A Jordi, que cal reconèixer que sempre té raó, pels *pizza thursdays* al pis i po bòlliri imparai su sardu. A Carlos, mi primera guía espiritual en este país, gracias por no dejar nunca de animarme y perseguirme. A Marc, por compartir conmigo escuelas y congresos, y sobre todo las escapadas durante ellos. A Elías por sus fuets de Girona y por su paciencia en introducirme al python. A Antonio, por asegurar que siempre estuviera alguien en el piso-búnker de Meyrin. Gracias a Miriam, por ser el único ejemplar de mujer que nunca he visto en ese piso. A Vicente, último heredero viviente del grupo de doctorandos: la história está en buenas manos.

Mil gracias al resto del grupo del altas energías de la UB: Edu, Albert, David, Adrià, Juan, Andreu, gracias por compartir muchos buenos momentos en la uni y en el CERN, y por la tantas discusiones entretenidas sobre cualquier cosa excepto la física.

Mis agradecimientos también van al resto de la gente que ha pasado por la UB. Gracias en particular a Arianna, per la vita dentro e fuori la UB, lo sai che non ti cambierei neanche per un *mijone de euro*! A la peña futbolera: Bruno, Dani, Octavi, Alessio, Carles, Juan, Xavi, Arnau, gracias por demostrar que ser físicos y a la vez buenos futbolistas es posible, recordaré esas temporadas como las mejores de mi carrera deportiva, vaya partidazos! A Miguel, para mí el verdadero y único ganador del concurso de frikis, por mostrar que cada peli puede ser un *peliculón*! A Clemens, latino nacido por casualidad en Regensburg, ganador de la carrera de caracoles, gracias por el *renormalón* y por poder contar con tu amistad a pesar de la distancia. A Ana y Carla, por hacer mucho más agradables las comidas en la uni. Gracias a la hermosa Estela de Aragón, por traer su amabilidad a ese pasillo y por sus pasos de samba. Gracias a mis compañeros de despacho Jaume y Juan por compartir estos largos años juntos.

La história de este logro no se puede separar de la vida pasada en Barcelona durante estos años. Tando gràtzias dae coro a sa cricca de *sos malos a ghirare*: Giamp, Putzu, Lovicu, Gabriele, Pux, Carboni, Simoneddu, Antonello, Bellinzis, gràtzias pro s'amistade bostra, chena de boisàteros su figadu diat èssere prus sanu ma sa vida unu scallonamentu! A Claudia, gràtzias po m'ascurtai sempri e mi donai cunsillus e agiudu, in pagu fueddus gràtzias po essi amiga e Tzia in su pròpiu tempus! Grazie di cuore ad Alessandra, mio alterego femminile, per tutte le ore passate a sorbirsi i miei problemi e per le

altrettante ore passate a sommergermi dei suoi! Gracias a Marta y Sheila por las tantas salidas, comidas, cenas, fiestas, *grazie mille*! Gràcies a Pau, millor català de l'any! Gràtzias a Frantziscu, Andreina, Cinzia e Alessandra de Biddesorris, e grazie a Giuseppe, compagni di fiesta ma soprattutto amici su cui poter contare. Grazie a Eloisa, per mostrare che è possibile essere una persona "più bella dentro che fuori" a quei livelli di hermosura! Ricorda, soprattutto per questo un sardo è per sempre!

Grazie agli amici fraterni di Iglesias, Marco, Matteo, Lorga, Spu, Sku, Stefano, Massi per esserci sempre. Le scuse per fare insieme qualche *calling* ci saranno sempre! Per chi sa, raggiungere con voi il *Cingommone* è un privilegio oltre che un'esperienza mistica.

Grazie a Giamba, per condividere tanti interessi, stati d'animo, elasticizzazione nel programmare e per mantenere un canale di comunicazione aperto 24/7. Vite e conquiste parallele nello studio e nel fantacalcio.

Gràtzias meda a Robi, zenia de fradili, ma in antis de totu amigu: gràtzias po s'agiudu, po is garas de *lanzamiento a la diana*, su bogavante, e totu is atrus momentus spassiosus in Barna e in Girona.

A sa Terra e a sa genti mia, cumentzu e acabu de su chi seu deu.

Infine, i miei cari. Grazie a zia Luisa e zio Vì, a Carlo e Ale, per tutto il sostegno e l'affetto che mi date sempre. Grazie alle mie care sorelle Anna e Ari, grazie per essermi sempre vicine anche da così lontano, come io lo sarò sempre per voi. Grazie a Matteo per avermi dato con Ari quella meraviglia di nipotino che è Ricky, gioia e nuova luce per tutti noi. Un pensiero speciale a nonna Margherita: non sei riuscita a vedermi raggiungere questo traguardo, ma ti ho portato sempre con me. Grazie ai miei amati mamma e papà, questo traguardo lo devo a voi ed è per voi, è il mio modo per ringraziarvi per tutto l'amore e l'appoggio che mi date.

Contents

1 Introduction

Everything in the world that we can directly experience is made of matter particles. They can be classified in two basic types, called quarks and leptons.

Each group consists of six particles, which are related in pairs, or *generations*. All stable matter in the universe is made from particles that belong to the first generation, made up by the lightest and most stable particles. Any heavier particles quickly decay to the next most stable level. The heavier and less stable particles belong to the second and third generations.

The six quarks are paired in three generations – the *up* and the *down* quark form the first generation, followed by the *charm* and the *strange* quark, then the *top* and the *bottom* quark. The six leptons are similarly arranged in three generations – the *electron* and the *electron-neutrino*, the *muon* and the *muon-neutrino*, and the *tau* and the *tau-neutrino*. The electron, the muon and the tau all have an electric charge and a mass, whereas the neutrinos are electrically neutral with very little mass.

Particles interact with each other through four fundamental forces: the *strong* force, the *weak* force, the *electromagnetic* force, and the *gravitational* force. They act over different ranges and with different strengths. The weakest force is gravity, but it has an infinite range. The electromagnetic force also has infinite range, but it is many times stronger than gravity. The weak and strong forces are effective only over a very short range and dominate at the level of subatomic particles. Despite its name, the weak force is much stronger than gravity but it is indeed the weakest of the other three. The strong force is the strongest among all the four fundamental interactions.

We know from experimental evidences that three of the fundamental forces result from the exchange of force carrier particles, which belong to a group

called *bosons*. Matter particles transfer discrete amounts of energy by exchanging bosons with each other. Each fundamental force has its own corresponding boson particle – the strong force is carried by the *gluon*, the electromagnetic force is carried by the *photon*, and the W and Z bosons are responsible for the weak force. Although not yet found, the *graviton* should be the corresponding force-carrying particle of gravity.

Each fundamental interaction is described in physics by a single theory: chromodynamics, flavourdynamics, electrodynamics, and Einstein's general theory of relativity. The Standard Model of Elementary Particles Physics is the theory which describes the fundamental particles and their interactions in nature. It incorporates the strong, the electromagnetic and the weak force, but does not explain gravitation. While its theoretical formulation was finalized in the 1970's, experimental confirmation of some of its predictions, like the top quark and the tau neutrino, had to wait until the end of the century. The last key piece predicted by the Standard Model, the *Higgs* boson, still remains to be experimentally confirmed, although serious clues of its existence have been recently shown by the CERN [1, 2]. The Standard Model is described in Chap. 2.

The LHCb experiment is one of the four main experiments of the Large Hadron Collider situated at CERN, and it is dedicated to the study of CP violation and rare decays in the B sector. It has peculiar features which makes it stand out with respect to the general-purpose LHC detectors, ATLAS and CMS. Its excellent capability of vertex identification can be exploited for a variety of studies beyond its main purposes. A description of the main features of the LHCb detector is given in Chap. 3.

This thesis describes the measurement of the production cross section of b quarks in proton-proton collisions. The data analyzed are those collected by the LHCb detector in 2010 with a centre-of-mass energy of $\sqrt{s} = 7\,\text{TeV}$. Chap. 4 shows the theoretical predictions of the production of b quarks and hadrons in such collisions as implemented in the Monte Carlo simulations.

The measurement is made by reconstructing hadronic jets associated to the hadronization of b quarks, through the identification of the characteristic displaced secondary vertex of the decay of the B hadron. The jet reconstruction algorithm is detailed in Chap. 5.

Chap. 6 is devoted to the estimation of the composition of the selected data sample with Monte Carlo techniques. Finally the $b\bar{b}$ production cross section is calculated, and the conclusions and an outlook for the next future are given.

2 The Standard Model

Over the last century, theories and discoveries on the fundamental structure of matter have led to a remarkable statement: everything that is visible in the Universe is made from twelve basic constituents called fundamental particles, governed by four fundamental forces. The dynamics of these fundamental particles under the influence of electromagnetic, weak and strong interactions is extremely well described by the relativistic quantum field theory known as Standard Model of elementary particle physics (SM). It has successfully explained plenty of experimental results and precisely predicted a wide variety of phenomena. SM has recently incorporated the physics of neutrino mass, mixing and oscillations [3], by now widely demonstrated by several experiments [4, 5].

Nevertheless the Standard Model falls short of being a complete theory of fundamental interactions, since it does not incorporate the physics of dark energy [6] nor the full theory of gravitation as described by general relativity. Other significant limitations of the Standard Model concern the strong CP problem [7] and the hierarchy problem [8].

The three fundamental forces are brought together in the language of gauge theories. Invariance of the Standard Model to the Poincaré global symmetry group, *i.e.* translations, rotations and boosts in spacetime, leads naturally to the classical physics conservation laws for energy, momentum and angular momentum, by Noether's theorem. The conserved charges of the electromagnetic, weak and strong forces result from invariance of the Standard Model to the local symmetry group: $\mathrm{SU(3)_C} \otimes \mathrm{SU(2)_W} \otimes \mathrm{U(1)_Y}$, where C represents the color charge of the strong force, W the isospin and Y the hypercharge of the unified electroweak interaction. The electric charge Q is also conserved and it

is derived from the hypercharge and the weak isospin, $\mathrm{Q} = \mathrm{W}_3 + \mathrm{Y}$.

The symmetry group has 12 generators that give rise to all the force mediators: the eight gluons g of the strong force, the three weak vector bosons, W^+, W^- and Z^0, and the single photon γ of the electromagnetic interaction.

The Standard Model Lagrangian can be summarised as:

$$\mathcal{L}_{\mathrm{SM}} = \mathcal{L}_{\mathrm{kin}} + \mathcal{L}_{\mathrm{em}} + \mathcal{L}_{\mathrm{c}} + \mathcal{L}_{\mathrm{n}} + \mathcal{L}_{\mathrm{YM}} + \mathcal{L}_{\mathrm{Higgs}} + \mathcal{L}_{\mathrm{Yukawa}} \ , \tag{2.1}$$

where:

- $\mathcal{L}_{\mathrm{kin}}$ is the free fermion lagrangian, the simplest Lagrangian for a free, massless, fermion field $\psi(x)$, containing just a kinetic term;
- $\mathcal{L}_{\mathrm{em}}$ is the electromagnetic coupling term;
- $\mathcal{L}_{\mathrm{c}}$ is the charged-current interaction term;
- $\mathcal{L}_{\mathrm{n}}$ is the neutral-current interaction term;
- $\mathcal{L}_{\mathrm{YM}}$ is the Yang-Mills lagrangian, following from the requirement of local $\mathrm{SU}(2) \times \mathrm{U}(1)$ gauge invariance;
- $\mathcal{L}_{\mathrm{Higgs}}$ is the term provided by the Higgs sector;
- $\mathcal{L}_{\mathrm{Yukawa}}$ is the Yukawa coupling term.

Along with the boson force mediators with integer spin, the other point-like constituents of matter with no known substructure up to the present limits of 10^{-18} – 10^{-19} m are known as fermions of spin $\mathrm{s} = \frac{1}{2}$ and are classified into leptons and quarks. The known leptons are: the electron e^- , the muon μ^- and the τ^- with electric charge $\mathrm{Q} = -1$ (all charges are given in units of the elementary charge e); and the corresponding neutrinos ν_e , ν_μ and ν_τ with $\mathrm{Q} = 0$. The known quarks are of six different flavours: u, d, s, c, b and t and have fractional charge $\mathrm{Q} = \frac{2}{3}, -\frac{1}{3}, -\frac{1}{3}, \frac{2}{3}, -\frac{1}{3}, \frac{2}{3}$ respectively.

A short outline of the Electroweak (EW) theory will be now given, before going through a more detailed review of Quantum Chromodynamics.

The proposal of the symmetry group for the EW Theory, $\mathrm{SU}(2) \otimes \mathrm{U}(1)$, was done by Glashow in 1961 [9] in his attempt to unify weak and electromagnetic interactions into a symmetry group that contained $\mathrm{U}(1)_{em}$. Another key ingredient for the building of the Electroweak Theory is provided by the Goldstone Theorem, which was initiated by Nambu in 1960 and proved and studied with generality by Goldstone in 1961, and by Goldstone, Salam and Weinberg

in 1962 [10]. This theorem states the existence of massless spinless particles as an implication of spontaneous symmetry breaking of global symmetries. The spontaneous symmetry breaking of local (gauge) symmetries, needed for the breaking of the electroweak symmetry was studied by P. Higgs *et al.* [11]. The present formulation of the Electroweak Theory was developed by Weinberg in 1967 and by Salam in 1968, who incorporated the idea of unification of Glashow.

The gauge bosons of the group (B, W^1 , W^2 and W^3) are all massless. A scalar Higgs field is introduced in order to break the symmetry of the group spontaneously. The coupling of the gauge bosons with the Higgs field results in the massive $W^{\pm}$ and Z^0 bosons. It also results in the entangling of the SU(2) and U(1) groups as the Z^0 boson and the photon are linear combinations of the massless B and W^3 bosons. This is shown in equations 2.2, where θ_{W} is the weak mixing angle.

$$\begin{aligned} Z &= \quad W^3 \cos\theta_{\mathrm{W}} - B \sin\theta_{\mathrm{W}} \\ \gamma &= \quad B \cos\theta_{\mathrm{W}} + W^3 \sin\theta_{\mathrm{W}} \ . \end{aligned} \tag{2.2}$$

The weak eigenstates of the quarks are superpositions of the mass eigenstates of the physical quarks. This means that quark transitions across generations are possible via the weak interaction. The mixing of the mass and weak eigenstates is described by the Cabibbo-Kobayashi-Maskawa (CKM) matrix [12].

2.1 Quantum Chromodynamics

Quantum Chromodynamics (QCD) is the gauge theory for strong interactions that bind quarks together. QCD also mediates the forces between hadrons and thus controls the formation of nuclei. The fundamental properties of QCD cannot be directly tested, since it is a non-linear theory that is not analytically solvable, but plenty of indirect evidences supports this theory. Unlike weaker quantum field theories such as electromagnetism, for which perturbation expansions in the interaction strength give very accurate results, QCD interaction is so strong that perturbative approximations often fail. Consequently, few precise predictions can be made from the theory.

The non-Abelian gauge group of QCD is SU(3), whose associated charge is called colour. The six flavours of quarks belong to the fundamental representation of this group, which for a gauge group SU(N_c) has dimension N_c; therefore N_c is called the number of colours and quarks are then said to have

3 different colours. The gauge bosons mediating the colour interaction are called gluons, they are massless and transform like connections in the adjoint representation. This representation having dimension $N_c^2 - 1$, QCD possesses 8 gluons.

The QCD invariant Lagrangian is built applying the gauge principle with the particularities of the non-abelian group SU(3) taken into account. The global symmetry SU(3) of the Lagrangian for the strong interactions is promoted to local by replacing the derivative of the quark by its covariant derivative which in the QCD case is,

$$\mathbf{D}_\mu \psi = (\partial_\mu \mathbf{I} + i g_s \mathbf{T}^a A_\mu^a)\psi \ , \tag{2.3}$$

where ψ and A_μ^a are the quark and gluon fields, g_s is the gauge coupling parameter which is related to the strong coupling constant by $\alpha_s = \frac{g_s^2}{4\pi}$, $\mathbf{T}^a$ are the generator matrices. The QCD Lagrangian density $\mathcal{L}_{\mathrm{QCD}}$ (related to the Lagrangian L by $L = \int dV \mathcal{L}$) is then written in terms of the quarks and their covariant derivatives and contains in addition the kinetic term for the gluon fields:

$$\mathcal{L}_{\mathrm{QCD}} = -\frac{1}{4} F_{\mu\nu}^a F_a^{\mu\nu} + \sum_f i\bar{\psi}_f (\gamma^\mu \mathbf{D}_\mu - m_f \mathbf{I})\psi_f \ , \tag{2.4}$$

f being the flavour index ($f = u, d, c, s, t, b$), m_f the mass of the quark, and the gauge invariant gluon field strength tensor is

$$F_{\mu\nu}^a = \partial_\mu A_\nu^a - \partial_\nu A_\mu^a - g_s f^{abc} A_\mu^b A_\nu^c \ , \tag{2.5}$$

which contains a bilinear term in the gluon fields since it corresponds to a non-abelian gauge theory with structure constants f^{abc} ($a, b, c = 1, \ldots, 8$), defined by the commutator of its generators $\mathbf{T}^a$ in the fundamental representation as

$$\left[\mathbf{T}^a, \mathbf{T}^b\right] = i f^{abc} \mathbf{T}^c \ . \tag{2.6}$$

The Lagrangian defines the quark and gluon interactions and their propagators.

Neither quarks nor gluons are observed as free particles. Hadrons are color-singlet (*i.e.* color-neutral) combinations of quarks, anti-quarks, and gluons. The Feynman rules for the propagators and interaction vertices are determined directly from the Lagrangian. The rules are only useful within the context of perturbation theory, which requires the strength of the coupling to be small. The gluon kinetic term $F_{\mu\nu}^a F_a^{\mu\nu}$ contains a three and a four gluon interaction

term: these are precisely the self-interaction gluon vertices which are genuine of a non-abelian theory.

2.1.1 Renormalization and running coupling

QCD is a renormalizable theory, hence the number of superficially divergent amplitudes is finite and these divergences can be absorbed by replacing the bare parameters of the QCD Lagrangian (Eq. 2.4), *i.e.* the bare coupling g_{B} and the fermion masses $m_{f\mathrm{B}}$, with the renormalized parameters measured at an (unphysical) arbitrary scale μ_R, the *renormalization scale*.

The requirement that physical observables need to be independent of the renormalization scale is at the base of the concept of the renormalization group and gives predictive power to the procedure of renormalization. This is achieved through a set of renormalization group equations that specify the running of the renormalized parameters as a function of the energy.

When one takes μ_R close to the scale of the momentum transfer Q in a given process, then $\alpha_s(\mu_R^2 \simeq Q^2)$ is indicative of the effective strength of the strong interaction in that process. The relevant renormalization group equation (RGE) yielding the energy dependence can be derived from the Callan-Symanzik equation [13]. The RGE for α_s then reads, considering only massless fermions

$$\mu_R^2 \frac{\partial \alpha_s}{\partial \mu_R^2} = \beta(\alpha_s) \ , \tag{2.7}$$

where we have implicitly defined the so-called β-function of QCD, which can be computed perturbatively order-by-order by calculating the relevant Green functions and can in general be expressed as an expansion in the coupling. For further convenience and in order to fix our notation, we write this expansion as

$$\beta = -2\alpha_s \left(\frac{\alpha_s}{4\pi}\beta_0 - \frac{\alpha_s^2}{(4\pi)^2}\beta_1 + \dots \right) \ . \tag{2.8}$$

It can be shown that in a mass-independent regularization scheme the β-function is gauge independent [14] and its first two coefficients β_0 and β_1 turn out not to depend on the particular mass-independent scheme adopted. From the calculation of the relevant one-loop diagrams, shown in Fig. 2.1, one gets the value of the first β-function coefficient [15]:

$$\beta_0 = \frac{2}{3}T_f N_f - \frac{11}{6}C_A = \frac{2N_f - 11N_c}{6} \ , \tag{2.9}$$

where $C_A = N_c$, N_f is the number of active quark flavours, *i.e.* those that

can be considered massless at the energy scale considered, and there is a trivial SU(3) factor, $T_f = \frac{1}{2}$. The positive contribution proportional to N_f is generated by the q-$\bar{q}$ loops and corresponds to the Quantum Electrodynamics (QED) case (except for the T_f factor). The gluonic self-interactions introduce the additional negative contribution proportional to N_c. This second term is responsible for the completely different behaviour of QCD: $\beta_0 < 0$ if $N_f < 16$.

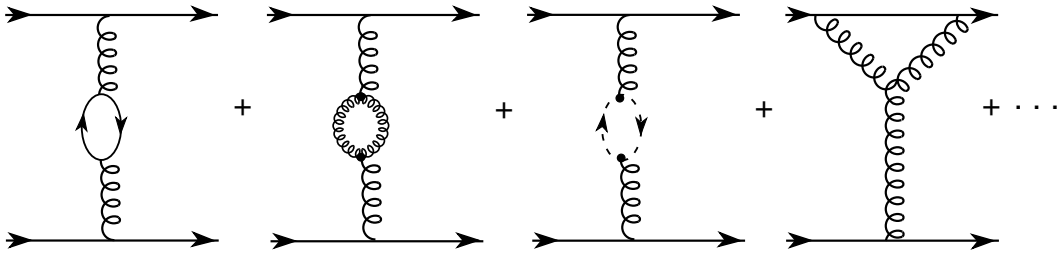

Figure 2.1: Feynman diagrams contributing to the renormalization of the strong coupling.

Truncating Eq. 2.8 to its leading order term β_0 leads to a simple approximate solution of the renormalization group equation (Eq. 2.7). It reads

$$\alpha_s(Q^2) = \frac{\alpha_s(\mu_R^2)}{1 + \beta_0 \frac{\alpha_s(\mu_R^2)}{\pi} \log \frac{Q^2}{\mu_R^2}} \ , \tag{2.10}$$

that decreases at short distances, *i.e.*

$$\lim_{Q^2 \to \infty} \alpha_s(Q^2) = 0 \ . \tag{2.11}$$

Thus, for $N_f \leq 16$, QCD has indeed the required property of *asymptotic freedom*. The gauge self-interactions of the gluons spread out the QCD charge, generating an antiscreening effect. This could not happen in QED, because photons do not carry electric charge. Only non-abelian gauge theories, where the intermediate gauge bosons are self-interacting particles, have this antiscreening property [16].

Although quantum effects have introduced a dependence with the energy, we still need a reference scale to decide when a given Q^2 can be considered large or small. An obvious possibility is to choose the scale at which α_s enters into a strong-coupling regime (*i.e.* $\alpha_s \sim 1$), where perturbation theory is no longer valid. A more precise definition can be obtained from the solution of

the β-function differential equation (Eq. 2.7). At one loop, one gets

$$\ln \mu_R + \frac{\pi}{\beta_0 \alpha_s(\mu_R^2)} = \ln \Lambda_{\mathrm{QCD}} \ , \tag{2.12}$$

where Λ_{QCD} is the scale which causes the coupling $\alpha_s(\Lambda_{\mathrm{QCD}})$ to diverge, thus bringing to a breakdown of perturbation theory. When $\mu_R \gg \Lambda_{\mathrm{QCD}}$, $\alpha_s(\mu_R^2) \to 0$, so that we recover asymptotic freedom. At lower energies the running coupling gets bigger; for $\mu_R \to \Lambda_{\mathrm{QCD}}$, $\alpha_s(\mu_R^2) \to \infty$ and perturbation theory breaks down. Processes such as heavy quark production occurring at an energy scale significantly above Λ_{QCD} can be handled by perturbative means. The scale Λ_{QCD} indicates when the strong coupling blows up. Eq. 2.12 suggests that confinement at low energies is quite plausible in QCD; however, it does not provide a proof because perturbation theory is no longer valid when $\mu_R \to \Lambda_{\mathrm{QCD}}$.

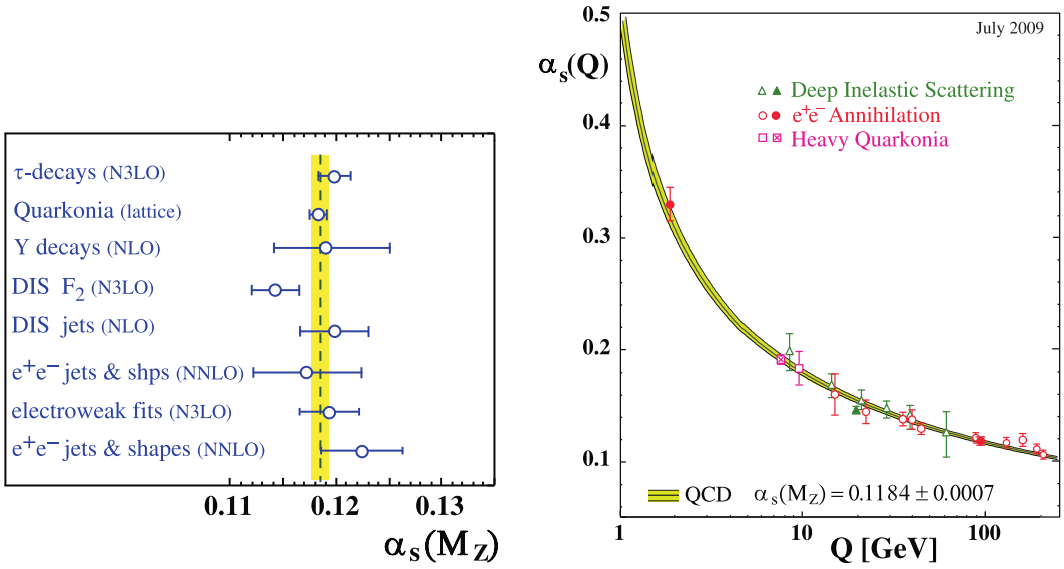

Figure 2.2: *Left*: Summary of measurements of $\alpha_s(M_{Z^0})$, used as input for the world average value. *Right*: Summary of measurements of α_s as a function of the respective energy scale Q. Both plots are taken from [17].

A recent world average [17] of various different measurements of α_s yields $\alpha_s(M_{Z^0}) = 0.1184 \pm 0.0007$, whose corresponding value for the QCD scale is $\Lambda^{(5)}_{\mathrm{QCD}} = (213 \pm 9)\,\mathrm{MeV}$, where the (5) apex signifies that five flavours of quarks (the up, down, strange, charm and bottom) have been considered massless at the mass $M_{Z^0} = 91.2\,\mathrm{GeV}$ of the neutral Z^0 boson. This value of α_s and Λ_{QCD} where obtained using the QCD β-function and its corresponding running

coupling up to 4 loops [18, 19].

Fig. 2.2 summarizes the measurements of α_s: the right plot provides a strong evidence for the correct prediction by QCD of the scale dependence of the strong coupling.

2.2 Heavy quark production and hadronization

Free quarks are never observed, *i.e.* a quark never exists on its own for a time longer than $\sim 1/\Lambda_{\rm QCD}$: up, down, strange, charm, and bottom quarks all hadronize, *i.e.* become part of a meson or baryon, on a timescale $\sim 1/\Lambda_{\rm QCD}$; the top quark instead decays before it has time to hadronize. Hence QCD final states always consist of hadrons, while perturbative QCD calculations deal with partons. Physically, an energetic parton fragments (*"showers"*) into many further partons, which then, on later timescales, undergo a transition to hadrons (*"hadronization"*). Fixed-order perturbation theory captures only a small part of these dynamics. Instead models are used to represent hadronization and are implemented in Monte Carlo (MC) generators.

The light u, d and s quarks can be obtained from a number of sources: valence flavours in hadronic beam particles, perturbative subprocesses and nonperturbative hadronization. Therefore the information carried by identified light hadrons is highly ambiguous. The characteristic that sets the b apart is its heaviness,

$$m_b \gg \Lambda_{\rm QCD} \ , \tag{2.13}$$

that implies that b quarks are not expected to be produced at any significant rate in non-perturbative processes [20]. If one is interested in the phenomenology of the decays of the b-flavoured hadrons, Eq. 2.13 suggests to treat the b as infinitely heavy in comparison with its companion light quarks in a bound state, paving the way to Heavy Quark Effective Theory [21] and its symmetry properties. On the other hand, if one aims at studying the hard production mechanism, Eq. 2.13 implies the possibility of computing the open-b cross section, which is free of collinear and infrared singularities order by order in perturbation theory (as opposed to, say, open-u cross section, whose final-state collinear singularities are cancelled only upon convolution with a non-perturbative fragmentation function). The b quark is also the heaviest quark which hadronizes before decaying, allowing us to test many of the ideas of the factorization theorems in a relatively clean environment. A priori, they

are therefore excellent probes of the underlying hard dynamics, whether that involves standard QCD processes or various kinds of new physics. They can also be identified in the data by techniques such as secondary vertices, prompt leptons or kinematical constraints.

2.2.1 Perturbative aspects

In order to understand the character of the perturbative process that occurred, it is often necessary to know not only that a c/b quark was produced, but also its original energy and direction of motion. The assumption is then often made that the observed charm/bottom hadron accurately reflects the original quark. For instance, the quark momentum distribution may be scaled down by a convolution with the Peterson fragmentation function [22], while the direction is assumed unchanged. In other cases, like for the study of CP violation in the B^0-$\overline{B}^0$ system, the produced hadrons are at the focus of attention, and a simple ansatz is that the composition of B hadrons is independent of the production environment and symmetric between particles and antiparticles.

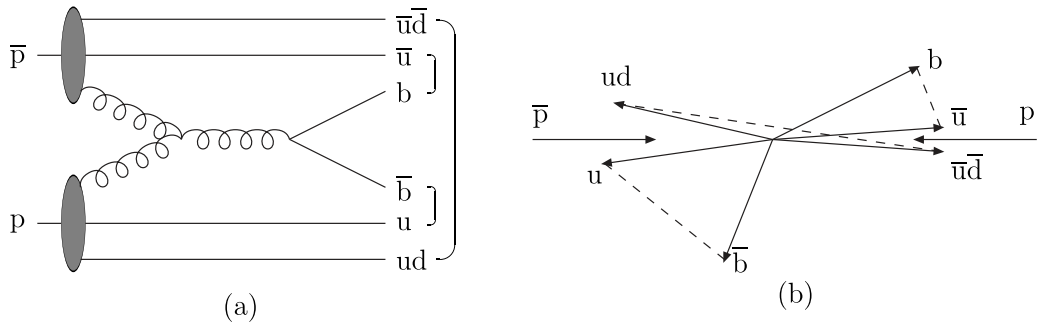

Figure 2.3: Example of a $p\overline{p}$ collision. (a) Graph of the process, with brackets denoting the final colour singlet subsystems. (b) Corresponding momentum space picture, with dashed lines denoting the colour strings.

The collision of two hadrons (Fig. 2.3) can be described as a sequence of distinct steps. A distinction between perturbative and nonperturbative parts of the calculation can be made. The *QCD factorization theorem* [23] allows the separation of short distance effects, which can be calculated perturbatively, and long distance effects which need to be modelled in other ways. At the center of the collision is the hard scattering of partons from the incoming hadrons. The partons are treated as unbound particles, and the process can be calculated at a fixed order in perturbation theory. The structure of the incoming hadrons is described by parton distribution functions (PDFs). The parton distribution

$f_i^A(x_i, \mu_F^2)$ gives the probability to find a parton i with a fraction x_i of the beam energy in beam particle A. The primary partons may undergo initial state radiation or splitting, and from this initial state shower two partons (each connected to one of the incoming hadrons) are selected to participate in the hard scattered interaction. In the case of QCD, the remnants of the incoming hadrons are not completely disconnected from the rest of the event. The cross section for the production of a b quark pairs from the the collision of two protons can be written from the factorization theorem as a convolution of the proton parton distribution functions with the $b\bar{b}$ cross section [24],

$$\sigma_{b\bar{b}} = \sum_{i,f} \int dx_i dx_j f_i^A(x_i, \mu_F^2) f_j^B(x_j, \mu_F^2) \hat{\sigma}_{ij}^{b\bar{b}}(p_i, p_j, \mu_F^2, \mu_R^2) \ , \tag{2.14}$$

and can be readily extended to other types of colliding particles. Here $\hat{\sigma}_{ij}^{b\bar{b}}$ is the short-distance cross section, the only pieces in Eq. 2.14 that can be computed in perturbation theory, μ_R^2 and μ_F^2 are the renormalization and factorization scales and $f_i^A(x_i, \mu_F^2)$ and $f_j^B(x_j, \mu_F^2)$ are the parton distribution functions.

The LO term (of $\mathcal{O}(\alpha_s^2)$) is trivial to obtain. The NLO one (of $\mathcal{O}(\alpha_s^3)$) was the result of landmark calculations [25]. Not surprisingly, the NNLO term is still not available; this may be worrisome, since at the NLO the scale dependence is still pretty large.

Several LO and NLO heavy quark production mechanisms in hadron-hadron collisions can be considered. Relevant LO and NLO Feynman diagrams are shown in Fig. 2.4. They can be categorised into three classes: flavour creation, flavour excitation and gluon splitting. The existence of the gluon was determined by identifying these NLO events. The three classes are characterized as follows:

1. in the LO description, the Q and $\bar{Q}$ have to emerge back-to-back in azimuth in order to conserve momentum, while the parton shower allows a net recoil to be taken by one or several further partons.

2. Flavour excitation is when a heavy flavour from the parton distribution of one beam particle is put on mass shell by scattering against a parton of the other beam, *i.e.* $Qq \to Qq$ or $Qg \to Qg$. When the Q is not a valence flavour, it must come from a branching $g \to Q\bar{Q}$ of the parton-distribution evolution.

3. Gluon splitting is when a $g \to Q\bar{Q}$ branching occurs in the initial- or final-state shower and no heavy flavours enter the hard scattering.

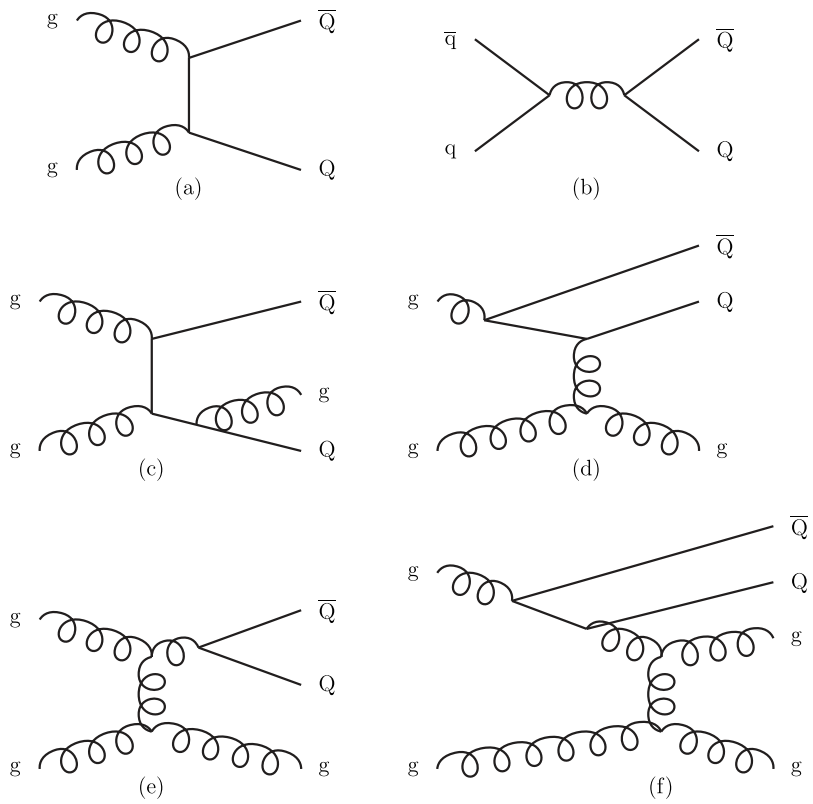

Figure 2.4: Examples of heavy-flavour production diagrams. (a,b) LO flavour creation. (c) Pair creation (with gluon emission). (d) Flavour excitation. (e) Gluon splitting. (f) Events classified as gluon splitting but of flavour-excitation character.

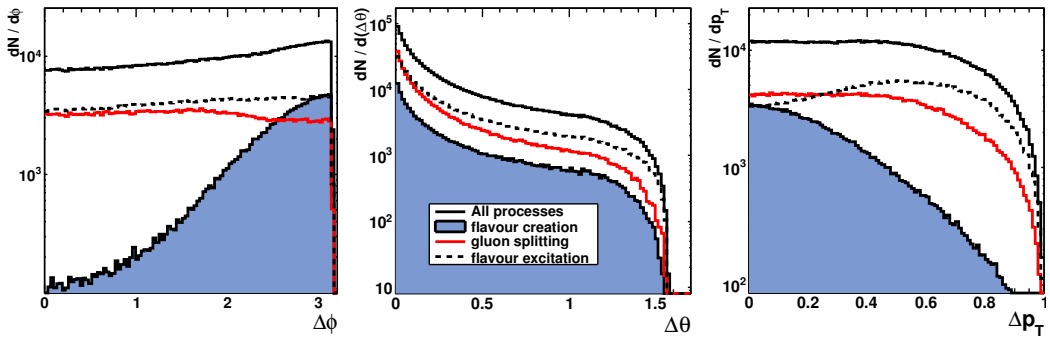

Figure 2.5: Correlated variables between b quark pairs produced from proton collisions: $\Delta\phi$, $\Delta\theta$ and $|A|$ respectively. Event generator is PYTHIA 6.4 [26]

Although events from the various categories cannot be fully separated, there are three primary correlated variables, shown in Fig. 2.5 that can be measured and used to determine the type of production mechanism. The first one is the opening angle $\Delta\phi$ between the quarks in the transverse plane, or plane perpendicular to the proton beam line. The second is the opening angle $\Delta\theta$ with respect to the beam line between the quarks. The third is the normalized difference in momentum in the transverse plane $|A| = \frac{|p_{\mathrm{T}_1} - p_{\mathrm{T}_2}|}{p_{\mathrm{T}_1} + p_{\mathrm{T}_2}}$. The dependence on the cross section on these correlated variables is calculated perturbatively by MC simulations.

In the case of flavour creation the two quarks are highly correlated. They are produced back-to-back, that is the angle between them is 180 ° in the centre of mass frame, they have roughly the same transverse momentum. In the gluon splitting the b quarks are close to one another in angular space and the momentum difference is spread out. In flavour excitation there is no real correlation in angular separation, but there is a large asymmetry in the momentum correlation. This large asymmetry is due to only one of the b quarks being produced directly from the hard scattering. The other quark is radiated before the hard-scattering occurs and has a very small momentum.

At LHC energies, the NLO order processes will make up 90% of b production. Current MC generators do not use the full NLO calculations, instead they simulate NLO by showering. The hard scattering and the b production are treated separately.

2.2.2 Non-perturbative aspects

Although theoretically well defined, the open-b cross section is not physically observable. In order to compare theoretical predictions with data, two things can be done: *a*) hadron-level experimental data are deconvoluted, and presented in terms of parton-level "measurements" that can be directly compared with open-b results. These deconvolutions are typically performed by means of parton shower Monte Carlos by the experimental collaborations. *b*) The open-b cross section is convoluted with a non-perturbative fragmentation function $D^{b\to H^b}$. For the single-inclusive p_{T} spectrum, one writes

$$\frac{\mathrm{d}\sigma H^b}{\mathrm{d}p_{\mathrm{T}}} = \int \frac{\mathrm{d}z}{z} D^{b\to H^b}(z,\epsilon)\frac{\mathrm{d}\hat{\sigma}}{\mathrm{d}\hat{p}_{\mathrm{T}}}, \qquad p_{\mathrm{T}} = z\hat{p}_{\mathrm{T}}\ . \tag{2.15}$$

$D^{b\to H^b}$ describes how a b quark transforms ("fragments") into a B hadron; it is not computable in perturbation theory but, being universal in the same

sense as PDFs, can be fitted to data in a given type of collision (usually e^+e^-) and used elsewhere. Common wisdom is that neither strategy *a*) nor *b*) have been particularly successful, since Tevatron data (and, to some extent, SpS ones) have been shown to be systematically larger than NLO QCD predictions [27], regardless of whether they were presented in terms of b quarks or of B mesons.

In order to study and understand the sizeable deviations from the simple picture, it is necessary to have a realistic framework for nonperturbative effects. The Lund String Model [20] is based on confinement and is best explained using $q\overline{q}$ production. As the q and $\overline{q}$ move apart from each other, a colour string connecting the two is stretched causing its potential energy to rise. These strings correspond to a Lorentz-invariant description of a linear confinement potential, with string tension $\kappa \approx 1\,\mathrm{GeV/fm}$. The total energy stored in the string increases with the distance of the two quarks q and $\overline{q}$, this energy will be eventually enough to produce a second pair $q'\overline{q}'$, breaking the primary string.

Each string piece has a colour charge at one end and its anticolour at the other. The double colour charge of the gluon corresponds to it being attached to two string pieces, while a quark is only attached to one. A diquark is considered as being in a colour antitriplet representation, and thus behaves (in this respect) like an antiquark. Then each string contains a colour triplet endpoint, a number (possibly zero) of intermediate gluons and a colour antitriplet end. An event will normally contain several separate strings (in the example of Fig. 2.3 three strings are produced).

The generation of quark pairs from string breaking is described in the Lund model as a quantum-mechanical tunnelling process in a linear potential. Simple calculations show that the tunnelling probability is inversely proportional to the quark constituent masses:

$$|\mathcal{M}|^2 = \propto e^{-(\pi m^2/\kappa)} \tag{2.16}$$

where m is the mass of the quark, leading to the suppression of heavy quarks production; in particular the proportion between different quark flavours is

$$u : d : s : c \approx 1 : 1 : 0.3 : 10^{-11}\ . \tag{2.17}$$

Charm and heavier quarks are therefore not expected to be produced in hadronization, even if they can take part in this process as the first quark pair, produced in the hard scattering.

The production of baryons within this model is simply explained by re-

placing the production of a quark pair by the production of a di-quark pair in a colour triplet state. The production of baryons is then suppressed with respect to mesons simply by the larger mass of the di-quark pair compared to the quark pair.

The string topology can be derived from the colour flow of the hard process. For instance, consider the LO process $u\overline{u} \to b\overline{b}$ in a $p\overline{p}$ collision. The colour of the incoming u is inherited by the outgoing b, so the b will form a colour-singlet together with the proton remnant, here represented by a colour antitriplet ud diquark. In total, the event will thus contain two strings, one b-ud and one $\overline{b}$-$\overline{u}\overline{d}$.

Once the string topology has been determined, the Lund string fragmentation model can be applied to describe the nonperturbative hadronization. To first approximation, one can assume that the hadronization of each colour singlet subsystem, *i.e.* the string, can be considered separately from that of all the other subsystems and that the fragmentation mechanism is universal, *i.e.* process-independent.

Depending on the invariant mass of a string, practical considerations lead to the need to distinguish three hadronization prescriptions:

1. *Normal string fragmentation.* In the ideal situation, each string has a large invariant mass. Then the standard iterative fragmentation scheme, for which the assumption of a continuum of phase-space states is essential, works well. The average multiplicity increases linearly with the string length, which means logarithmically with the string mass. In practice, this approach can be used for all strings above some cut-off mass of a few GeV.

2. *Cluster decay.* If a string is produced with a small invariant mass, maybe only two-body final states are kinematically accessible. Such a low-mass string is called cluster, and it is considered separately from above. When kinematically possible, a Q-$\bar{q}$ cluster will decay into one heavy and one light hadron by the production of a light quark–antiquark pair in the colour force field between the two cluster endpoints.

3. *Cluster collapse.* This is the extreme case of the above situation, where the string mass is so small that the cluster cannot decay into two hadrons. It is then assumed to collapse directly into a single hadron, which inherits the flavour content of the string endpoints. This mechanism plays a special role, in that it allows large flavour asymmetries in favour of hadron species that can inherit some of the beam-remnant flavour content.

Pythia MC generator [26], used for LHCb simulations, implements the Lund string fragmentation model. The other most used fenomenological approach is the Cluster fragmentation model [28] and it is the one implemented in the Herwig MC generator [29].

2.3 Experimental QCD

Since we are not able to directly measure partons (quarks or gluons), but only hadrons and their decay products, a central issue for every experimental test of QCD is establishing a correspondence between observables obtained at the partonic and the hadronic level. This correspondence is achieved by means of infrared and collinear safe quantities, which allow one to obtain finite predictions at any order of perturbative QCD; the simplest case of such observables is the total cross section. More generally, when measuring inclusive observables, the final state is not analyzed at all regarding its (topological, kinematical) structure or its composition. Basically the relevant information consists in the rate of a process ending up in a partonic or hadronic final state.

As soon as parts of the structure or composition of the final state are analyzed and cross section differential in one or more variables characterizing this structure are of interest, we talk about exclusive observables, such as jet rates, jet substructure and event-shape distributions. Furthermore, any cross section differential in some characteristic kinematic quantity of the final state falls into this category, such as transverse momentum distributions of jets or vector bosons in hadron collisions.

It is worth mentioning that, besides the correspondence between the parton and hadron level, also a correspondence between the hadron level and the actually measured quantities in the detector has to be established. The simplest examples are corrections for finite experimental acceptance and efficiencies.

2.3.1 Hadronic jets

In hard interactions, final-state partons and hadrons appear predominantly in collimated bunches. These bunches are generically called jets. To a first approximation, a jet can be thought of as a hard parton that has undergone soft and collinear showering and then hadronization. Jets are used both for testing our understanding and predictions of high-energy QCD processes, and also for identifying the hard partonic structure of decays of massive particles like top quarks.

Jets need to be defined: this is generally done through a jet definition, a set of rules for how to group particles into jets and how to assign a momentum to the resulting jet. A good jet definition can be applied to experimental measurements, to the output of parton-showering Monte Carlos and to partonic calculations, and the resulting jets provide a common representation of all these different kinds of events.

Jets are used for a wide range of physics analyses. One way of classifying their uses is according to the different possible origins for the partons that give rise to the jets. At hadron colliders, one of the best studied jet observables is the inclusive jet spectrum, related to the high-momentum-transfer $2 \to 2$ scattering of partons inside the colliding (anti)protons. In this kind of process the energy of the jet (in the partonic centre-of-mass frame) is closely related to that of the parton in the proton that underwent a hard scattering and the inclusive jet spectrum therefore contains information on the distributions of partons inside the proton (e.g. [30]), and also on the strength of their interaction. Another origin for the partons that lead to jets is that they come from the hadronic decay of a heavy particle, for example a top quark, a Higgs boson, or some other yet-to-be discovered resonance. Jets may also originate radiatively, for example from the emission of a gluon off some other parton in the event. The rate of production of such jets provides information on the value of strong coupling (*e.g.* [31]) and is related also to the colour structure of events.

Given the variety of these and other related possible uses of jets, it should not be surprising that there is no single optimal way of defining jets and, over the 30 years that have passed since the first detailed proposal for measuring jets, many jet definitions have been developed and used.

Two main classes of jet algorithm can be identified: cone algorithms, extensively used at hadron colliders, and sequential recombination algorithms, more widespread in e^+e^- and ep colliders.

Very generically, most (iterative) cone algorithms start with some seed particle i, sum the momenta of all particles j within a cone of opening-angle R, typically defined in terms of (pseudo-)rapidity and azimuthal angle. They then take the direction of this sum as a new seed and repeat until the cone is stable, and call the contents of the resulting stable cone a jet if its transverse momentum is above some threshold $p_{\mathrm{T}min}$. The parameters R and $p_{\mathrm{T}min}$ should be chosen according to the needs of a given analysis.

Sequential recombination algorithms at hadron colliders are characterized by a distance $d_{ij} = \min(k_{t,i}k_{t,j})\Delta_{ij}^2/R^2$ between all pairs of particles i, j, where Δ_{ij} is their distance in the rapidity-azimuthal plane, $k_{t,i}$ is the transverse

momentum with respect to the incoming beams, and R is a free parameter. They also involve a "beam" distance d_{iB}. One identifies the smallest of all the d_{ij} and d_{iB} and if it is a d_{ij}, then i and j are merged into a new pseudo-particle, if the smallest distance is d_{iB} then i is removed from the list of particles. As with cone algorithms, one usually considers only jets above some transverse-momentum threshold $p_{\mathrm{T}min}$.

3 The LHCb Experiment

3.1 CERN and The Large Hadron Collider

The European Organization for Nuclear Research (CERN), is the world's largest particle physics laboratory, situated on the Franco-Swiss frontier, near Geneva. Established in 1954, when 11 European states agreed to set up a centre for fundamental research to investigate the nature of the universe at the very small scale, CERN has been the site of key discoveries such as the neutral currents predicted by electroweak unification first seen by the Gargamelle experiment in 1973 [32]. The $W^{\pm}$ and Z^0 bosons were discovered by the UA1 experiment at the Super Proton Synchrotron (SPS) $p\overline{p}$ collider in 1983 [33]. The 27 km circumference Large Electron-Positron (LEP) collider was in operation from 1989 to 2000 and was used to prove the existence of three, and only three, generations of light neutrinos that couple to the Z^0 boson: the best indication that the three generation picture for matter particles in the Standard Model is correct.

Now in 2012, CERN is supported by 20 European member states and, with participation from more than 80 countries, has become the world's focus for research in fundamental physics. A total of 10000 visiting scientists from 608 institutes and universities from 113 countries around the world use CERN's facilities, amounting to half of the world's particle physicists. Moreover, CERN employs around 2400 people between scientific and technical staff. It currently hosts the largest particle accelerator in the world, the Large Hadron Collider (LHC), and its six experiments: ALICE, ATLAS, CMS, LHCb, LHCf and TOTEM. A diagram of the LHC ring including the positions of the detectors is shown in Fig. 3.1.

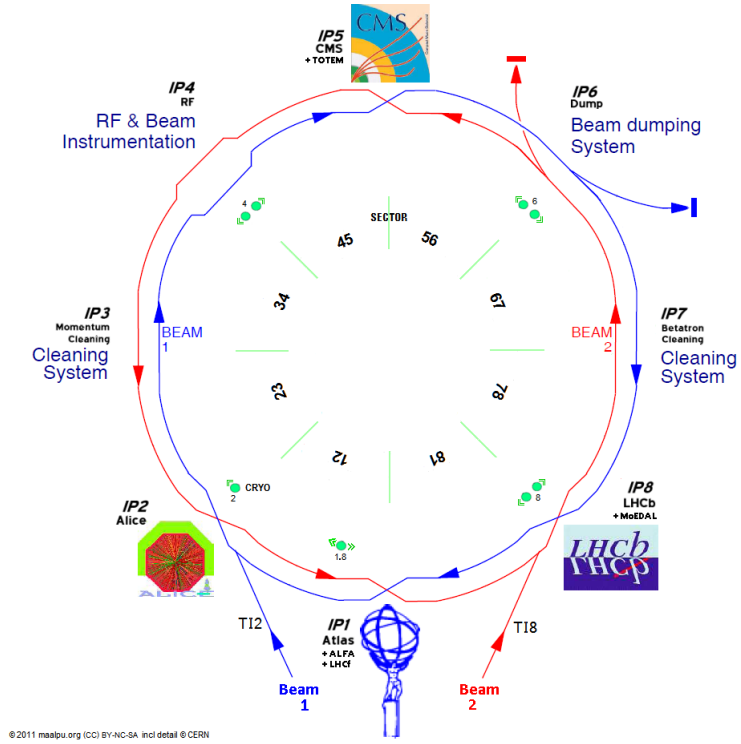

Figure 3.1: A schematic of the LHC and the positions of the four main detectors.

3.2 The Large Hadron Collider

The superconducting hadron collider LHC is the highest energy particle accelerator in the world, currently producing proton-proton collisions at a centre of mass energy $\sqrt{s} = 8\,\text{TeV}$ [34]. Built in the old LEP ring tunnel between 45 m and 170 m below ground level on a plane inclined 1.4° towards the Léman lake, the LHC has the potential to create new high-mass particles that could never have been produced in previous facilities.

The LHC is designed to reach a target collision energy of 14 TeV with a luminosity, $\mathcal{L}$, of $10^{34}\,\text{cm}^{-2}\,\text{s}^{-1}$. This enormous particle intensity is required to search for undiscovered rare phenomena and for new particles, such as the Higgs boson. Given $N = \mathcal{L}\sigma\mathcal{B}$ the number of observable events per second, where σ is the production cross section and $\mathcal{B}$ the branching fraction for a given decay, the designed LHC could therefore produce the Standard Model $115\,\text{GeV}/c^2$ Higgs at a rate of about 25 per minute in the dominant mode, with $\sigma(gg \to H^0X) = 58 \times 10^{-36}\,\text{cm}^2$ and $\mathcal{B}(H^0 \to b\bar{b}) = 71\%$ [35].

The predicted $b\bar{b}$ production cross-section at 14 TeV is 500 μb and so the

expected rate of $b\bar{b}$ pair production at LHCb, which is designed to run at $\mathcal{L} = 2 \times 10^{32}\,\mathrm{cm}^{-2}\,\mathrm{s}^{-1}$, is 50000 per second when the LHC is running under design conditions.

Charged particles must be accelerated to ultra-relativistic speeds, where energy loss from synchrotron radiation becomes an issue. This loss is relatively less important for more massive particles. On top of that, antiparticles are expensive to produce and store. These two main reasons led CERN to move from LEP e^-e^+ collisions to LHC pp collisions. Whereas LEP accelerated oppositely-charged leptons within a single ring, the LHC collides hadrons with like-charges and therefore requires two separate rings with counter-rotating beams.

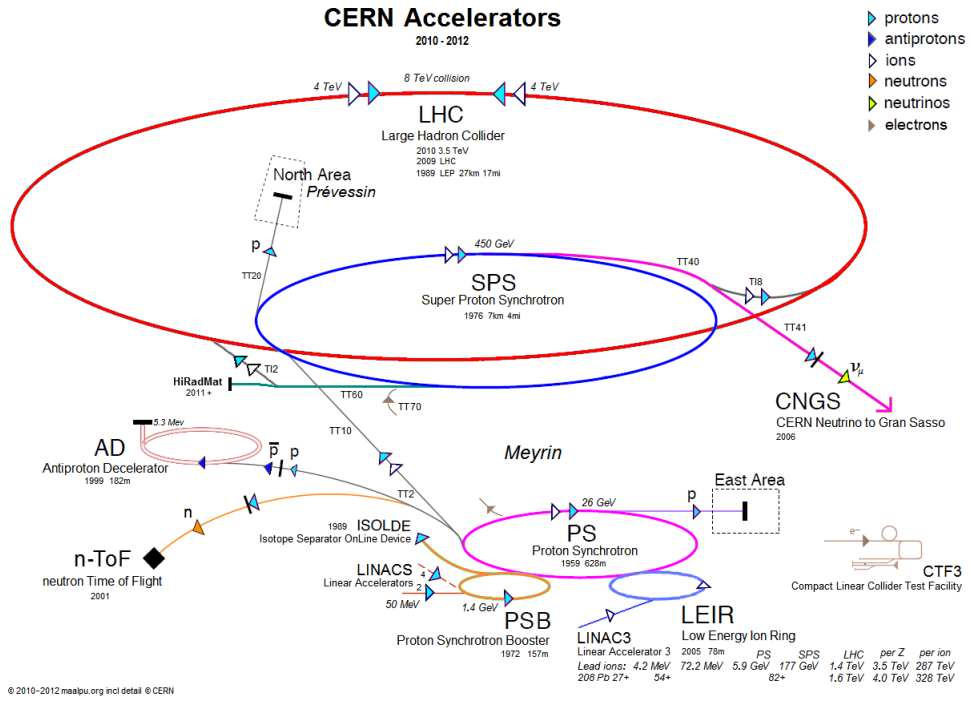

Figure 3.2: The accelerator complex at CERN used to feed protons from ionized hydrogen into the LHC at 450 GeV.

As with the re-use of LEP's tunnel, CERN has upgraded a number of past accelerators to provide the feed chain for the LHC (Fig. 3.2). Protons are incrementally accelerated through the CERN accelerator complex before injection into the LHC. They flow through a chain of accelerators: Linac2 (50 MeV) - Proton Synchrotron Booster (1.4 GeV) - Proton Synchrotron (25 GeV) - Super Proton Synchrotron (450 GeV). Each proton beam consists of a series of

"bunches" containing up to 1.15×10^{11} protons with a maximum of 2808 bunches per beam. The bunches are separated by 25 ns giving a maximum collision rate of 40 MHz. At the maximum energy per beam of 7 TeV each proton is travelling at $0.999999991\,c$.

Proton beams are brought into collision simultaneously at four points around the ring. Each collision point is located within a subterranean cavern housing one of the four main purpose-built particle detector.

ATLAS [36] and CMS [37] are general purpose detectors with the objective to test the Standard Model at the TeV scale, and to search for the Higgs boson and physics beyond the Standard Model. They are barrel shaped machines that cover the full 4π steradians angular acceptance with the exception of a narrow region around the beam pipe. They are optimized to trigger on events with high transverse momentum objects at large angles to the beamline. ATLAS is the biggest detector built on the LHC, with a diameter of 22 m and a length of 40 m. CMS is equipped with a 4 T superconducting solenoid, chosen to provide the large bending power needed. ALICE [38] is dedicated to the study of the physics of strongly interacting matter and the quark-gluon plasma (QGP) at extreme values of energy density and temperature in heavy nuclei (Pb-Pb) collisions.

These three main detectors are depicted in Figs. 3.3-3.4-3.5 The LHCb experiment is the focus of Sec. 3.3.

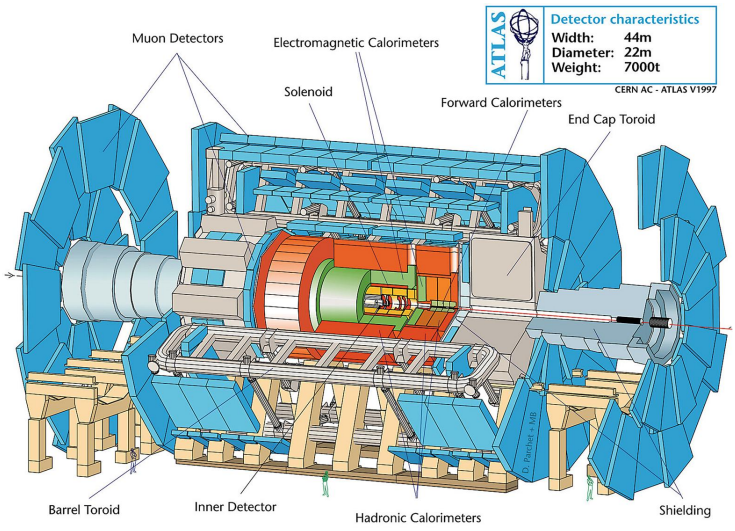

Figure 3.3: The ATLAS detector [36].

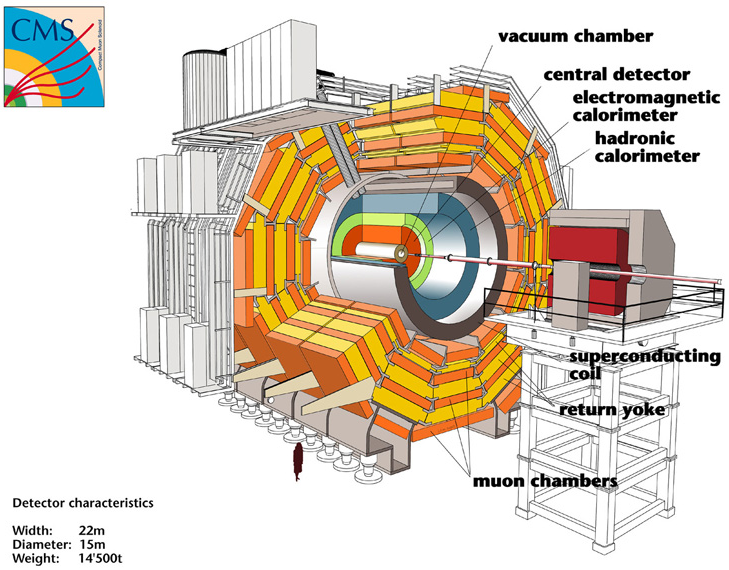

Figure 3.4: The CMS detector [37].

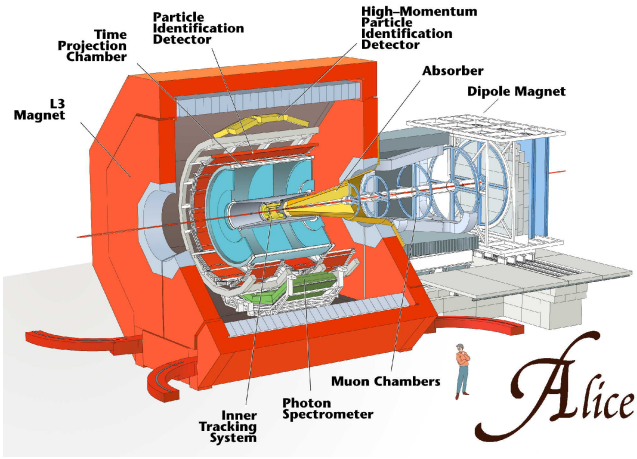

Figure 3.5: The ALICE detector [38].

3.3 The LHCb detector

The Large Hadron Collider Beauty (LHCb) detector [39] is hosted at Interaction Point 8 of the LHC accelarator, in the cavern formerly occupied by the DELPHI [40] experiment. It is dedicated to the study of heavy flavor physics at the LHC. Its main aim is to search for indirect evidence of new physics in *CP* violation and in the rare decays of hadrons containing b (and c) quarks.

LHCb was designed to be operated at a modest luminosity, $\mathcal{L} = 2 \times$

$10^{32}\,\mathrm{cm}^{-2}\,\mathrm{s}^{-1}$, compared to the LHC's maximum $10^{34}\,\mathrm{cm}^{-2}\,\mathrm{s}^{-1}$. This luminosity was achieved in May 2011, making LHCb the first LHC experiment to reach design operating conditions. This luminosity was chosen to maximize the probability of single parton interactions per bunch crossing (Fig. 3.6) in order to simplify B decay identification. This interaction probability results

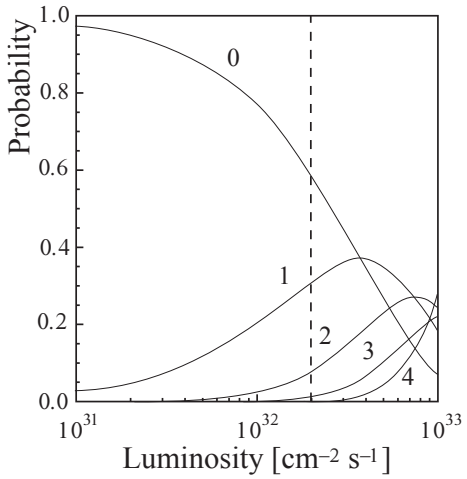

Figure 3.6: The probability of parton interactions as a function of luminosity. Events with a single interaction dominate at LHCb with $\mathcal{L} = 2 \times 10^{32}\,\mathrm{cm}^{-2}\,\mathrm{s}^{-1}$ [41].

in an average number of visible pp collisions in LHCb, μ, of about 0.4. With experience of actual running conditions and improvements in background rejection, this interaction rate has been increased to an average μ of about 1.0 to 2.5.

The number of produced $b\bar{b}$ pairs in a nominal year is expected to be $\sim 10^{12}$. Figure Fig. 3.7 shows the polar angle correlation between the b and the $\bar{b}$ of a $b\bar{b}$ pair produced at LHCb as predicted by LO Pythia generator [26]: they are produced predominantly in the forward and backward directions where the angles of flight of the two quarks are positively correlated. Thus, if one quark from the $b\bar{b}$ pair flies within the LHCb geometrical acceptance then the other is also likely to do so. Despite covering only around 4% of the total solid angle, the LHCb experiment accepts around 40% of all heavy-quarks (c, b, t) produced in the LHC collisions and so the single-arm design achieves both economy and good physics coverage.

The LHCb detector must be able to exploit this large number of B hadrons. This requires an efficient, robust and flexible trigger in order to cope with the complex hadronic environment. The trigger must be sensitive to many differ-

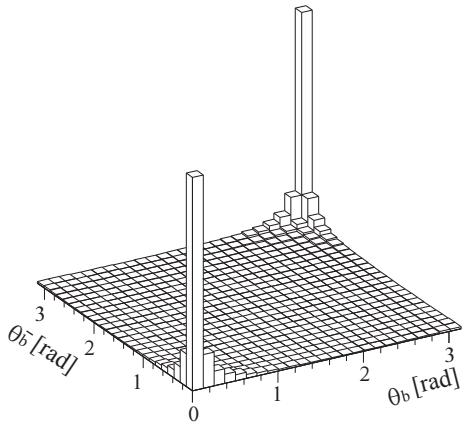

Figure 3.7: The polar angles of b versus $\bar{b}$ quarks produced at the LHC as predicted by PYTHIA.

ent final states. Excellent vertex and momentum resolution are essential prerequisites for the good proper-time resolution necessary to study the rapidly oscillating $B_s^0 - \overline{B}_s^0$ meson system and also for the good invariant mass resolution, needed to reduce combinatorial background. In addition to electron, muon, photon, π^0 and η detection, identification of protons, kaons and pions is crucial in order to cleanly reconstruct many hadronic B meson decay final states. Finally, a data acquisition system with high bandwidth and powerful online data processing capability is needed to optimize the data taking.

3.3.1 Performance during 2010

During 2010 the LHC ran with an energy per beam of 3.5 TeV and a centre of mass energy of 7 TeV. By the end of the run the peak luminosity at LHCb reached almost $2 \times 10^{32}\,\mathrm{cm}^{-2}\,\mathrm{s}^{-1}$ with only 344 colliding bunches, a factor of eight fewer than the designed maximum. As a result the average number of proton-proton interactions per bunch crossing μ exceeded 2.5, presenting a serious challenge for the LHCb experiment which was designed to run with $\mu = 0.4$. Nonetheless LHCb achieved a data taking efficiency of 89%, recording $37.66\,\mathrm{pb}^{-1}$ of a total delivered luminosity of $42.15\,\mathrm{pb}^{-1}$. The integrated luminosity over the year 2010 is shown in Fig. 3.8.

The $b\bar{b}$ production cross-section at a centre-of-mass energy of 7 TeV was measured by LHCb as $\sigma(pp \to b\bar{b}X) = 284 \pm 20(\mathrm{stat}) \pm 49(\mathrm{syst})\,\mu\mathrm{b}$ [42]. Thus, an estimated 10 billion $b\bar{b}$ pairs were produced at the LHCb experiment during 2010.

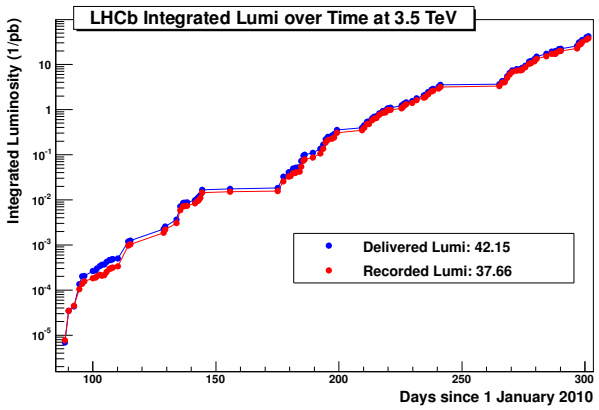

Figure 3.8: The integrated luminosity delivered to and recorded by the LHCb experiment throughout 2010.

3.4 Detector layout

LHCb is a single-arm spectrometer with a forward angular coverage from approximately 10 mrad to 300 (250) mrad in the bending (non-bending) plane. In terms of *pseudorapidity*,

$$\eta = -\ln\tan(\frac{\theta}{2}) \ , \tag{3.1}$$

where θ is the polar angle with respect to the z axis (see Fig. 3.9), the acceptance of LHCb is $1.9 < \eta < 4.9$.

The layout of the LHCb spectrometer is shown in Fig. 3.9. The right-handed coordinate system adopted has the z axis along the beam, and the y axis along the vertical.

LHCb capability to identify characteristic displaced vertices from boosted B hadron decays relies on a silicon vertexing tracker (VELO) around the interaction point [43]. The B decay products are detected by tracking and calorimetry systems and specific decay processes are distinguished by identification (PID) of charged particle species with the Ring Imaging Cherenkov (RICH) and muon detectors [44]. The calorimeters provide PID for photons, electrons and hadrons [45].

The LHCb detector consists of six subdetectors, which are grouped in three interdependent systems:

- the Tracking System, made of:

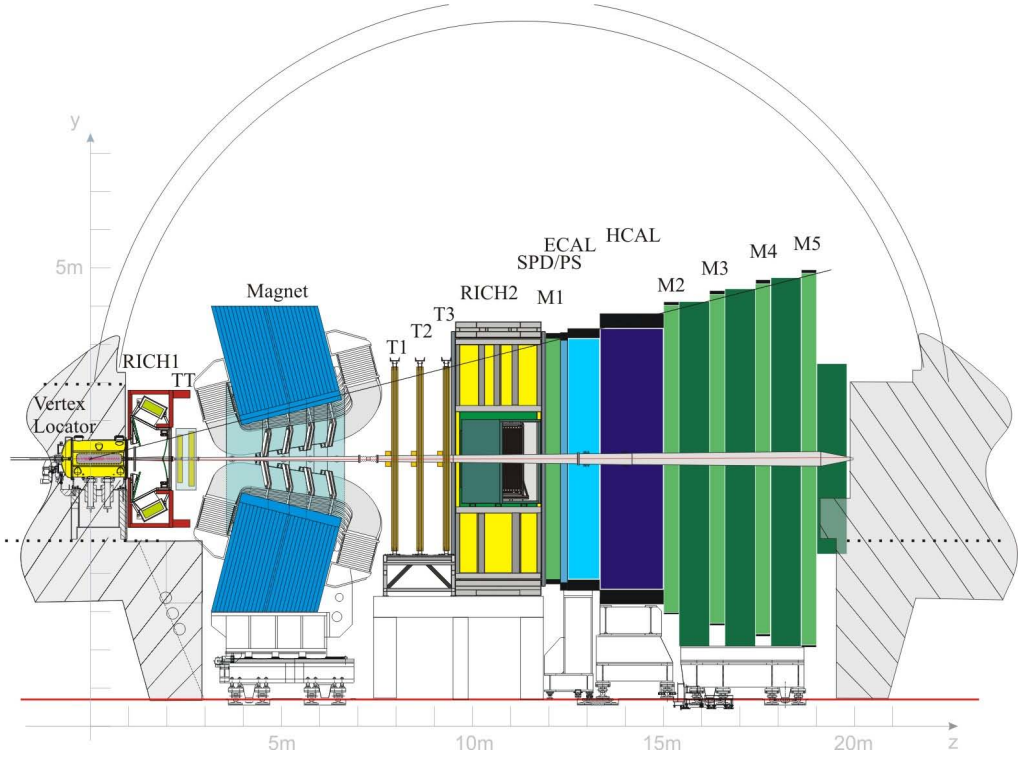

Figure 3.9: View of the LHCb detector.

  - the VErtex LOcator (VELO), which provides the capability to identify characteristic displaced vertices from boosted B hadron decays [43];
  - the Tracker Turicensis (TT), a silicon microstrip detector in front of the spectrometer magnet [46];
  - three tracking stations – T1, T2, and T3 – each composed of a central Inner Tracker station (IT) surrounded by an Outer Tracker station (OT) [47, 48];
  - the LHCb Magnet to bend charged particles in the x-z plane for momentum measurements [49];

- the Particle Identification System:

  - two Ring and Imaging Cherenkov detectors (RICH1 and RICH2) for particle identification (PID) of charged particle species [44];
  - the Calorimeters, providing PID for photons, electrons and hadrons and composed by the Scintillating Pad Detector (SPD), the Pre-

Shower detector (PS), the Electromagnetic CALorimeter (ECAL) and the Hadronic CALorimeter (HCAL) [45];

– five muon stations – M1, M2, M3, M4, and M5 – which compose the Muon Detector [50];

- The Trigger System, composed by some of the already mentioned sub-detectors plus the pile-up detector, dedicated exclusively to triggering [51].

The beampipe

The beampipe is designed to minimize its contribution to the material budget in the detector acceptance. This is especially important in the high-rapidity region (see Fig. 3.10 for a summary of the material budget before the calorimeters), where the particle density is higher. Beryllium was chosen as the material for 12 m out of the 19 m long beampipe, for its high transparency to the particles resulting from the collisions. It is the best available material for this application given its high radiation length combined with a modulus of elasticity higher than that of stainless steel.

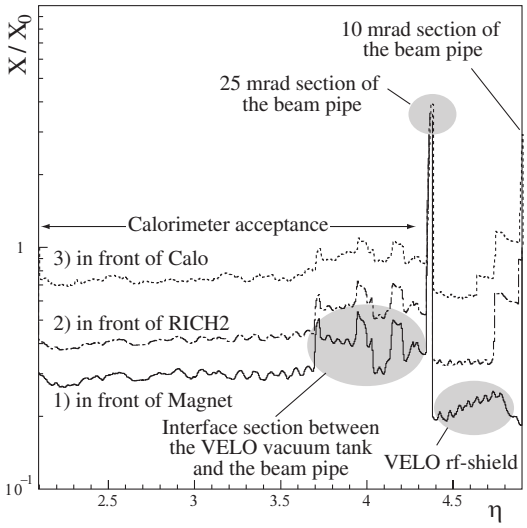

Figure 3.10: Material seen by a neutral particle from the nominal position of the interaction point as a function of the pseudorapidity at three different z positions before the calorimeter (1–3), averaged over the azimuthal angle.

3.4.1 The Tracking system

An accurate measurement of the trajectories of particles produced in collisions is mandatory for all physics analyses at LHCb. To achieve several of the key measurements of the LHCb physics program [52] it is important that the detector provides an excellent momentum resolution. The combination of the path of a particle with knowledge of the LHCb magnetic field allows the particle's momentum to be measured.

The Tracking system consists of the VELO, the Magnet, and four planar tracking stations: TT, upstream of the dipole magnet, and T1–T3, downstream of the magnet. The VELO and TT use silicon microstrip detectors. In T1–T3, silicon microstrips are used in the region close to the beampipe –the IT– and straw-tubes are used in the outer region of the stations, the OT. The TT and the IT were developed in a common project called the Silicon Trackers (ST).

For the purpose of this discussion it is helpful to define the *upstream* and *downstream* directions which point from the muon stations towards the VELO and vice versa.

3.4.1.1 The magnet

In common with almost all particle physics experiments, a dipole magnet (Fig. 3.11a) is used in the LHCb experiment to measure the momentum of charged particles. It is a warm magnet design with saddle-shaped coils in a window-frame yoke with sloping poles in order to match the required detector acceptance.

The design of the magnet with an integrated magnetic field of 4 Tm for tracks of 10 m length had to accommodate the contrasting needs for a field level inside the RICHs envelope less than 2 mT and a field as high as possible in the regions between the vertex locator, and the TT tracking station (see Fig. 3.11b). The conductor has a specific resistance of below 28 Ωm at 20°C and each coil weighs 27 tons. The polarity of the magnetic field may be swapped between "up" and "down" which is extremely useful in determining systematic effects due to charge asymmetries associated with the detector.

In order to achieve the required momentum resolution for charged particles, the magnetic field must be measured with a relative precision of a few times 10^{-4} and the position of the B-field peak with a precision of a few millimetres. A semi-automatic measuring device was constructed which allowed remotely controlled scanning along the longitudinal axis of the dipole by means of an array of Hall probes.

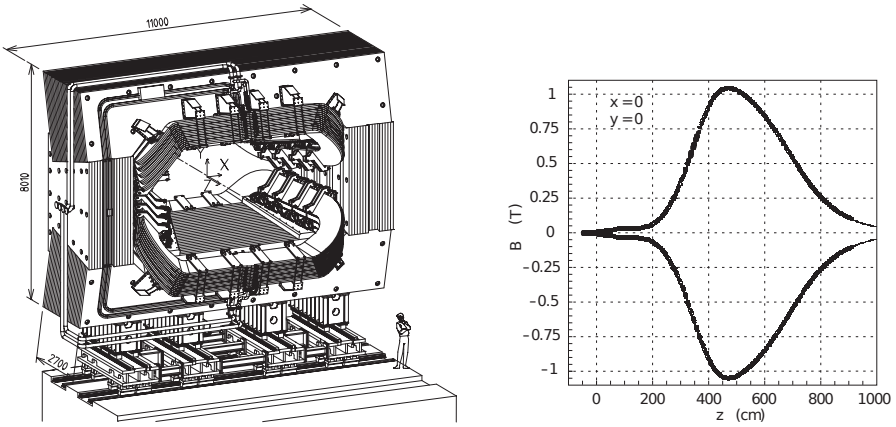

(a) (b)

Figure 3.11: (a) Perspective view of the LHCb dipole. The interaction point lies behind the magnet. (b) Magnetic field strength along the z axis for both up and down polarities.

3.4.1.2 Vertex locator

The VErtex LOcator (VELO) provides precise measurements of track coordinates close to the interaction region, which are used to identify the displaced secondary vertices which are a distinctive feature of b and c-hadron decays [43]. Most b-hadrons decay inside the VELO, in a so-called *secondary vertex* (SV). In a secondary vertex, the b-hadron daughter tracks converge to a point displaced from the interaction point or *primary vertex* (PV). Secondary vertices play a crucial role in the High Level Trigger (HLT) and are used to enrich the b-hadron content of selected data. Therefore, a precise track reconstruction in this region is needed in order to separate primary from secondary vertices. The VELO is able to detect particles with $1.6 < \eta < 4.9$ and emerging from interactions in the range $|z| < 10.6\,\text{cm}$.

The VELO consists of a series of silicon modules, each providing a measure of the r and ϕ coordinates, arranged along the beam direction (Fig. 3.12). Two planes perpendicular to the beam line and located upstream of the VELO sensors are called the *pile-up veto system*.

The VELO sensors are placed at a radial distance from the beam which is smaller than the aperture required by the LHC during injection and must therefore be retractable for safety reasons. The detectors are mounted in a vessel that maintains vacuum around the sensors and is separated from the machine vacuum by a thin walled corrugated aluminium sheet. This is done to minimize the material traversed by a charged particle before it crosses the

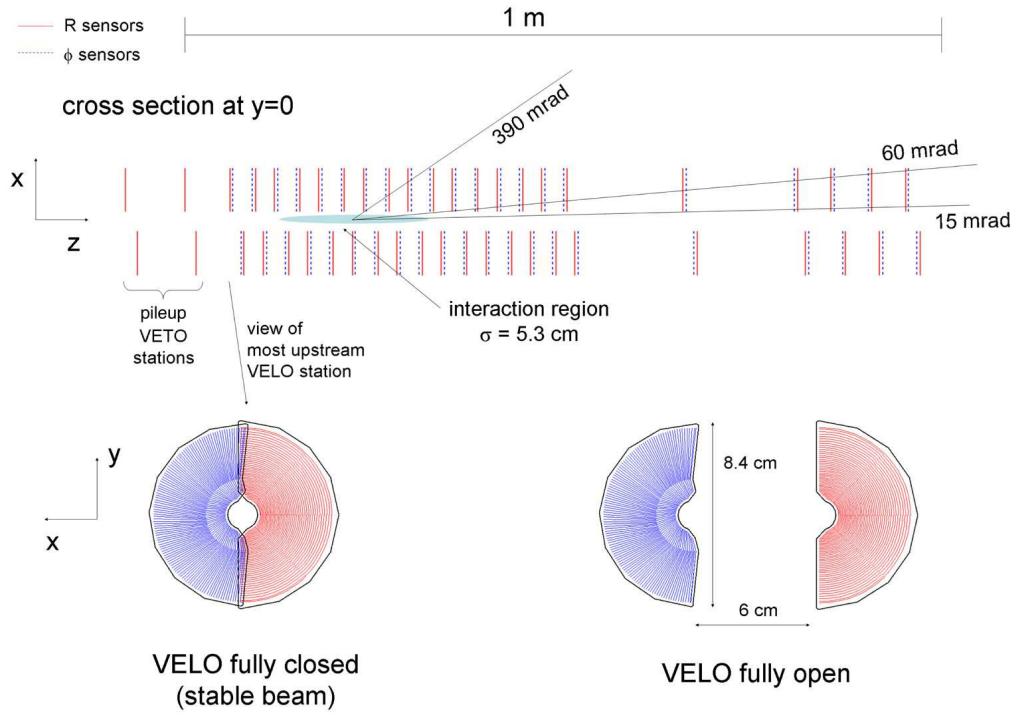

Figure 3.12: Cross section in the (x,z) plane of the VELO silicon sensors, at $y = 0$, with the detector in the fully closed position. The front face of the first modules is also illustrated in both the closed and open positions. The two pile-up veto stations are located upstream of the VELO sensors.

sensors and the geometry is such that it allows the two halves of the VELO to overlap when in the closed position.

Each of the 21 VELO stations is composed by one r-sensor and one ϕ-sensor. The r-sensors are made of concentric semicircular strips (4×512 strips) centered on the nominal LHC beam position. The ϕ-sensors are subdivided into two regions, inner and outer, with 683 and 1365 strips, respectively. This allows to avoid unacceptably high strip occupancies in the innermost edge and too large strip pitch at the outer edge of the sensor.

The track definition within the LHCb acceptance ($1.6 < \eta < 4.9$) requires hits in at least three modules and are reconstructed with the polar coordinates collected in these modules. From preliminary measurements, the primary interaction vertex resolution was determined to be $\sigma(x, y, z) = (16, 15, 90)\,\mu\text{m}$, with a cluster finding efficiency of 99.8%, and a best single hit precision of

4 µm at the optimal track angle [53].

3.4.1.3 Silicon Tracker

The term "Silicon Tracker" (ST) includes the Tracker Turicensis (TT) located upstream of the dipole magnet and the Inner Tracker (IT) [47] which is located downstream of the dipole magnet. Both the TT and IT detectors use microstrip sensors with a strip pitch of about 200 µm with active surface areas of 8.4 m^2 and 4.0 m^2 respectively. Each of the four ST stations has four detection layers in an (x-u-v-x) geometry, with vertical strips for the two x layers sandwiching layers with strips rotated by $+5°$ and $-5°$ about the z-axis for u and v respectively to enhance spatial resolution.

The design choices for the Silicon Tracker detectors were largely driven by the following considerations:

Spatial resolution. Simulation studies have demonstrated that a single-hit resolution of about 50 µm is adequate for both the TT and the IT. The momentum resolution of the spectrometer is then dominated by multiple scattering over almost the full range of particle momenta.

Hit occupancy. Charged particle densities of about 5×10^{-2} per cm^2 for minimum bias events are expected in the innermost regions of the TT. They fall off by two orders of magnitude to about 5×10^{-4} per cm^2 in the outermost regions of the detector. Different readout strip lengths were chosen for different regions of the detector to keep maximum strip occupancies at the level of a few percent while minimizing the number of readout channels.

3.4.1.4 Outer Tracker

The LHCb Outer Tracker (OT) is a drift-time detector [48] for the tracking of charged particles and the measurement of their momentum over a large acceptance area. A required mass resolution of 10 MeV/c^2 for the decay $B_s^0 \to D_s^- \pi^+$ translates into a required momentum resolution of $\delta p/p \approx 0.4\%$. The reconstruction of high multiplicity B decays demands a high tracking efficiency and at the same time a low fraction of wrongly reconstructed tracks: a track efficiency of 95% would result, for the decay $B_s^0 \to D_s^- \pi^+$, in an overall reconstruction efficiency of 80%.

Each OT module contains two staggered monolayers of drift-tubes with inner diameters of 4.9 mm. A mixture of Argon (70%) and CO_2 (30%) is

chosen as a counting gas in order to guarantee a drift time below 50 ns and a drift-coordinate resolution of 200 µm. Modules in the x-layers are oriented vertically, whereas those in the u and v layers are tilted by $\pm 5°$, respectively. The total active area of a station is $5971 \times 4850\,\mathrm{mm}^2$ covering all the LHCb acceptance not covered by the IT stations.

3.4.1.5 Track reconstruction

The LHCb track reconstruction consists in combining the hits in the VELO, the TT, the OT and the IT detectors to form particle trajectories from the interaction region to the calorimeters, regardless of their origin.

The magnetic field strength drops away from the centre of the magnet, out towards the VELO and T-stations, therefore momentum measurements are typically made by matching relatively straight upstream and downstream track segments to form *long* tracks, as illustrated in Fig. 3.13.

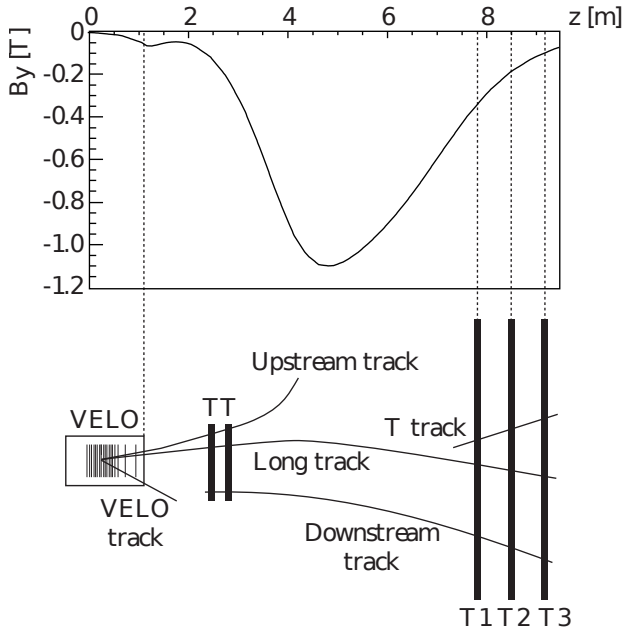

Figure 3.13: An illustration of the various track types: VELO, upstream, long, downstream and T-tracks. The evolution of the magnetic field strength, B_y , is given along the z-axis.

Long tracks cross the full tracking system from the VELO to the T stations. These have the most precise momentum determination and therefore are the most commonly used set of tracks for physics analyses.

The track reconstruction starts with a search for almost aligned track *seeds*, the initial track candidates, in the VELO and the T stations where the magnetic field is low. Trajectories are refitted with a Kalman filter in order to account for multiple scattering and correct for dE/dx energy loss. This algorithm then tries to associate hits in the other parts of the tracking system to form track candidates. The quality of the reconstructed tracks is monitored by the χ^2 of the fit and the pull distribution of the track parameters.

The track finding efficiency has been measured using $K^0 \to \pi^+\pi^-$ decays and is found to be greater than 95% for all tracks with a transverse momentum greater than 100 MeV/c. The tracking efficiency as a function of transverse momentum is show in Fig. 3.14.

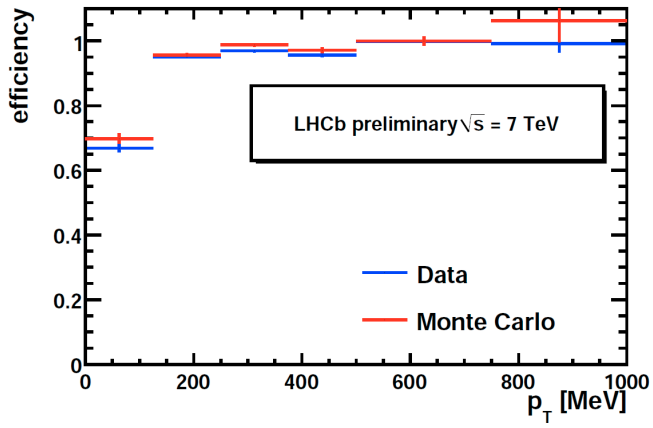

Figure 3.14: The tracking efficiency as a function of transverse momentum calculated from $K^0 \to \pi^+\pi^-$ from LHCb 2010 data compared with the performance predicted by MC simulations.

High momentum resolution at LHCb is essential for a number of reasons. Momentum criteria are used extensively in the trigger and selections to isolate events with physics interest. Momentum measurements are also used to reconstruct the masses of decaying particles, determine particle identity and reconstruct proper decay times. The nominal momentum resolution has been measured as $\delta p/p = (0.35 - 0.55)\%$ depending upon the momentum of the track.

The impact parameter (IP) of a track is defined as the distance of closest approach between the extrapolated particle track and the primary proton-proton collision vertex. High impact parameter resolution is important as the LHCb trigger imposes requirements on the impact parameter of tracks in order to locate displaced vertices from B and D meson decays. The impact

parameter resolution is found to be $\sigma_{IP} = (20 \pm 29/p_{\mathrm{T}})\,\mu\mathrm{m}$, where p_{T} is the transverse momentum of the track in GeV.

3.4.2 The Particle Identification System

Particle identification (PID) is a fundamental requirement for LHCb. It uses the combined outputs of the calorimeters, muon chambers and RICH detectors to assign a likelihood to be either a muon, electron, proton, pion or kaon to each track. The RICH detectors are especially important in separating pions from kaons. The LHCb Calorimeter is used for particle identification of electrons, photons and hadrons, as well as for their energy and position measurement. The muon system provides fast information for the high-p_{T} muon trigger at the earliest level (Level-0) and muon identification for the high-level trigger (HLT) and offline analysis.

3.4.2.1 Ring Imaging Cherenkov detectors

It is essential for the goals of the experiment to separate pions from kaons in selected B hadron decays, in order to separate similar decays such as $B^0_{(s)} \to \pi^+\pi^-$, $K^\pm\pi^\mp$, K^+K^-. The discovery of Cherenkov radiation led to the development of Ring Imaging Cherenkov (RICH) detectors for PID. An electrical insulator (or *radiator*) will produce light at a particular angle, θ_{C}, to the trajectory of a charged particle passing through it with superluminal velocity, $v > c/n$, where c is the speed of light in a vacuum and n is the refractive index of the radiator. Measurement of this angle allows calculation of the particle velocity, by

$$v = \frac{c}{n \cos\theta_{\mathrm{C}}} \ . \tag{3.2}$$

Combined with a momentum measurement from the tracking system, the particle's mass and therefore the species can be determined. RICH detectors [44] use spherical mirrors to focus Cherenkov light to a ring, the radius of which is a function of θ_{C} and the detector geometry. Fig. 3.15a shows the distribution of θ_{C} as a function of momentum for pions, kaons and protons, illustrating also the separation power of the RICH system.

The momentum spectrum varies according to the polar angle: the smaller θ the harder is the momentum spectrum. Hence the particle identification system consists of two RICH detectors to cover the full momentum range (see Fig. 3.15b).

The RICH1 detector is located upstream of the magnet, at the end of the VELO, covering the full LHCb acceptance. It covers the low momentum

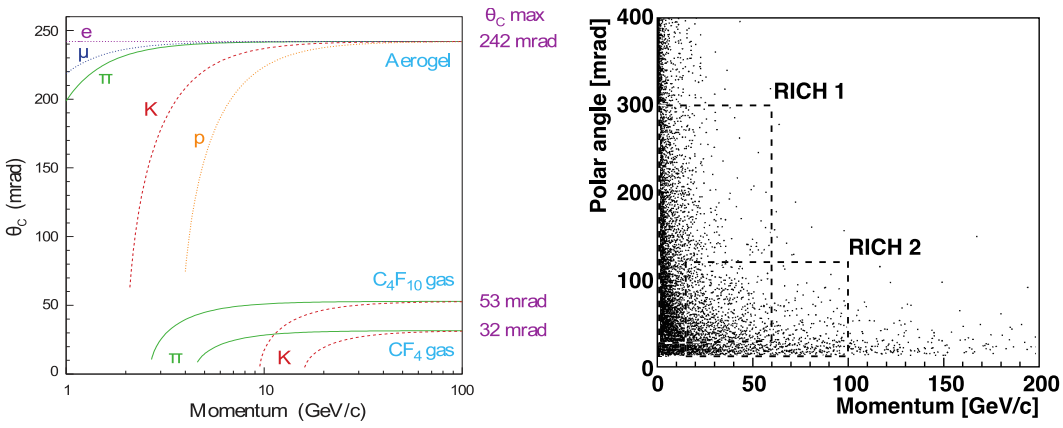

(a) (b)

Figure 3.15: (a) Cherenkov angle versus particle momentum for the RICH radiators. (b) Polar angle as a function of momentum for MC generated pions from $B^0 \to \pi^+\pi^-$. Low momentum, large angle pions are identified by RICH1 and high momentum, small angle pions by RICH2.

range, from 1 GeV/c to 60 GeV/c with the use of 5 cm thick silica aerogel tiles ($n = 1.03$) arranged around the beam-pipe followed by 1 m of C_4F_{10} gas ($n = 1.0014$). In Fig. 3.16a a cosmic event reconstructed by the detector is depicted. The light emitted in the radiators is focused by circular mirrors onto plane mirrors which reflect the light onto an array of Hybrid Photon Detectors (HPDs) which are sensitive to Cherenkov photons with wavelengths in the range 200–600 nm. At the end of 2010 the Cherenkov angle resolution of RICH1 was 1.75 mrad compared to a predicted resolution of 1.55 mrad from Monte Carlo simulated data.

The RICH2 detector is located downstream of the magnet, between the T Stations and the SPD/PS, and has a limited angular acceptance of $\sim \pm 15$ mrad to $\sim \pm 200$ mrad in the bending plane and ± 100 mrad in the non-bending plane. It provides momentum coverage in the range 15–100 GeV/c. A schematic view of RICH2 is shown in Fig. 3.16b.

RICH2 uses a CF_4 radiator ($n = 1.0005$) and a similar mirror arrangement to RICH1. As with RICH1, Cherenkov photons are detected by HPDs. At the end of 2010 the Cherenkov angle resolution of RICH2 was 0.73 mrad compared to a predicted resolution of 0.66 mrad from Monte Carlo simulated data.

The total material contributions of RICH1 and RICH2 are 0.08 and 0.15 radiation lengths, respectively.

The 196 HPDs of RICH1 and the 288 HPDs of RICH2, with 1024 pixels

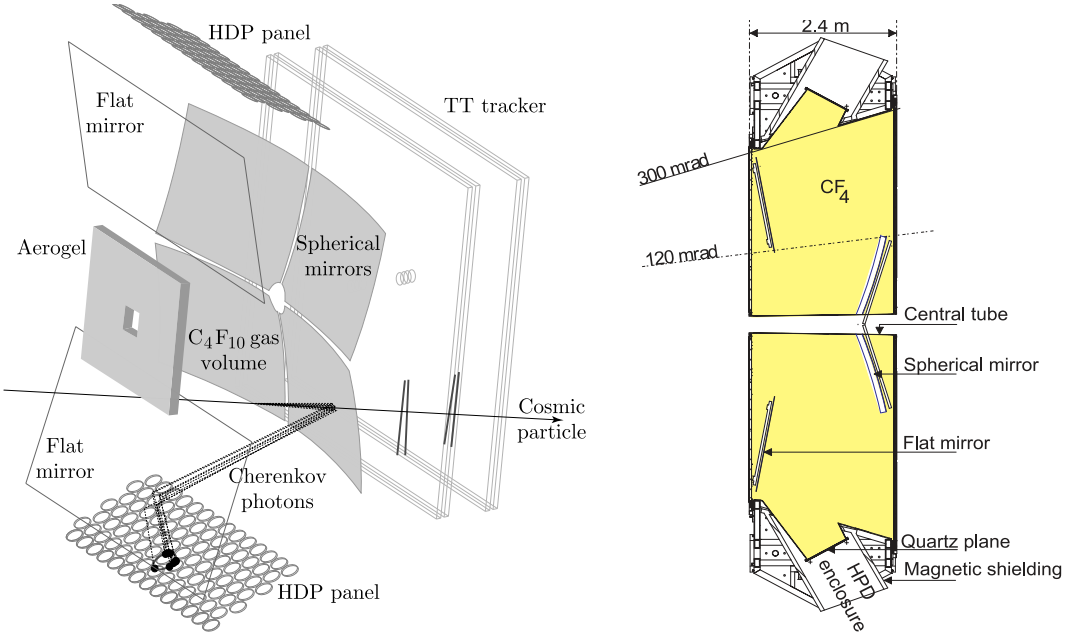

(a) A cosmic event reconstructed in RICH1. (b) Side view schema of the RICH2.

Figure 3.16: The RICH detectors at LHCb.

each, are isolated from the magnetic field. Electron trajectories inside the HPDs are highly sensitive to an external magnetic field, so each tube is protected from the fringe field of the LHCb magnet with a 1 mm-thick cylindrical casing of nickel-iron alloy.

3.4.2.2 Calorimetry

The calorimeter system [45] performs several functions. It selects transverse energy hadron, electron and photon candidates for the first trigger level (L0), which makes a decision 4 μs after the interaction. It provides the identification of electrons, photons and hadrons as well as the measurement of their energies and positions. The reconstruction with good accuracy of π^0 and prompt photons is essential for flavor tagging and for the study of B-meson decays.

A classical structure of an electromagnetic calorimeter (ECAL) followed by a hadron calorimeter (HCAL) has been adopted. The most demanding identification is that of electrons. The electron Level 0 trigger is required to reject 99% of the inelastic pp interactions while providing an enrichment factor of at least 15 in b events. This is accomplished through the selection of electrons of large transverse energy E_{T}. The rejection of a high background of

charged pions requires longitudinal segmentation of the electromagnetic shower detection, *i.e.* a preshower detector (PS) followed by the main section of the ECAL. The electron trigger must also reject a background of π^0 with high E_{T}. Such rejection is provided by the introduction, in front of the PS, of a scintillator pad detector (SPD) plane used to select charged particles. A thin lead converter is placed between SPD and PS detectors.

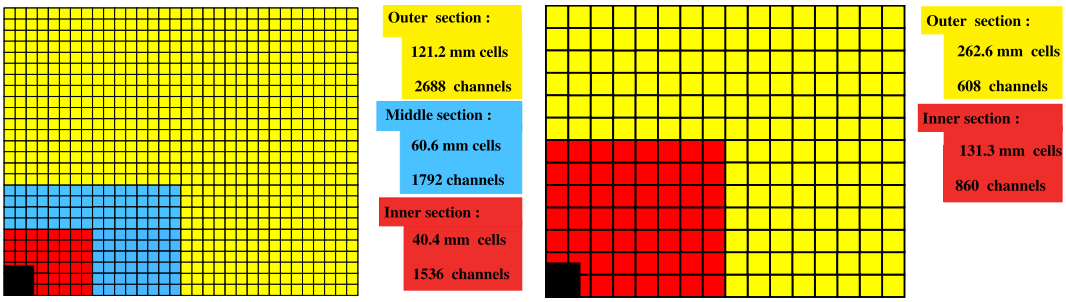

Figure 3.17: Lateral segmentation of the SPD/PS and ECAL (left) and the HCAL (right). One quarter of the detector front face is shown. In the left figure the cell dimensions are given for the ECAL.

The PS/SPD, ECAL and HCAL adopt a variable lateral segmentation (shown in Fig. 3.17) since the hit density varies by two orders of magnitude over the calorimeter surface. A segmentation into three different sections has been chosen for the ECAL and projectively for the SPD/PS. Given the dimensions of the hadronic showers, the HCAL is segmented into two zones with larger cell sizes.

The Scintillator Pad Detector/Preshower detector

The Scintillator Pad Detector/Preshower (SPD/PS) detector consists of a 15 mm, 2.5 X_0 thick, lead converter sandwiched between two almost identical planes of rectangular scintillator pads of high granularity – the SPD before the lead layer, and the PS after – with a total of 12032 detection channels. The sensitive area of the detector is 7.6 m wide and 6.2 m high, and the centers of the two scintillator planes are separated by 56 mm.

The SPD is used to separate photons from electrons at the L0 trigger by making use of the fact that it is a binary –and therefore very fast – detector. Charged particles deposit energy in the scintillator material, while neutral particles do not interact. The amount of deposited energy is converted to a binary 0 or 1 depending on a cell-by-cell threshold value set to minimize photon misidentification while keeping good charged particle identification.

Misidentification comes mainly from photon conversion in the material before the SPD, but also can come from interactions in the SPD that produce charged particles inside it, and backwards moving charged particles, the so-called backsplash [54], that are generated in the lead absorber or in the ECAL. Test beams showed that photons arriving at the SPD with an energy between 20 and 50 GeV have a misidentification probability of 0.8% when applying a threshold of 0.7 Minimum Ionizing Particles (MIPs).

The distinction between charged pions and electrons is done by making use of the electromagnetic shower dispersion measured in the PS. Test beam results show that with a threshold of 4 MIPs, charged pion rejection factors of 99.6%, 99.6% and 99.7% with electron retentions of 91%, 92% and 97% are achieved for 10, 20 and 50 GeV/c momentum particles, respectively. An invariant mass resolution of 7 MeV/c^2 for $\pi^0 \to \gamma\gamma$ is close to expectations from Monte Carlo simulation.

The Electromagnetic Calorimeter

The ECAL is placed at 12.5 m from the interaction point. Its dimensions match projectively those of the tracking system, $\theta_x < 300$ mrad and $\theta_y < 250$ mrad, but its inner acceptance is limited to $\theta_{x,y} > 25$ mrad due to the substantial radiation dose level in that region.

The ECAL thickness, 25 X_0, was chosen so it would contain the full electromagnetic shower of high energy incoming photons in order to ensure optimal energy resolution. Its design energy resolution is given by

$$\frac{\sigma_E}{E} = \frac{10\%}{\sqrt{E}} \oplus 1\% \,, \tag{3.3}$$

where energy is measured in GeV. The first term is the statistical fluctuation of the shower while the second comes from the systematic uncertainties of the calibration.

The Hadronic Calorimeter

The LHCb Hadron Calorimeter (HCAL) is used mainly for trigger and particle identification. It is a sampling device made from iron and scintillating tiles, as absorber and active material respectively. The special feature of this sampling structure is the orientation of the scintillating tiles that run parallel to the beam axis.

The overall HCAL structure is built at a distance of 13.33 m from the

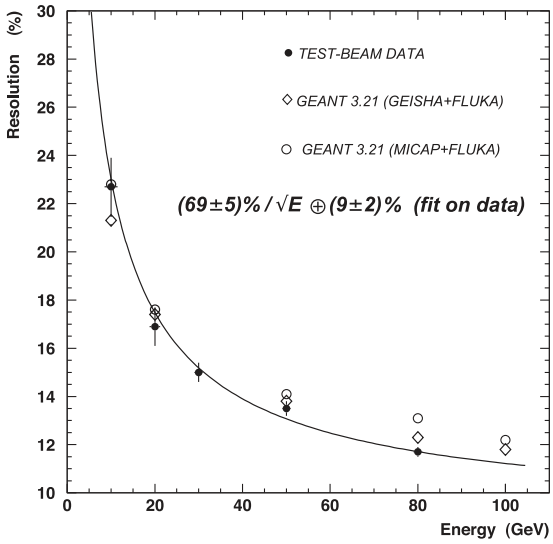

Figure 3.18: HCAL energy resolution, both for data and for simulation with three different hadronic simulation codes. The curve is a fit to the data.

interaction point, with dimensions of 8.4 m in height, 6.8 m in width and 1.65 m in length. Due to limited space in the cavern, the HCAL thickness is only $5.6\,X_0$, which is not enough for containing the full hadronic shower. Therefore, it gives only an estimation of the hadron energy with a design resolution of

$$\frac{\sigma_E}{E} = \frac{80\%}{\sqrt{E}} \oplus 10\% \ , \tag{3.4}$$

where the energy is measured in GeV. It is segmented transversely into square cells of 131.3 mm (inner) and 262.6 mm (outer), as illustrated in Fig. 3.17.

The energy resolution and uniformity of the HCAL were measured at the calorimeter test beam. The resolution extracted from a fit to the data at several energies is shown in Fig. 3.18.

3.4.2.3 The Muon detector

Muon triggering and offline muon identification are fundamental requirements of the LHCb experiment. Muons are present in the final states of many *CP*-sensitive B decays, in particular the two gold-plated decays $B_d^0 \to J/\psi(\mu^+\mu^-)K_s^0$ and $B_s^0 \to J/\psi(\mu^+\mu^-)\phi$. They play a major role in *CP* asymmetry and oscillation measurements, since muons from semi-leptonic B decays provide a tag of the initial state flavor of the accompanying neutral B mesons. In addition, the study of rare B decays such as the flavor-changing neutral current decay,

$B_d^0 \to \mu^+\mu^-$, may reveal new physics beyond the Standard Model.

Muons have a long lifetime $\tau_\mu \approx 2.2\,\mu$s, which means $c\tau_\mu \approx 659\,$m, and a low interaction probability, and thus they fly through the whole detector. Muons are extremely penetrating and therefore muon chambers are installed at the end of the detector, where all other possible charged particles have been filtered. The Muon Detector [50] is composed of five stations, M1–M5, of rectangular shape, with a total of 1380 chambers covering a total area of $435\,\text{m}^2$. Station M1 is located in front of the calorimeters and is used to improve the p_T measurement in the trigger. The inner and outer angular acceptances of the muon detector are 20 (16) mrad and 306 (258) mrad in the bending (non-bending) plane, respectively. Most sensitive layers consist of Multi-Wire Proportional Chambers (MWPCs). The primary aim of the muon system is observation of penetrating charged particles; however, these sensors also provide some momentum and energy information.

The muon identification efficiency has been measured as close to 97% from $J/\psi \to \mu^+\mu^-$ for muon momentum over 10 GeV/c, with excellent agreement with MC simulations.

3.4.3 The Trigger System

With the LHC running under design conditions the rate of pp interactions producing at least two tracks within the LHCb acceptance is 10 MHz. The LHCb detector was designed to only be able to write data to tape at a rate of 2 kHz requiring the trigger to reject 4999 out of every 5000 events. Decays of B mesons used in CP violation and new physics measurements falling within the LHCb acceptance occur at a rate of approximately 10-100 Hz. The LHCb trigger therefore must also be able to identify these relatively rare signals buried within a large amount of uninteresting background.

The LHCb trigger [51] is divide in two levels, shown in Fig. 3.19. The first stage is a hardware trigger known as the "Level 0" (L0) trigger which reduces the rate from 10 MHz to 1 MHz. This is followed by two software "High Level Triggers", HLT1 and HLT2, which reduce the rate to 50 kHz and 2 kHz respectively.

An important feature of the LHCb trigger system is its flexibility. The number of interactions per bunch crossing at the design configuration was expected to be dominated by single interaction due to the relatively low LHCb luminosity of $2 \times 10^{32}\,\text{cm}^{-2}\,\text{s}^{-1}$.The running conditions in 2010 and 2011 have been substantially different than those considered in the design of the trigger system: running at $3.5 \times 10^{32}\,\text{cm}^{-2}\,\text{s}^{-1}$ the experiment is not dominated by

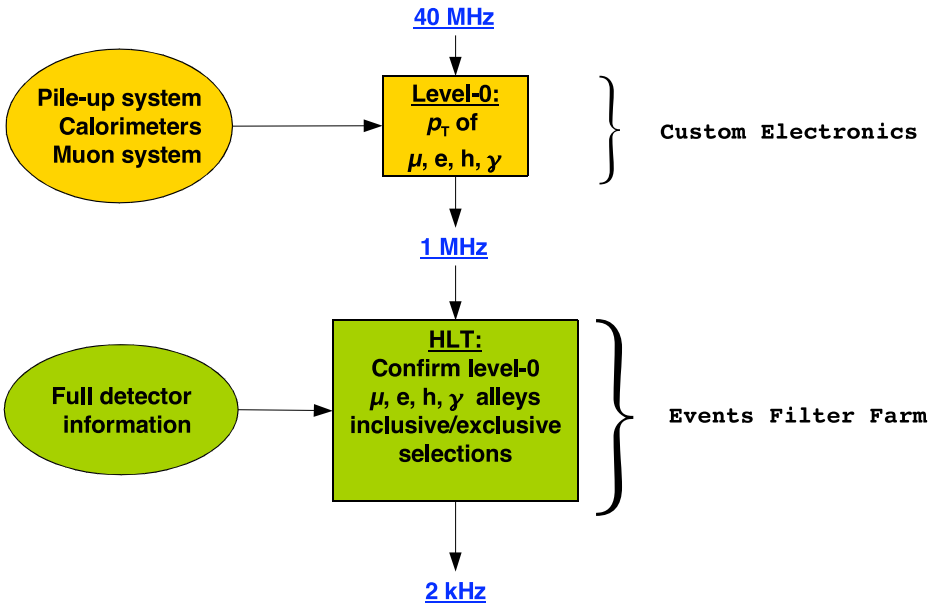

Figure 3.19: Schema of the event flow in the LHCb trigger system.

single interactions and the visible collision rate is 12–15 MHz. This causes the event size to become larger than designed, further changing the trigger working conditions and the storage requirements. The LHCb trigger has been able to adapt remarkably well to these significant modifications of its running conditions thanks to its flexibility, and has provided excellent performance throughout the data taking periods of 2010 and 2011. The output of the trigger in 2011 has been 3 kHz of very clean samples of b and c decays, exceeding the design value of 2 kHz. The output of the trigger planned for 2012 is $\sim$ 4.5 kHz.

3.4.3.1 Level-0 Trigger

The L0 trigger is based on hardware and uses only basic information from the calorimeters and muon system. The L0 muon trigger algorithms or "lines" rely on the standalone momentum reconstruction capability of the muon system which has a resolution of approximately 20%. There are two muon lines: a single muon trigger and a di-muon trigger which look for one and two high momentum muons in the muon stations respectively. Hadrons, electrons and photons are triggered through dedicated lines which use information from the SPD, PS, ECAL and HCAL. Since B meson decay products are usually particles with a large transverse momentum and transverse energy, high p_{T} and E_{T} objects constitute a very clear signature to trigger on. Therefore, the Level-0

trigger focuses on the reconstruction of:

- the highest E_{T} hadron, electron and photon clusters in the calorimeters;
- the two highest p_{T} muons in the muon chambers.

Furthermore, events with high particle multiplicity are rejected in order to reduce the processing time in the HLT.

3.4.3.2 High Level Trigger

The High Level Trigger (HLT) filters events using a software application. It uses the Online Event Filter Farm (EFF), which contains up to 20000 CPU cores, to process and reduce the rate at which events are kept down to ∼3 kHz. The high rate of incoming events from the Level-0 Trigger and the computing power limitation of the EFF do not allow the up-front use of the full event data information in the decision-making process. Thus, the HLT is divided in two stages: the first stage (HLT1) uses only a partial reconstruction to reduce the rate by a factor of ∼ 20 so that the second stage (HLT2) is able to perform full event reconstruction to further discriminate signal events.

HLT1

The HLT1 is designed to minimize the impact of varying running conditions on its performance. It is based around a single track trigger, which searches for a single track with high momentum, a large impact parameter with respect to all primary vertices in the event, and a good track quality. In addition to this, lifetime unbiased muon and electron triggers are used for analyses which are sensitive to the presence of lifetime biases. These latter triggers are based around the confirmation of the L0 trigger decision by matching tracks reconstructed in the HLT to the objects used in the L0 decision, *i.e.*, muon segments or calorimeter clusters.

HLT1 takes ∼15 ms to process a L0-accepted minimum bias event, and accepts ∼5% of such events with an efficiency of more than 80% on signal events for most of LHCb's benchmark B decay modes. The ∼50 kHz selected by HLT1 are passed to HLT2.

HLT2

The combined output rate of events accepted by the HLT1 alleys is sufficiently low to allow an off-line track reconstruction. The HLT-tracks differ from the

off-line in not having been fitted with a Kalman filter to obtain a full covariance matrix since this is too CPU intensive. Prior to the final selection, a set of tracks is selected with very loose cuts on their momentum and impact parameter. These tracks are used to form composite particles, such as $K* \to K^+\pi^-$, $\phi \to K^+K^-$, $D^0 \to hh$, $D_s \to K^+K^-\pi^-$ and $J/\psi \to \mu\mu$, which are subsequently used for all selections to avoid duplication in the creation of final states.

The HLT2 input rate is sufficiently low to perform an almost-full-offline reconstruction, the main difference being that in the HLT2 only tracks with $p_{\mathrm{T}} > 500\,\mathrm{MeV}/c$ and $p > 5000\,\mathrm{MeV}/c$ are reconstructed. Having fully reconstructed events allows the HLT2 trigger lines to use event selection criteria more in line with those used in offline analyses. Furthermore, Global Event Cuts (GEC), such as the reconstructed track multiplicity, are used to reject complex events which require a big amount of processing time.

The HLT2 trigger is made up of a mixture of inclusive, which search for generic B decay features such as displaced vertices or dilepton pairs, and exclusive trigger lines, which select specific decays using similar selections to those used offline. Muon triggers, which select high-p_{T} single or dimuons, used up about another third of the bandwidth. Charm decays accounted for $\sim$1/3 of the HLT2 bandwidth, while the rest was used by several exclusive lines, such as the radiative lines, and inclusive lines such as the ϕ trigger.

3.5 Software framework

The LHCb software is based on the Gaudi framework [55], used for all the applications of the experiment. It has the flexibility needed for running the LHCb chain from the Monte Carlo generation to the real data analysis using the same tools. Data persistency is based on the Root software [56], a framework designed to handle and analyse large amounts of data.

The Gauss software [57] provides the simulation of physics events by running Pythia 6.4 [26], which describes processes up to the Leading Order. The decays of the produced particles are handled either with Pythia or through an LHCb-tuned EvtGen package [58] in the case of B hadrons. The particle-detector interaction is handled by the Geant4 package [59], which is used to transport the particles through the detector. Detector geometry and materials are stored in a database.

The energy depositions in the LHCb detector and the L0 trigger is simulated by the Boole software package [60]. After a Boole pass, the simulated

and the real data can be reconstructed and analysed using the same software.

The MOORE package [61] is used to run the HLT during data acquisition or offline starting from real data or from the output of BOOLE. The trigger is configured via a unique key, called a Trigger Configuration Key (TCK), which defines the sequence of algorithms and their cuts. It is represented by a 32-bit number, with the lower 16 bits reserved for the L0 configuration and the higher 16 bits for the HLT.

Hits and calorimetric depositions are converted into tracks and, eventually, particles by BRUNEL [60]. Event reconstruction is performed by BRUNEL both for real and MC events.

The DAVINCI software package [62] comprises the analysis and selection tools, such as particle identification algorithms, vertex fitting functions. It is also responsible of the administration and running of the *stripping*, a process in which events are further selected for physical analyses.

3.6 Data flow in LHCb

The raw data of the events selected by the trigger system coming from the experiment are further offline processed and then archived. These unprocessed data are used to reconstruct the physical particles, made up from tracks and particle identification information, by making use of the raw information such as the hits or the calorimeter cluster energies. Reconstructed events are saved in a Stripping Data Summary Tape (SDST) file, which contains the necessary information for further event filtering without including the raw data. The SDST files are analyzed in order to filter events for physical analyses by making use of the full reconstructed information and with looser timing constraints than in the HLT. This sequence is known as *stripping*, and finally produces a Data Summary Tape (DST) file, to which the raw data event information is attached. DSTs are the files accessible to scientists for physics analyses. The data are reprocessed several times a year with the improvement of the reconstruction, alignment and stripping software and algorithms.

The stripping is the centralized selection of interesting events run after the reconstruction. Stripped DSTs, stripped events, and stripping selections are the only selections which are run centrally, and therefore the only events and selections which are available for the entire LHCb dataset.

The sequence of selections used to create candidates and select the event is called *stripping line*. Stripping lines are then grouped into *streams*, sets of selections of a similar type, selecting similar events. Ideally no analysis should

have to work with the output of more than one stream. Each stream writes out a different DST with the selected events and candidates from that stream.

4 Signal and Background characterisation

An efficient identification of b-jets from jets of other flavours necessarily has to exploit the kinematic and topological properties of the B hadron decay. The algorithm developed with the aim of identifying and tagging b-jets takes advantage of this knowledge and will be extensively detailed in Sec. 5.

Since the goal of the analysis is to measure the cross section of bottom production in LHCb using inclusive b-flavoured final states, it is also mandatory to investigate the correlations between the produced b quark and the related B hadron, as well as the correlations between the b quark pair and the resulting b-hadron pair: Monte Carlo predictions allow to estimate how much the properties of the quark are modified when going to the hadron level by processes such as fragmentation. The method used here is expected to be less affected by non-perturbative effects than other measurements based on exclusive channel decays.

This chapter discusses the characterisation of signal and background by means of MC simulations.

4.1 Monte Carlo samples

Signal (b-jets) and background (jets from c quarks, light quarks and gluons) description is provided by the LHCb standard MC simulations (see Sec. 3.5).

LHCb Monte Carlo productions of fully simulated events have been used to study properties of b quarks and B hadrons as well as for the study of c and light quarks. This simulations are from the 2010 MC production campaign, called

MC10, in which simulations have been produced with the detector and trigger configurations in use during the 2010 data taking at $\sqrt{s} = 7\,\text{TeV}$ and provide a consistent description of collected collisions. In particular, they reproduce the average visible number of interactions μ in 2010 running conditions which was ≈ 2.5, significantly higher than the value of $\mu = 0.4$ for which LHCb was designed for.

MC10 production of inclusive $b\bar{b}$ fully simulated events have been used to study the properties of b quarks and B hadrons. Simulation makes use of Pythia 6.4 as physics event generator. Proton-proton collisions are simulated at a centre-of-mass energy $\sqrt{s} = 7\,\text{TeV}$. At generator level, at least one B hadron is required to be inside the 400 mrad of acceptance around the z axis with $\mathrm{p}_z > 0$ in order to fully simulate a $b\bar{b}$ event. MC10 simulation has been performed employing the Trigger Configuration Key TCK=0x002E002A (see Sec. 3.5). About one half of 2010 data has been taken under 0x002E002A and 0x002E002C trigger conditions: this is the data sample chosen for the analysis, since these two TCKs differ only slightly from each other and for compatibility with the MC10 production.

4.2 Signal characterisation

The main aim of this section is to investigate the correlations between the b quark and the B hadron, and between the two b quarks and the two B hadrons, in order to develop afterwards a selection procedure that is efficient in selecting signal and effective in rejecting background. By construction, the seed-based jet algorithm is aimed to be capable to directly measure B hadron cross section in LHCb, therefore it relies on how well the measured B hadron approximates the properties of the b quark in order to infer the cross section of b quarks.

Figure 4.1 shows the momentum distribution of b quarks and hadrons before and after requiring them to be inside the detector acceptance: this condition does not affect significantly the p_{T} distribution (Figure 4.1c,d), while it selects significantly more energetic quarks and hadrons (Figure 4.1a,b). However, no relevant differences can be noted between quarks and hadrons, when asking them to be inside the detector acceptance.

On the other hand, Fig. 4.2 highlights a different behaviour of quarks and hadrons with respect to the acceptance cut: uncut distribution of the ratio between the number of hadrons and quarks in bins of momentum is flat around 1 as expected, while low momentum B hadrons are more likely to be in accep-

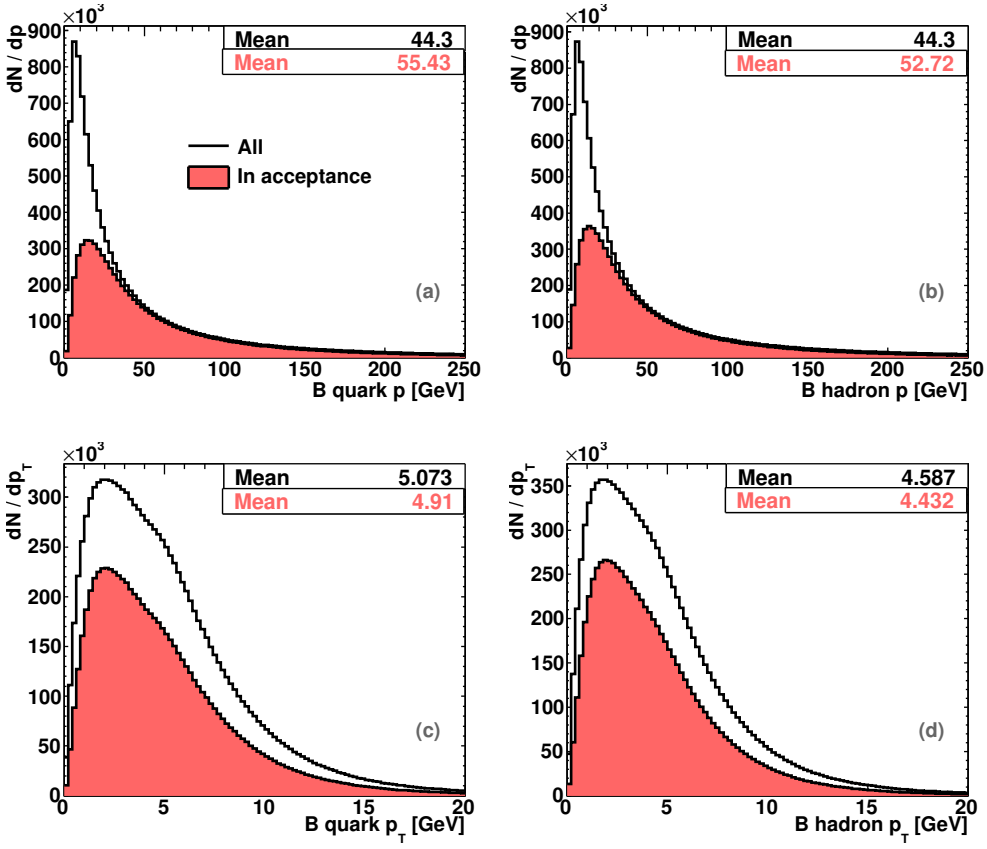

Figure 4.1: Distribution of p and p_{T} of b quarks (left hand plots) and hadrons. In red, distributions for *accepted* quarks and hadrons.

tance than the respective quark. This behaviour is also confirmed by the ratio plotted as a function of p_{T}: at low p_{T}, more hadrons are pushed towards the detector acceptance, while for $p_{\mathrm{T}} > 5\,\mathrm{GeV}$ the initial quark direction is more probable to lie on the acceptance than its relative hadron.

It is nevertheless important to notice that the shape of the ratio distribution in bins of p_{T} proves to be unaffected by the cut on acceptance applied to both b quarks and B hadrons.

In Fig. 4.3 the ratio of the B hadron momentum (p_{T}) and of the b quark is shown. The shape gives an hint of the fragmentation function implemented in Pythia for the b quark hadronisation. Most probable value is close to unity, in most of the cases the p_{T} of the hadron does not deviate significantly from the p_{T} of the quark. Requiring both quark and hadron to be in acceptance

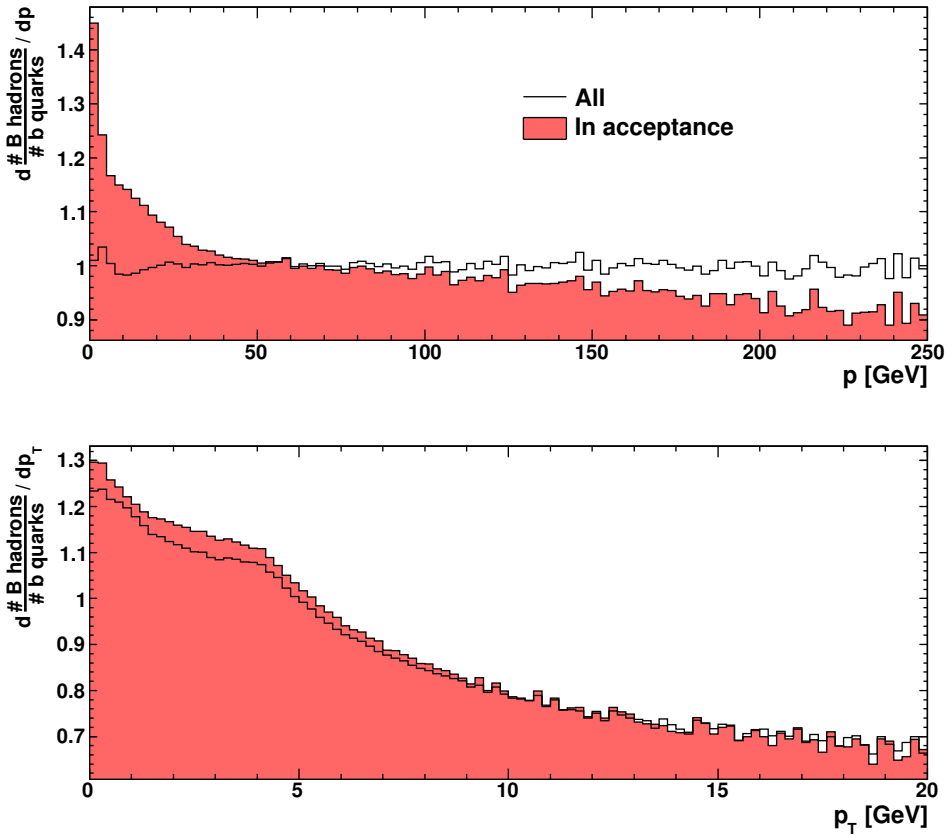

Figure 4.2: Ratio between the number of B hadrons and the number of b quarks in bins of p (top) and p_{T}. In red, distributions when both quark and hadron are in acceptance.

reduces the statistics but does not change significantly the distribution shape.

Figure 4.4 shows the distance between the two quarks of a $b\bar{b}$ pair and between the two hadrons arising from them, expressed in terms of the difference in the azimuthal angle $\Delta\phi$, the pseudorapidity $\Delta\eta$, and $\Delta\mathrm{R} = \sqrt{\Delta\eta^2 + \Delta\phi^2}$. The distributions at the quark level are plotted for the two quarks produced at the interaction, and for the two quarks at the time of their hadronisation. The differences between the distributions are due to the internal implementation of the involved QCD processes (such as gluon emission) within Pythia, that may change the initial quark properties. For our purposes it is however worth emphasising how the B hadron nicely retains the b quark properties at its last

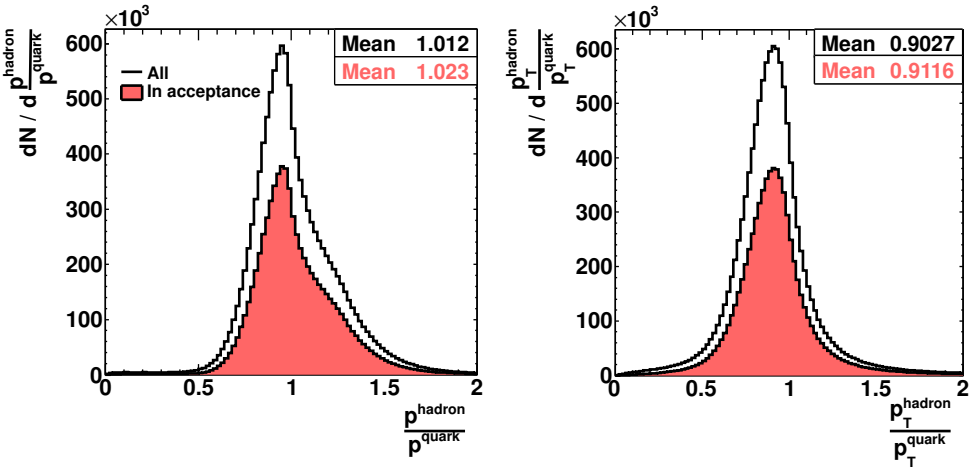

Figure 4.3: Ratio between the p (p_{T}) of the B hadron and the one of the corresponding b quark when both are inside LHCb acceptance.

stage.

The peak at π rad is expected in the $\Delta\phi$ distribution (in Fig. 4.4) due to the production mechanism of flavour creation. An investigation on physics generator behaviour has been done, looking at the different $b\bar{b}$ production subprocesses.

As described in Sec. 2.2.1, three mechanisms contribute to the beauty production at LHCb and are used by PYTHIA to produce $b\bar{b}$ pair: gluon-gluon fusion and $q\bar{q}$ annihilation (flavour creation in hard QCD scattering), flavour excitation (semi-hard process) and gluon splitting (soft process). Flavour creation refers to the lowest-order QCD $b\bar{b}$ production diagrams. Flavour excitation corresponds to diagrams where a $b\bar{b}$ pair from the quark sea of the proton is excited into the final state due to the hard QCD interaction of one of the b quarks with a parton from the other proton. Gluon splitting refers to the processes in which the $b\bar{b}$ pair arises from a $g \to b\bar{b}$ splitting in the initial or final state. Neither of the quarks from $b\bar{b}$ pair participate in the hard QCD scattering in this case.

Figure 4.5 shows the distribution of $\Delta\phi$ for b quark pairs produced via flavour creation: it is clear the back-to-back feature of this process. ΔR then results in a more symmetric distribution around π. It is important to emphasize here that the study presented in this section is based on PYTHIA, where NLO interference among production processes is not described.

A direct comparison between the b quark and the related B hadron has

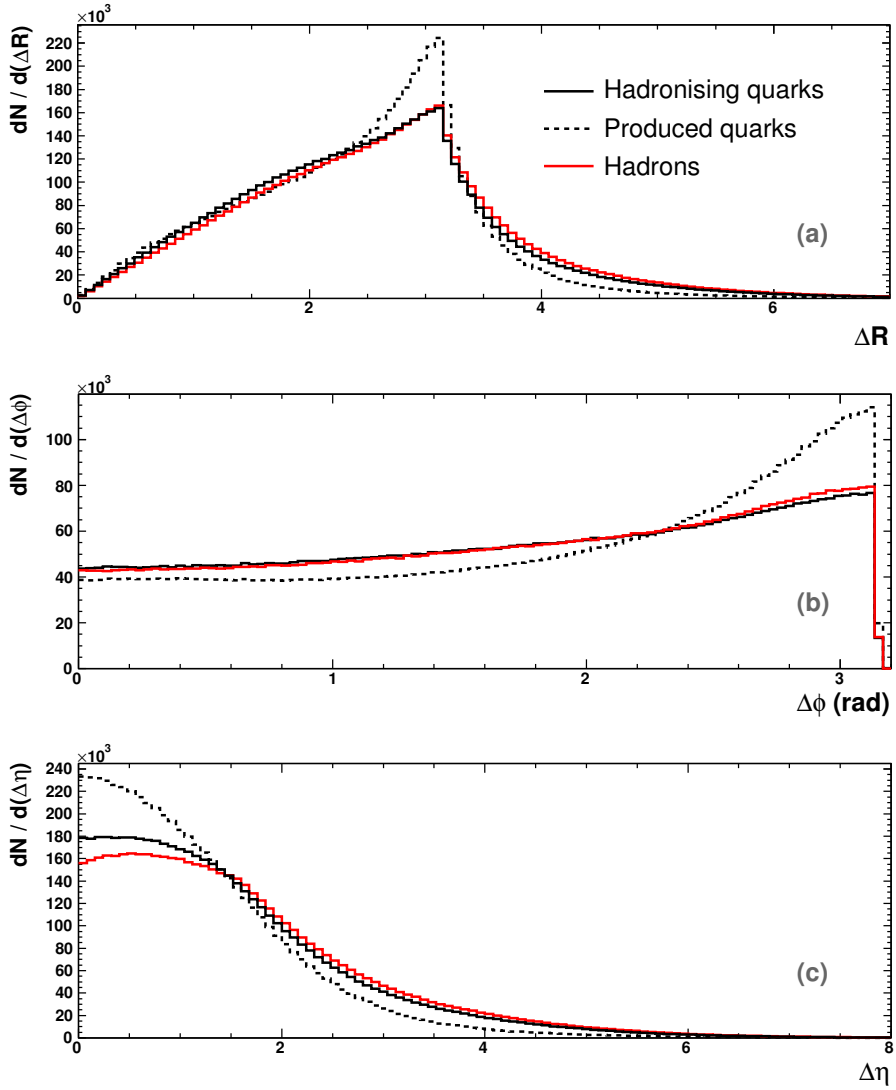

Figure 4.4: ΔR (a), $\Delta\phi$ (b) and $\Delta\eta$ (c) between the b and $\bar{b}$ quarks: distributions are shown at the very first PYTHIA production step (dashed line) and at the last one before hadronisation (continuous black line). In red, distributions for the B hadron pairs.

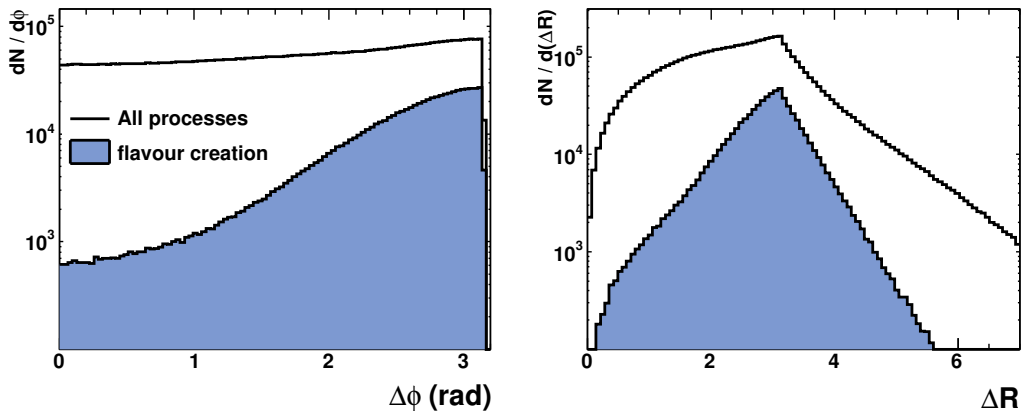

Figure 4.5: $\Delta\phi$ and $\Delta\eta$ between the two quarks of a $b\bar{b}$ pair (black line). In blue, when the $b\bar{b}$ pair is produced via flavour creation.

been obtained using PYTHIA 8 [63]. It is presented in Fig. 4.6, where the ΔR between them is plotted together with the ΔR between the quarks at production and hadronisation level. The quark and the hadron are mostly close each other, with a distance in the (ϕ, η) plane lower than 1.

In Fig. 4.6 a rather unexpected bump can be observed near $\Delta R = 3.0$ in the quark-quark distribution. This behaviour has been investigated with PYTHIA 6.4, where the bump is event more pronounced, as it is clear from Fig. 4.7. It is also clear that the issue does not affect all production mechanisms and turns out to be related to how the PYTHIA event history is traced by HEPMC [64], the interface to PYTHIA implemented in GAUSS. The discrepancy found between the two quark stages (production and hadronisation) forced to choose one of them as reference for the b quark. If not otherwise stated, the b quark at the hadronisation level is considered hereafter [65].

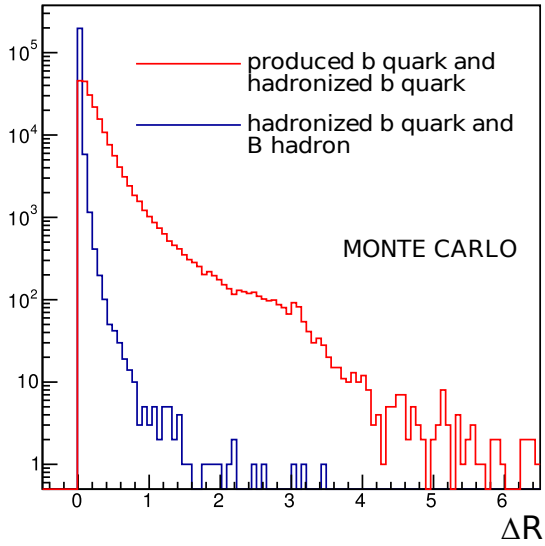

Figure 4.6: ΔR of b quark at production and hadronisation stage (red). In blue, ΔR between the hadronising quark and the related hadron. Results from PYTHIA 8.

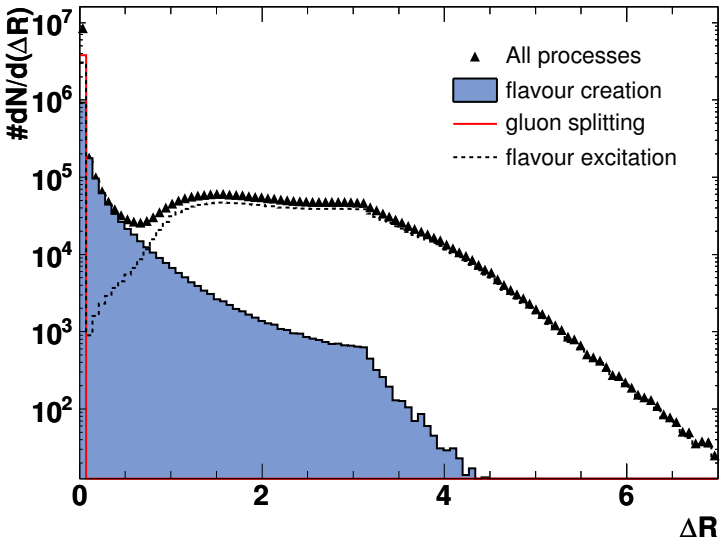

Figure 4.7: ΔR of b quark at production and hadronisation stage for different production mechanisms as found in PYTHIA 6.4.

4.3 Physical Background characterisation

The background for the analysis consists of a *physical* component, mainly made of hadronic jets arising from the hadronisation of charm, light quarks and gluons, and a *combinatorial* background, defined as events in which a $b\bar{b}$ pair has been actually produced and the seed algorithm reconstructs jets not physically associated to any signal quark. The combinatorial part requires a definition of seed or jet in order to be investigated and will be approached in Sec. 5.

This section illustrated the features of production and hadronisation of $c\bar{c}$, by far the main source of physical background, compared with $b\bar{b}$.

Monte Carlo simulations of inclusive $c\bar{c}$ events in pp collisions at $\sqrt{s} = 7\,\text{TeV}$ have been used, with exactly the same production settings as for $b\bar{b}$ inclusive production. Here the fundamental generator cut is to ask at least one charmed hadron inside the 400 mrad acceptance around the z axis with $\mathrm{p}_z > 0$.

Fig. 4.8 and 4.9 show the momentum and the p_T of c quarks and c-hadrons respectively. The shape of these distributions is compared with the corresponding ones from beauty quarks and hadrons. The transverse momentum of the b quark is in average roughly twice the c quark p_T. This difference further increases in the case of hadrons. Looking at high p_T secondary vertices (here also referred to as *seeds*) therefore has a discriminating power also against the charm background.

Fig. 4.10 illustrates the ratio between the momentum of the c-hadron and the one of the corresponding c quark, compared with the distribution for b quarks. While the B hadron retains the most of the energy of the original b quark, in the case of charm production a larger part of the initial quark energy is carried away in the fragmentation process.

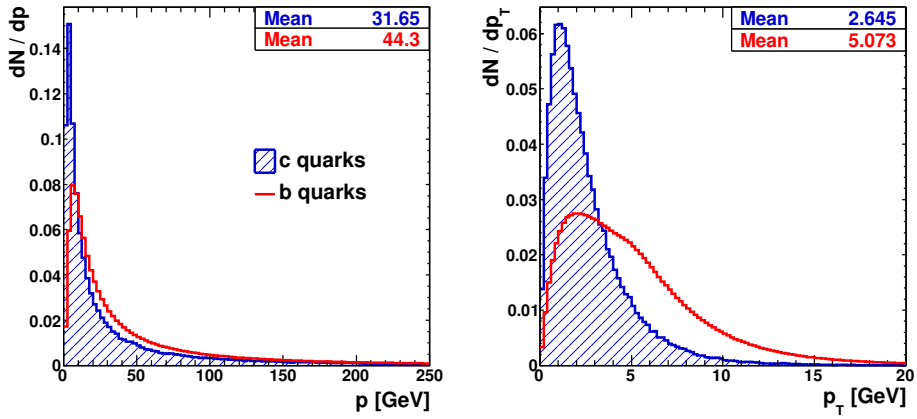

Figure 4.8: Momentum and transverse momentum of c quarks (blue) compared with b quarks. Quarks are required to be inside the LHCb acceptance.

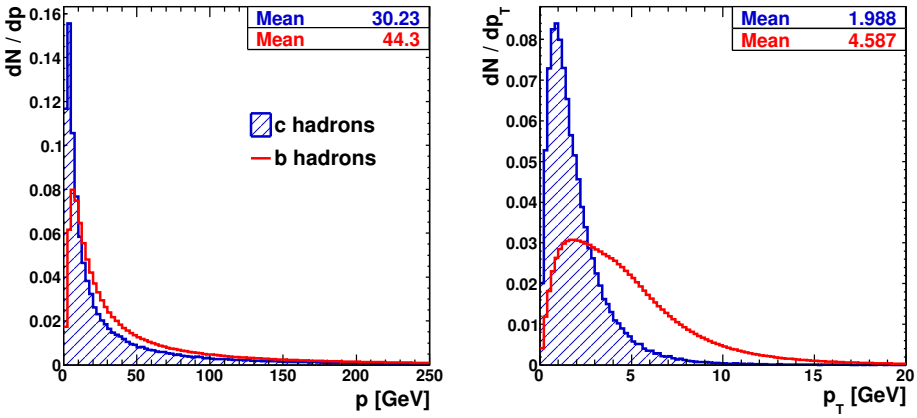

Figure 4.9: Momentum and transverse momentum of c-hadrons (blue) compared with b-hadrons. Hadrons are required to be inside the LHCb acceptance.

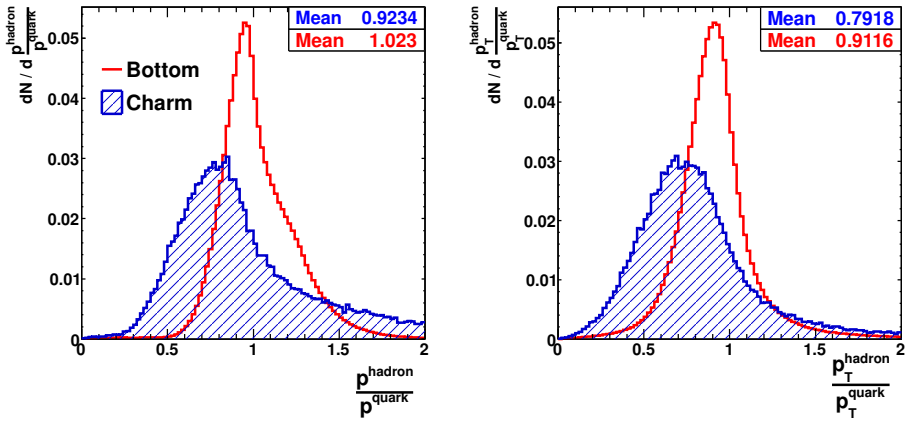

Figure 4.10: Ratio between the p (p_{T}) of the c-hadron (blue, filled) and the one of the corresponding c quark when both are inside LHCb acceptance. Distributions for b quarks and hadrons are also shown for shape comparison.

5 Signal Selection

In comparison to other experiments, the LHCb detector features an outstanding capability to identify displaced secondary vertices with respect to the interaction point. This is a mandatory achievement for its main purpose of studying B rare decays and the CP violation in the B-meson system and it is ensured by its high-resolution Vertex Locator.

The VELO provides a good spatial resolution for *vertexing* and allows to measure the time of flight. The extraordinary performance of the whole LHCb tracking system (see Sec. 3.4.1) makes possible accurate measurements of particles' trajectories and momenta. Many lifetime and kinematic based properties of the decay of B hadrons are at the basis of the identification of b-quark jets (b-tagging), thus the LHCb detector could prove to be suitable to perform QCD studies based on heavy-quark jets.

The LHCb has a peculiar single-armed forward geometry, for which it covers only 4% of the total solid angle around the interaction point. Standard jet algorithms such as k_t [66], anti-k_t [67] and the cone algorithm family [68], mainly developed within 4π experiments, need to be adapted in order to be used in this experimental context and to exploit the main capabilities of the detector.

5.1 Introduction

The most significant property of the B hadron is its long lifetime of about 1.5 ps ($c\tau \approx 460\,\mu\text{m}$) in the rest frame. Due to the large boost at which they are produced in the LHCb frame, the average flight distance is of the order $\mathcal{O}(1\,\text{cm})$,

hence the B hadron decay is characterized by a displaced secondary vertex (SV). The charged particle tracks associated to the SV are distinguishable from the *prompt* tracks coming from the pp collision by their *impact parameter* (IP) with respect to the PV. Jets from light flavour hadrons or gluons contain basically no displaced vertex and a suppression of the background due to these component is easy to achieve. On the other hand, collisions with c-jets in the final state have similar topology due to the non-negligible lifetime of c-mesons, thus the lifetime-related variables turn out to be less effective in discriminating this background. Fig. 5.1 illustrates the topology of a long-lived heavy hadron decay compared to light jets.

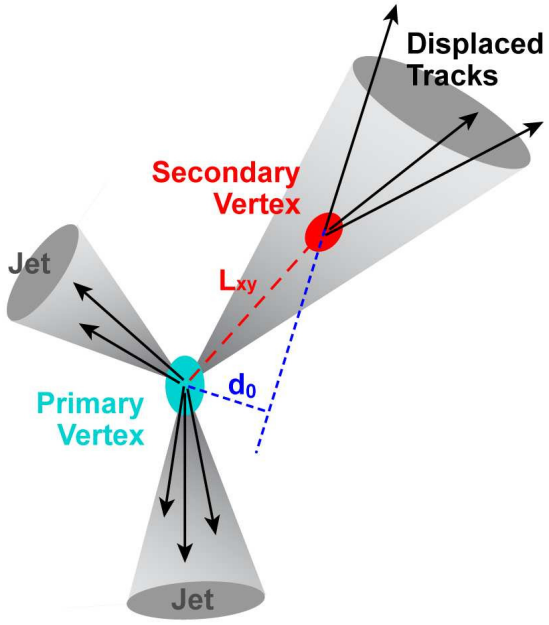

Figure 5.1: Schematic diagram of a long-lived particle decay that travels a distance L_{xy} before decaying at the secondary vertex. The tracks from the decay have a large impact parameter d_0. Light jets are also depicted, whose tracks are compatible with the PV.

Other properties of B mesons that may be exploited for background rejection are their large mass and charged track multiplicity in the final state. Due to the hard b fragmentation function the b-hadron carries a large fraction of the total jet energy.

The jet reconstruction tool developed to identify the jets originating from the b quark hadronisation is a *cone-type seeded* algorithm: the basic idea is to

take an inclusive secondary vertex originating from the long-lived B hadron as *seed* for jet reconstruction. The position of the seed with respect to the PV establishes the direction of a cone of given aperture. The jet is then built collecting charged and neutral particles that are found to be inside the cone. The radius of the cone is expressed in terms of the dimensionless parameter R_c in the (ϕ, η) plane, thus a particle i with azimuthal angle ϕ_i and pseudorapidity η_i is taken if

$$\Delta R_i = \sqrt{(\phi_0 - \phi_i)^2 + (\eta_0 - \eta_i)^2} < R_c \tag{5.1}$$

where (ϕ_0, η_0) is the seed position in the (ϕ, η) plane.

The method is physically justified by the fact that the mass of the b quark is heavy, and hence the B hadron is close to the quark level (see Sec. 4.2), depending less on the fragmentation process than the measurements based on exclusive decay channels. One advantage of this method is the high statistics accessible, which allows to explore angular correlations between the $b\bar{b}$ pairs and a larger kinematic region compared to exclusive reconstructions.

5.2 Event Selection

Candidate events are firstly selected on the basis of the L0 and HLT trigger decision. The events used are triggered by the presence of a high p_T particle with high impact parameter, and selected at the HLT trigger level by the possible presence of a decaying B hadron.

Since the real data for physics analysis have been further reprocessed and filtered through the stripping process (see Sec. 3.6), they are only available in stripping streams which are sets of selection lines. The choice for this analysis fell naturally on the Bhadron stream, which is the collection of stripping lines that select events on the basis of the possible presence of a decaying B hadron. In order to keep systematics under control, only a handful of Bhadron stripping lines has been considered.

The choice of the trigger lines as well as of the stripping lines has also been made in order to comply as much as possible with the requirement of inclusiveness of this analysis. Both simulations for MC studies and real data for the extraction of the $b\bar{b}$ cross section have been treated using the same trigger and stripping strategy, in order to avoid biases which they are likely to introduce.

Trigger and stripping strategies will be motivated and discussed in detail in Sec. 5.5.

The event selection also requires that one, and only one, primary vertex is

recontructed. Primary vertices are determined by at least 5 charged particles (see [69] for details on the LHCb standard PV reconstruction). This requirement reduces significantly the statistics given the conditions of the considered runs, where the average number of pp interactions is ~ 2.0. This acts as a Pile-Up Veto, *i.e.* rejecting events in which there is more than one pp interaction, in order to avoid the difficulty of assigning the reconstructed seed to the corresponding PV. This choice has an impact on the integrated luminosity of the data sample used for the measurement: it needs a careful evaluation as done in Sec. 6.2.

Events are finally required to have at least one secondary vertex, the seed, reconstructed using tracks with high impact parameter with respect to the PV, as described in the following section.

Samples of MC simulated events corresponding to minimum bias (MB) pp collision processes (MC10) have been used, in addition to the MC samples presented in Sec. 4.1, to study the component of light quarks and gluons.

5.3 The Seeding Algorithm

The seeding algorithm is a procedure to search for a pair of tracks that form a good vertex and are likely to be part of the decay products of a B hadron. Seed track candidates are properly preselected from the list of charged *long* tracks (see Sec. 3.4.1.5) of the event, with requirements on transverse momentum, χ^2 of the resulting track fit and impact paramenter significance IPS ($= \mathrm{IP}/\sigma_{\mathrm{IP}}$) with respect to the PV. The cuts applied are summarized in Tab. 5.1. All the charged tracks are reconstructed assuming a pion mass hypothesis.

	Cut
Track momentum	> 2.0 GeV
Track p_T	> 0.6 GeV
First track χ^2/ndf	< 2.5
Second track χ^2/ndf	< 3.0
IPS wrt PV	> 2.5

Table 5.1: Cuts used for the selection of seed track candidates.

The default LHCb vertex fitter OfflineVertexFitter [70] is used to fit a secondary vertex with preselected pairs of tracks (namely i and j). Reconstructed vertices are kept if they meet the requirements listed in Tab. 5.2. Tracks are required to have opposite charge in order to reject part of the com-

	Cut
Sum of tracks charge	0
Seed p_T	> 1.0 GeV
$z_{\mathrm{SV}} - z_{\mathrm{PV}}$	> 1 mm
Secondary vertex χ^2/ndf	50
DOCA	< 3 mm
ΔR_{ij}	< 1.4
$\lvert M_{\mathrm{seed}} - M_{K^0_{\mathrm{S}}} \rvert$	$> 10\,\mathrm{MeV}$
$\lvert M_{\mathrm{seed}} - M_{\Lambda} \rvert$	$> 10\,\mathrm{MeV}$

Table 5.2: Requirements on the reconstructed two-track secondary vertices.

binatorial background. A cut on the p_{T} of the seed candidate is applied, which is defined as the sum of four-momenta of constituting tracks. A minimum distance Δz to the PV is required for seeds, which must not be upstream with respect to the PV. Tracks are also required not to exceed a maximum angular separation, thus a constraint on ΔR_{ij} is imposed. Goodness of vertex is ensured with cuts on the resulting vertex fit χ^2 and on the distance of closest approach between the two tracks (DOCA). A constraint on the invariant mass of the seed has been put in order to reject two-body decays of long-lived particles, such as K^0_{S} and Λ^0.

Tracks can be part of more than one seed, therefore a seed selection is performed making a recursive loop over the set of seeds. The seeds are sorted according to the sum of seed track IPS and the ones that share one track with the highest IPS seed are removed.

Seeds are considered as *signal* if both tracks belong (according to MC truth information) to the decay of the same B hadron. Whenever a seed contains at least one track not belonging to the decay products of a B hadron, or two tracks coming from different B hadrons, the seed is considered as *combinatorial* background (misreconstructed signal).

MC10 inclusive $b\bar{b}$, $c\bar{c}$ and minimum bias are used in Fig. 5.2 to compare some basic seed variables. The distributions are normalized to the same area, in order to emphasize the differences in shape. The sum of seed track IPS shows a discriminating power when comparing the one from correctly reconstructed B hadron decay vertices with the one from both charm and light contributions. The average p_{T} of b- and c-seeds are comparable, being both in average about twice the p_{T} of non-heavy quark seeds.

The multiplicity of reconstructed seeds (number of reconstructed seed can-

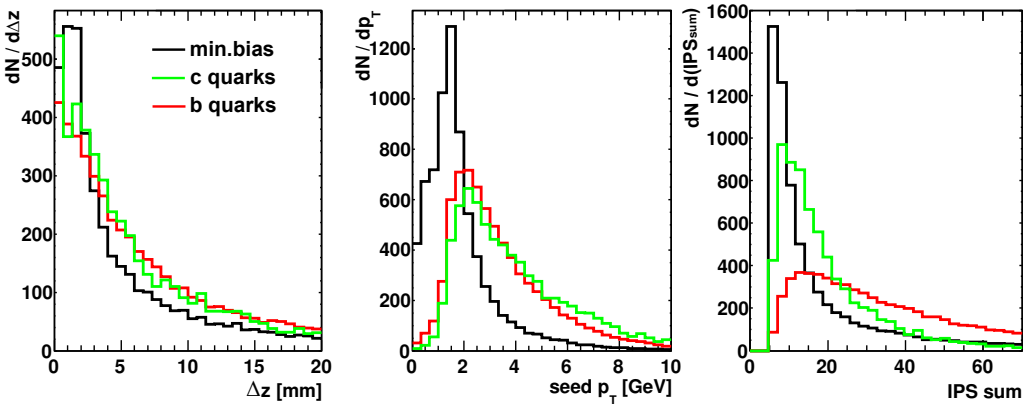

Figure 5.2: Distributions of $|z_{\text{seed}} - z_{\text{PV}}|$, seed p_{T} and sum of seed track IPS, for seeds from b, c and light component. Distributions are normalized to the same area for shape comparison.

didates per event) for the MC10 $b\bar{b}$ inclusive sample which passed the trigger selection is shown in Fig. 5.3. The number of reconstructed seeds with respect to the number of true B hadrons within LHCb acceptance is also shown. Some inefficiency of the seeding procedure is observed, since in an important fraction of events the number of true B hadrons in acceptance is higher than the number of reconstructed seeds. Also, in some cases the seeding algorithm reconstruct more seeds than the actual number of B hadrons in acceptance. A seed merging procedure could be thought to minimize these instances.

The reconstructed seed are found to describe well the B hadron direction: the ϕ and θ resolution evaluated for signal seeds turns out to be (15.8 ± 0.2) mrad and (1.82 ± 0.18) mrad respectively. The quoted number has been extracted from the Gaussian fit to the $\Delta\phi = \phi_{rec} - \phi_{true}$ and $\Delta\theta = \theta_{rec} - \theta_{true}$ distributions (*cf.* Fig. 5.4), with $\phi_{rec}(\theta_{rec})$ denoting the azimuthal (polar) angle of the reconstructed seed and ϕ_{true} (θ_{true}) the angle of the corresponding B hadron decay point (extracted from MC simulations).

The separation between two seeds in $\Delta\phi = |\phi_1 - \phi_2|$, $\Delta\eta = |\eta_1 - \eta_2|$ and $\Delta R = \sqrt{(\Delta\phi)^2 + (\Delta\eta)^2}$ has been studied and it is shown in Fig. 5.5. It can be observed that there is a significant contribution from seeds coming from the same B hadron, which ideally should correspond to a single reconstructed seed.

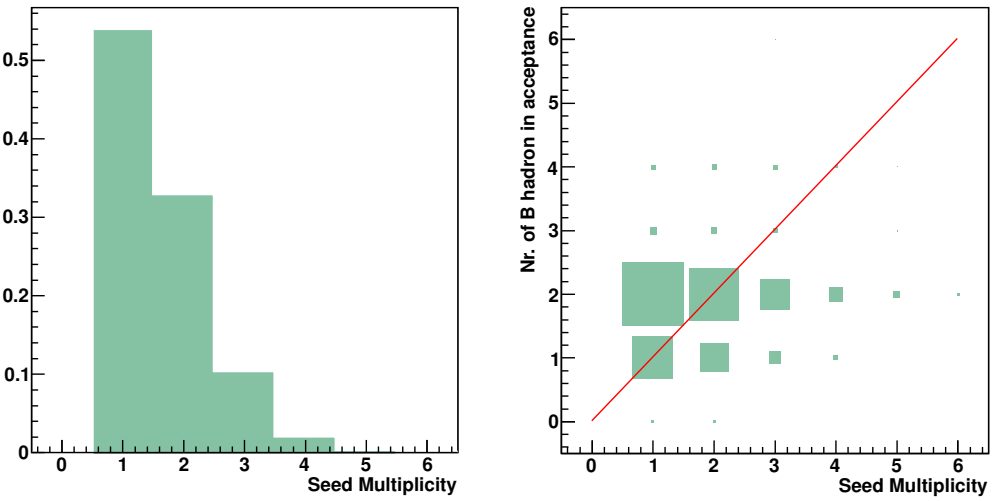

Figure 5.3: Multiplicity of reconstructed seeds (*left*). Seed multiplicity against the number of B hadrons inside LHCb acceptance (*right*).

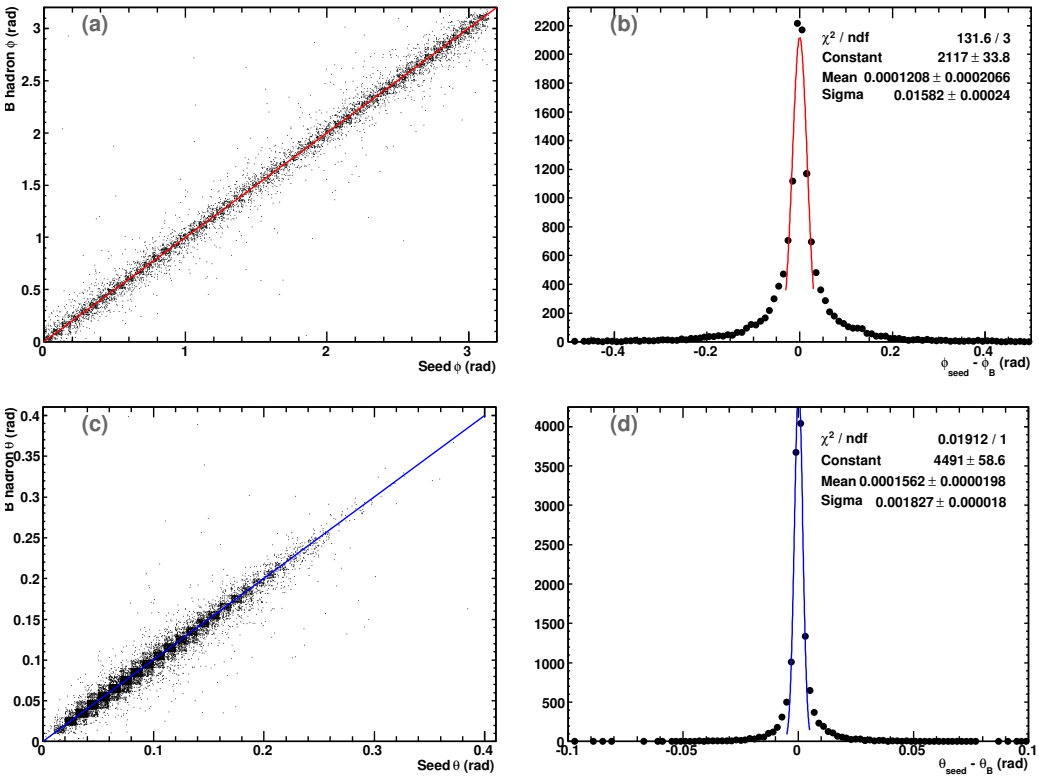

Figure 5.4: Plot a (c): signal seed ϕ (θ) with respect the corresponding B hadron ϕ (θ). Signal seed ϕ (θ) resolution in b (d).

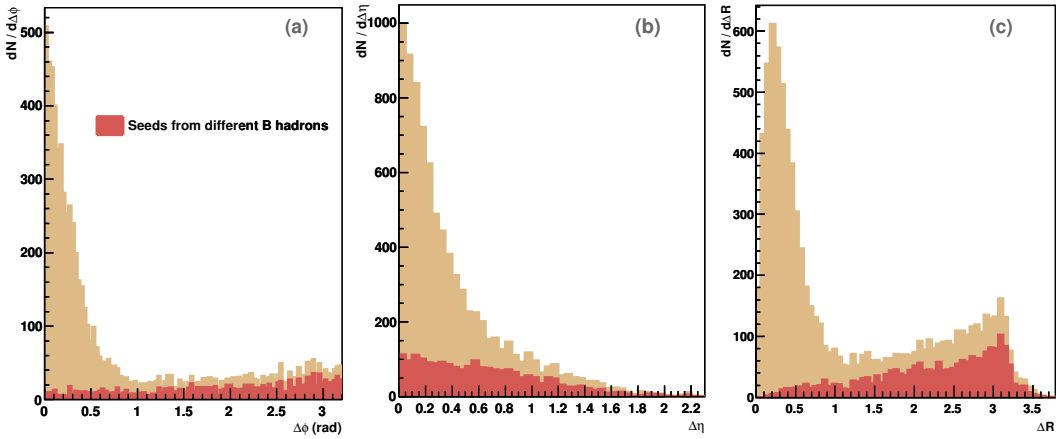

Figure 5.5: Separation of two seeds in: (a) $\Delta\phi$, (b) $\Delta\eta$, (c) ΔR defined in the text. The contribution from signal seed pairs coming from different B hadrons is superimposed in red. Total distributions in light brown. Normalised distributions for MC10 $b\bar{b}$-inclusive events with at least one seed and positive physics trigger decision.

5.3.1 Seed Merging

Reconstructed pairs of seeds having $\Delta\phi \sim 0$ are very likely to come from the same B hadron or from the chain $B \to D$, as it can be seen in Fig. 5.6, which shows the $\Delta\phi$ of two seeds in events with a single B hadron in acceptance. Such seed pairs are merged into a single seed, assigning to the resulting seed the best possible parameters.

Two seeds are merged into a single seed if the invariant mass of all the tracks in the two seeds is below 4.0 GeV (see Fig. 5.7). Low values of invariant mass correspond to a majority of seed pairs having low $\Delta\phi$, as can be observed in Fig. 5.7. A new vertex fit is not performed, instead the merged seed inherits the spatial position from the best seed in terms of DOCA of seed tracks. All the seed tracks of the initial two seeds are assigned to the new one.

The seed merging procedure allows to reduce significantly the fraction of fake seeds affecting strongly low $\Delta\phi$ region. Fig. 5.8 illustrates the effect of merging by comparing the seed pair $\Delta\phi$ before and after the merging procedure.

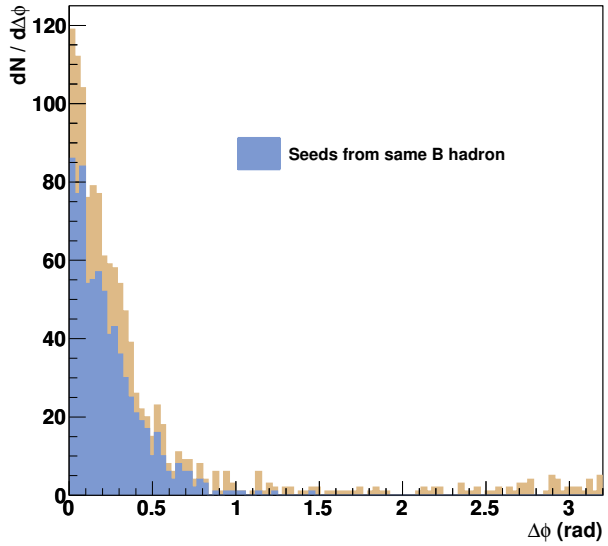

Figure 5.6: $\Delta\phi$ between two seeds in events with 1 B hadron in acceptance. In blue the component from seed pairs related to the same B. Total distribution in light brown.

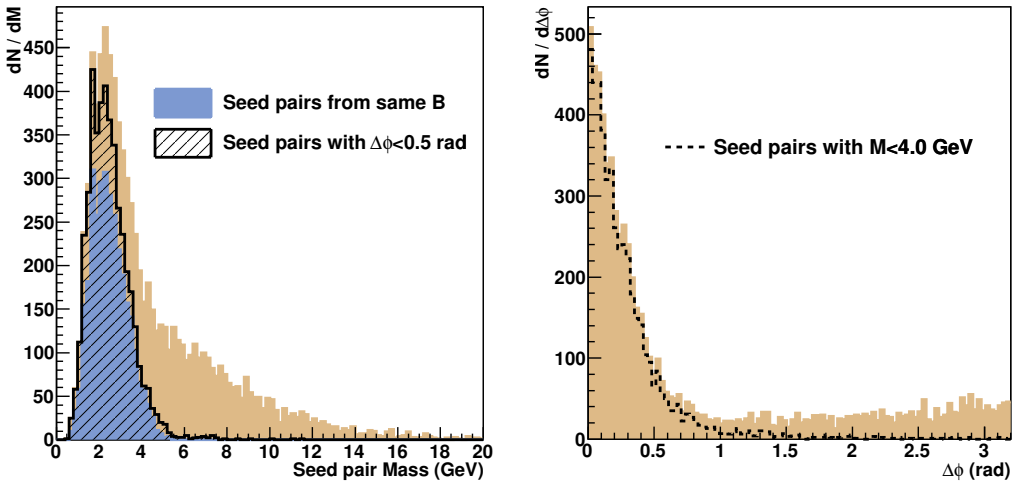

Figure 5.7: *Left*: invariant mass of two seeds. Distribution for seed pairs with $\Delta\phi < 0.5\,\text{rad}$ is also shown. *Right*: $\Delta\phi$ of two seeds. Dashed line distribution is for seed pairs with invariant mass $M < 4.0\,\text{GeV}$. Total distributions in light brown.

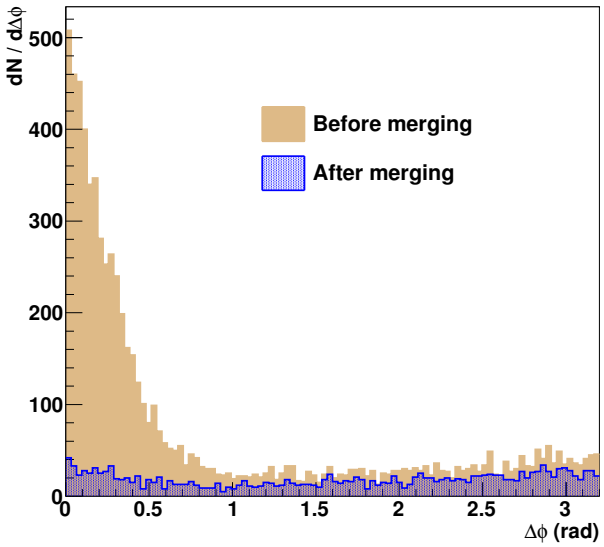

Figure 5.8: $\Delta\phi$ between two seeds before and after the merging procedure. Total distribution in light brown.

5.3.2 *b*-tagging Efficiency

By construction, the b-tagging of the jet algorithm is implicit in the seeding procedure: seed secondary vertices are selected having in mind the features that characterise the decay of B hadrons.

To measure the inclusive b-jet production cross section, the b-jet tagging efficiency obtained by the seeding algorithm must be estimated. The efficiency is estimated using Monte Carlo simulations. It is defined as the ratio of the number of signal seeds and the number of generated B hadrons in the LHCb acceptance. Only B hadrons which are not excited states (*e.g.* B^*, B^{**}) are counted, in order to avoid double counting when using the MC simulation. Only signal seeds have been considered, *i.e.* those with both tracks positively truth-matched to the same B hadron. The seeds associated to the same B hadron have been counted only once.

The tagging efficiency as a function of the reconstructed seed multiplicity is listed in Tab. 5.3, together with the fraction of fake seeds, defined as the ratio of the number of seeds with no tracks originated from B decay and the total number of reconstructed seeds. The quoted numbers have been obtained from the Monte Carlo events with positive trigger decision after the merging procedure.

Seed multiplicity	Efficiency (%)	Fraction of fake seeds (%)
1	52.8 ± 0.4	1.68 ± 0.14
2	78.5 ± 0.7	7.6 ± 0.4
≥3	80.4 ± 2.3	18.16 ± 1.9

Table 5.3: b-tagging efficiency and fraction of false seeds for different seed multiplicities.

The average fraction is:

$$\epsilon_{\text{tag}} = (59.0 \pm 0.4)\% \tag{5.2}$$

The average fraction of fake seeds is estimated using Monte Carlo simulations to be:

$$\epsilon_{false} = (2.92 \pm 0.13)\% \tag{5.3}$$

Although The seed merging procedure reduces the number of seeds by about 24%, it does not affect substantially the tagging efficiency, which was estimated to be $\epsilon'_{\text{tag}} = (59.7 \pm 0.4)\%$ before merging any seeds. Fake seed component is therefore the most affected one, being reduced from $\epsilon'_{false} = (3.58 \pm 0.14)\%$ before the merging stage.

A data-based cross-check of the procedure to determine the b-tagging efficiency obtained by the seeding procedure has been made elsewhere ([71]), with a three-track seeding technique using events where a B hadron is fully reconstructed. The method performs the seeding with the set of particles obtained excluding the ones originating from the fully reconstructed B signal. MC and data estimation proved to be in reasonable agreement.

5.4 Jet Reconstruction

The line of flight of B hadrons is reproduced with good precision by the position of the seed with respect to the primary vertex, as shown in Fig. 5.4. Jets are then built adding up to the seed the four-momentum of charged (*long* and *upstream*) and neutral particles that are found to be inside a cone, whose axis coincides with the seed trajectory and is left unchanged by this procedure.

Let R_{c} be the radius of the cone, in terms of the R parameter defined in Eq. 5.1. Commonly used values of R_{c} in cone algorithms range from 0.4 to 1.0 [72]. Fig. 5.9 illustrated the p_{T} of hadronic jets at generator level using MC10 $b\bar{b}$ inclusive: they are constructed following the procedure explained before

using different values of R_c around the generated B hadron flight direction. Some hints of what would be an appropriate value of R_c can be obtained from Fig. 5.9, where generated stable or visible particles[1] that are truth-matched to a b quark are used to build the p_T of such "true" jets. B hadron p_T is also presented for comparison. Unless otherwise stated, in the present chapter a value $R_c = 0.7$ is assumed.

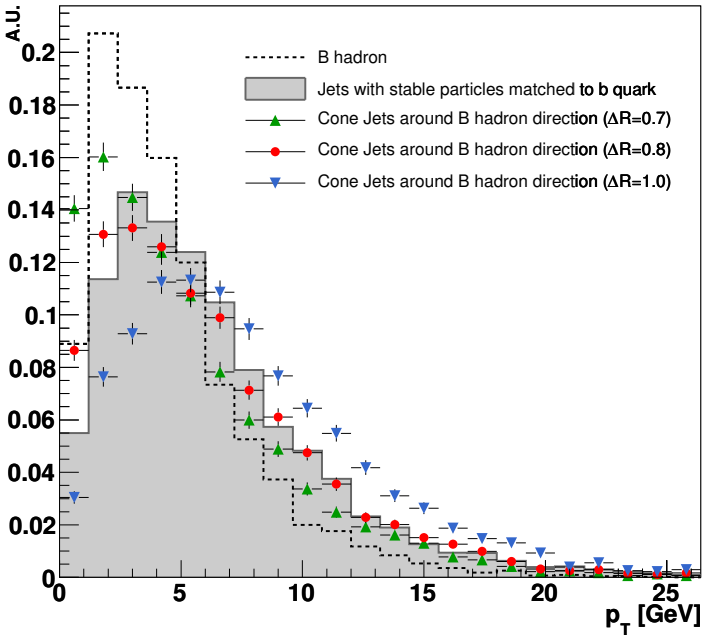

Figure 5.9: Filled grey histogram: total p_T of stable generated particles associated to the b quark fragmentation. Coloured markers: p_T of cone jets built around B flight direction with visible generated particles with different values of R_c. B hadron p_T is the dashed line distribution. Event generator is PYTHIA 6.4.

5.4.1 Jet Merging and Splitting

In the jet clustering procedure, additional tracks are initially left free to be assigned to one or more jets in order to study jet overlapping. A criterion must be worked out to merge or split overlapping jets. Total and charged

[1] *Stable* particles are meant to be any final state related to the b quark fragmentation, stable enough to cross the detector. *Visible* particle definition includes all stable particles which the detector is capable to distinguish with good efficiency: they basically do not include neutrinos.

track multiplicity of jets in MC10 $b\bar{b}$ inclusive sample is shown in Fig. 5.10. Jets have in average ~ 11 particles, ~ 7 of which are charged tracks.

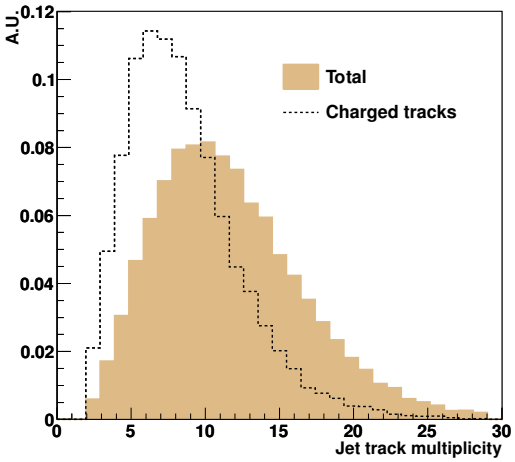

Figure 5.10: Total and charged track multiplicity of jets as obtained in MC10 inclusive $b\bar{b}$ sample.

MC10 $b\bar{b}$, $c\bar{c}$ and *minimum bias* samples are used in Fig. 5.11 to compare the invariant mass and the transverse momentum of b-, c- and light jets, where the latter are defined in not entirely appropriate way as jets with no seed tracks associated to b nor c. As expected, jets from c quark fragmentation have slightly softer p_{T} and lower mean invariant mass with respect to b-jets. However, it is not surprising that light-quark and gluon jets thus defined have comparable mass and p_{T}: the application of the seeded algorithm produces sensible results if applied to the search for c-jets, also characterized by a displaced SV, while the absence of this assumption in the case of light jets leads to inconsistencies. Infrared-safe algorithms such as anti-k_t [67] are better suited to study jets from light quarks and gluons.

The separation of the four-momenta of two jets in the $\phi - \eta$ space is shown in Fig. 5.12. The two components due to jet pairs originating from the same or from different B hadrons is highlighted. Jet pairs for which $\Delta R < 2R_{\mathrm{c}}$ have spatial overlapping.

5.4.1.1 Jet overlapping

It is interesting to inspect the jet overlapping in terms of shared energy. Let us define $E_{i\cap j}$ the energy component of $\mathbf{p}_{i\cap j}$, the four-momentum sum of all particles simultaneously assigned to jet i and j, whose energy is E_i and E_j respectively, each particle being counted once. Shared energy fraction $F_{E\mathrm{shared},ij}$

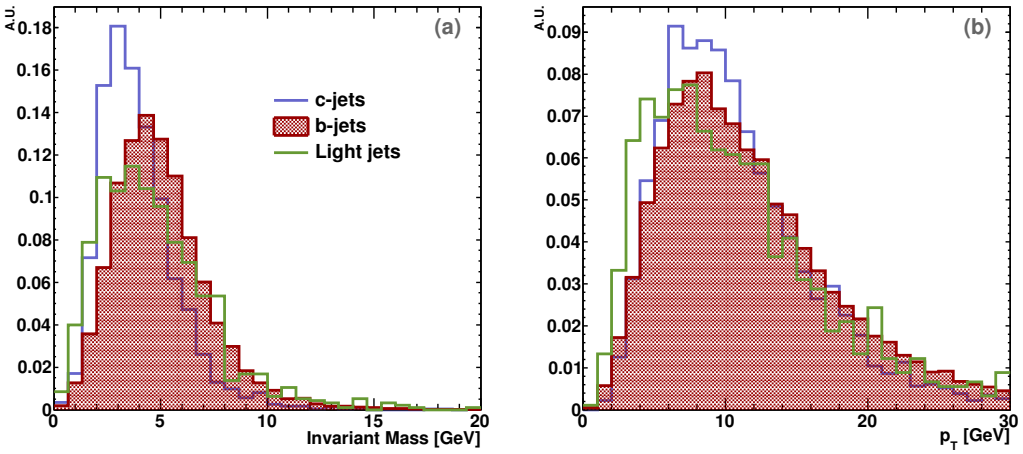

Figure 5.11: Invariant mass (a) and transverse momentum (b) of b-, c- and light jets. Distributions are normalised to the same area.

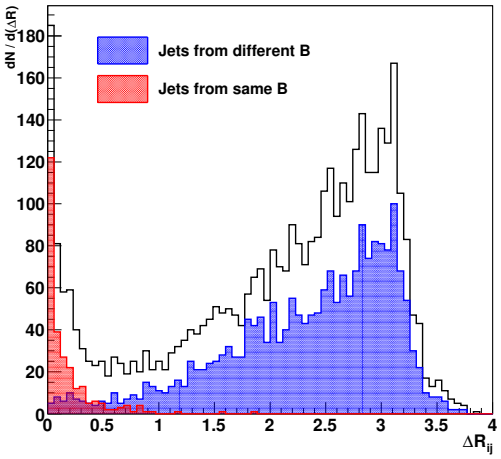

Figure 5.12: ΔR between two jets. Jet pairs originating from different (same) B hadrons are shown in blue (red). The black line is the total distribution.

is then defined as:

$$F_{E\text{shared},ij} = \frac{E_{i\cap j}}{E_i + E_j} \ . \tag{5.4}$$

Fig. 5.13 shows the distribution of this fraction. The component of jet pairs originating from the same B decay can be taken as a reference to establish the value of $F_{E\text{shared},ij}$ above which jets i and j will be merged into a single jet. Therefore jet merging will be performed if $F_{E\text{shared},ij} > 0.4$. The ΔR distribution of such jets may be seen in Fig. 5.14.

The procedure consists in recursively merging a jet with the jet which shares the maximum energy fraction with it. As for the seed merging, merged jet inherits the seed position from the best seed in terms of DOCA of seed tracks.

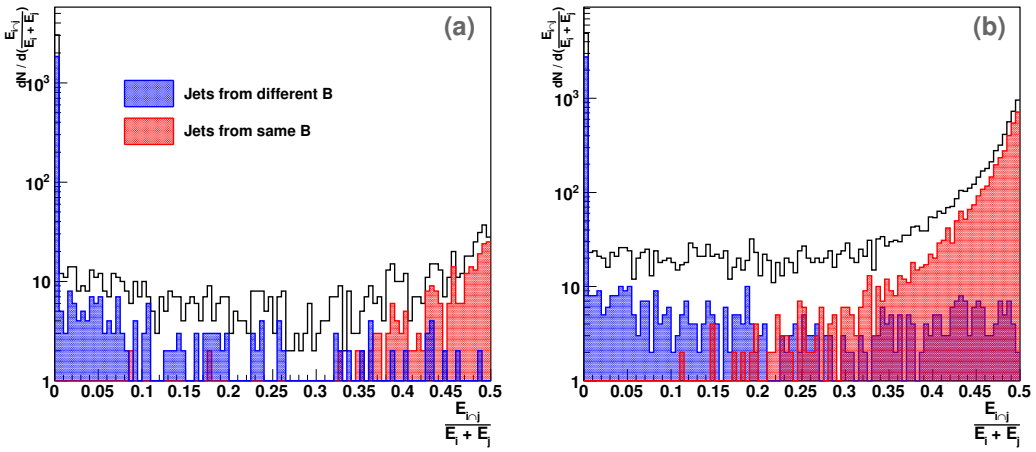

Figure 5.13: Fraction of energy shared between two jets (a). Jet pairs originating from different and same B hadron are shown in blue and red respectively. In (b) distribution is shown excluding seed merging procedure. The black line is the total distribution.

The last step of the jet reconstruction procedure is the splitting: tracks shared by two jets for which $F_{E\text{shared},ij} < 0.4$ are univocally assigned to the closer jet in ΔR. Fig. 5.15 shows the final ΔR distribution between two jets after jet merging and splitting procedure.

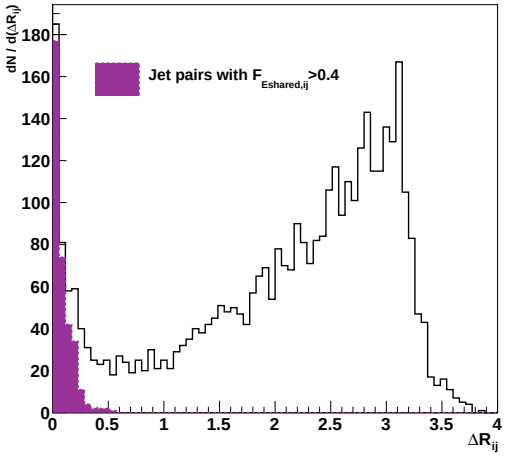

Figure 5.14: ΔR between two jets for which $F_{E\text{shared},ij} > 0.4$. The black line is the total distribution.

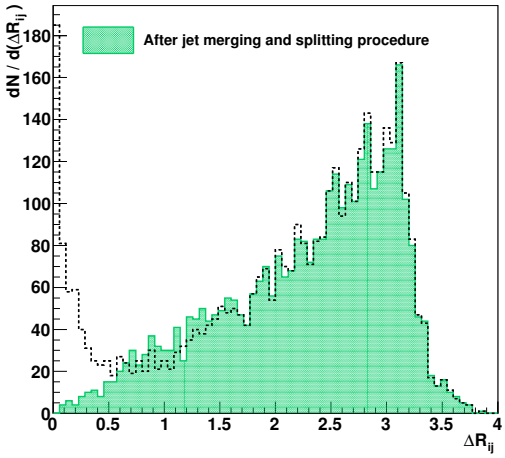

Figure 5.15: ΔR between two jets after jet merging and splitting (green). Initial distribution in dashed line.

5.5 Trigger and Stripping efficiencies

5.5.1 Trigger efficiency

LHCb trigger consists of hardware and software levels, aimed at reducing the 40 MHz collision rate down to 2 kHz — the final trigger output bandwidth. Hardware based L0 trigger [51] relies on selecting highest p_{T} hadron, electron and photon clusters in the calorimeters as well as muon candidates in the muon chambers. Software based High Level Trigger has two consecutive trigger steps, *i.e.* HLT1 that is based mostly on the track p_{T} and impact parameter as it is expected for B decay products, HLT2 which makes use of more exclusive selections.

Since the event production rate in LHCb has been continually increasing since the LHC start up, the configuration of the LHCb trigger system had to be adjusted several times in order to get an optimal physics yield keeping output bandwidth at its nominal value. The LHCb trigger is configured via a unique key, the so-called Trigger Configuration Key (TCK) [73], being a 32-bit word which defines sequence of algorithms and cuts for both L0 and HLT triggers. Lower 16 bits specify the L0 configuration, while upper 16 bits indicate corresponding HLT configuration, the so-called HltType.

Two signal samples containing the events with at least one reconstructed seed (*one-seed signal*) and with at least two seeds in the event (*two-seed signal*) have been obtained from ∼6M $b\bar{b}$-inclusive events of MC10 simulation, where the corresponding TCK has been flagged. A common requirement in both samples is the presence of exactly one reconstructed PV.

The efficiency to reconstruct at least one or two seeds out of a sample of one PV events has been evaluated from MC10 $b\bar{b}$ inclusive events and has been found to be

$$\epsilon_{1\mathrm{seed}} = (18.07 \pm 0.03)\% \tag{5.5}$$

$$\epsilon_{2\mathrm{seed}} = (3.00 \pm 0.01)\% \ . \tag{5.6}$$

Since MC10 simulation has been performed employing TCK=0x2E002A, the appropriate L0, HLT1 and HLT2 trigger lines have been tested in order to get the highest efficiency. The most efficient L0 lines for one- and two-seed signal samples prove to be `L0Hadron` and `L0Muon` lines. Their efficiency is listed in Tab. 5.4. These two lines combined account for the 89.8% of one-seed signal events accepted by the whole L0 trigger for physics analyses `L0Physics` (91% of accepted two-seed signal events).

L0 Trigger Line	Efficiency(%)
one-seed signal sample	
`L0Hadron`	18.0 ± 0.1
`L0Muon`	12.7 ± 0.1
Total	28.2 ± 0.1
two-seed signal sample	
`L0Hadron`	28.7 ± 0.2
`L0Muon`	15.2 ± 0.2
Total	39.2 ± 0.2

Table 5.4: L0 trigger efficiencies for given lines for one- and two-seed signal samples. L0 efficiencies are defined with respect to the number of sample events.

Events accepted by one of this two L0 lines are then requested to have positive decision for one of the `Hlt1Track*` lines of HLT1 trigger. This requirement guarantees to accept 88.9% (94%) of one-seed (two-seed) signal events accepted by `HLT1Physics` lines. Efficiencies are shown in Tab. 5.5.

The HLT2 topological lines [74] has been chosen for selecting the events at the HLT2 stage. They are designed to trigger inclusively on n-body ($n = 2, 3, 4$) B decays with at least 2 charged daughters. Tab. 5.6 summarizes the efficiency of `Hlt2Topo*` lines. They turn out to account for the 60.7% (69.4%) of one-seed (two-seed) signal events accepted by `HLT2Physics`.

The overall trigger efficiency for one-seed and two-seed signal samples have been found to be:

$$\epsilon_{\text{trigger}}^{\text{1seed}} = (4.09 \pm 0.04)\% \tag{5.7}$$

$$\epsilon_{\text{trigger}}^{\text{2seeds}} = (11.3 \pm 0.2)\% \ . \tag{5.8}$$

The TisTos tool [75] has been used elsewhere [71] to check the fractions of events triggered on signal (TOS), triggered independently from signal (TIS) and triggered on both (TOB). The TOB fraction is sensitive to potential ambiguities in the trigger decision but it has been found to be negligible in any case. The TisTos mechanism could not be used straight away in our analysis, since the $b\bar{b}$ cross section measurement is aimed to be inclusive by definition, and the TisTos algorithm is especially suited for exclusive selections. Only cross-checks, as shown in [71], could be done with a partial signal sub-sample, that corresponds to an exclusive selection.

HLT1 Trigger Line	Efficiency(%)
one-seed signal sample	
`Hlt1TrackMuon`	19.3 ± 0.2
`Hlt1TrackAllL0`	41.0 ± 0.2
`Hlt1TrackPhoton`	3.1 ± 0.1
Total	48.6 ± 0.2
two-seed signal sample	
`Hlt1TrackMuon`	18.6 ± 0.3
`Hlt1TrackAllL0`	56.4 ± 0.4
`Hlt1TrackPhoton`	4.9 ± 0.2
Total	62.3 ± 0.4

Table 5.5: HLT1 trigger efficiencies for `Hlt1Track*` lines for one- and two-seed signal samples. HLT1 efficiencies are defined with respect to the number of events after L0.

HLT2 Trigger Line	Efficiency(%)
one-seed signal sample	
`Hlt2TopoOSTF2Body`	12.6 ± 0.2
`Hlt2TopoOSTF3Body`	20.5 ± 0.2
`Hlt2TopoOSTF4Body`	14.3 ± 0.2
Total	29.8 ± 0.3
two-seed signal sample	
`Hlt2TopoOSTF2Body`	15.9 ± 0.4
`Hlt2TopoOSTF3Body`	32.5 ± 0.5
`Hlt2TopoOSTF4Body`	32.4 ± 0.5
Total	46.4 ± 0.5

Table 5.6: HLT2 trigger efficiencies for `Hlt2Topo*` lines for one- and two-seed signal samples. HLT2 efficiencies are defined with respect to the number of events after HLT1.

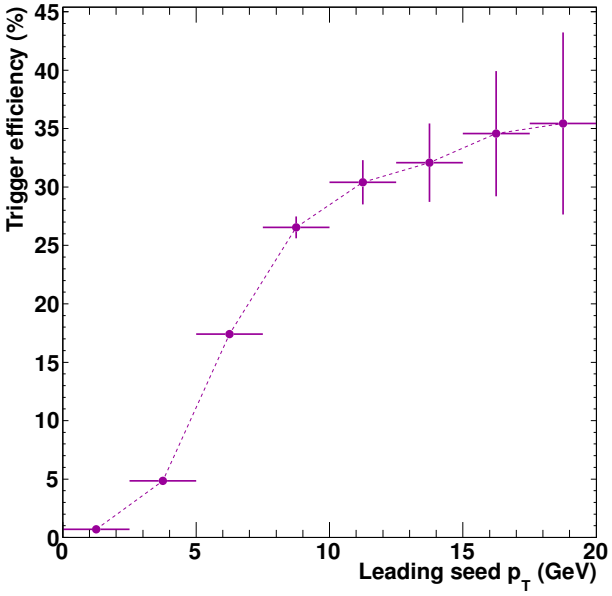

Figure 5.16: Trigger efficiency as a function of the leading seed p_{T}.

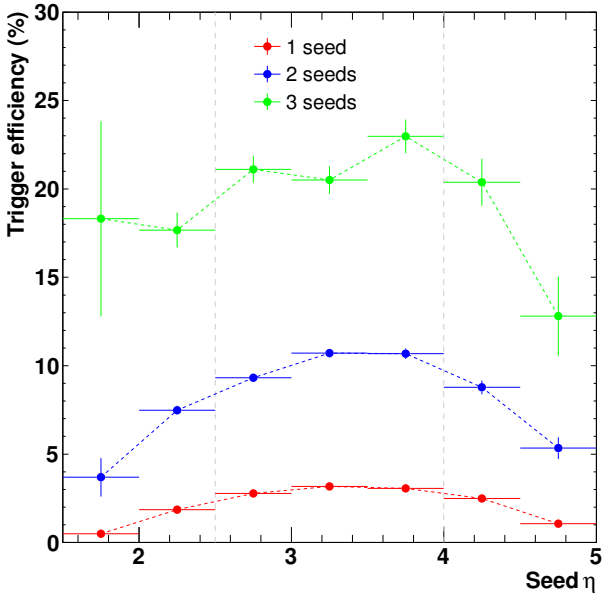

Figure 5.17: Trigger efficiency as a function of η of the seed for events with exactly 1, 2, 3 seeds.

Overall trigger efficiency as a function of the leading seed p_{T} is shown in Fig. 5.16.

A fiducial region definition is needed in order to avoid partial jet reconstruction due to the finite acceptance of the detector, making sure that the reconstructed events are maximally contained in the detector, and therefore the $b\bar{b}$ cross section will be calculated within this volume. It can be defined in terms of the p_{T} and η of the seed or of the jet. Before defining a proper p_{T} region, it is mandatory to correct the energy of the seed or of the jet. This is discussed in Sec. 5.6.

Fig. 5.17 illustrates the dependence of the trigger efficiency on the seed η for events with exactly 1, 2, 3 seeds. The efficiency proves to be quite stable in the range $\eta \in [2.5, 4.0]$, thus the measurent will be restricted to this seed η interval.

5.5.2 Stripping efficiency

Since there is no dedicated stripping selection for b-jet analyses and after considering that $\sim 80\%$ of one- and two-seed signal events accepted by the stripping lines from the B hadron stream are stripped by `B2DX*` lines, this particular group of stripping lines has been chosen to determine the stripping efficiency. They are listed in Tab. 5.7 along with their prescaling, a factor that has a direct influence in the rate of accepted events of each line (See the Appendix for more details). `B2DX*` lines with prescale factor different than 1.0 has been also excluded for the sake of ease of systematic error evaluation. This choice causes a further 14% (18%) of loss in the stripping efficiency for one-seed (two-seed) signal.

Stripping efficiencies with a such defined set of stripping lines for one- and two-seed signal samples after overall trigger are as follows:

$$\epsilon^{\mathrm{1seed}}_{\mathrm{stripping}} = (9.3 \pm 0.3)\% \tag{5.9}$$

$$\epsilon^{\mathrm{2seeds}}_{\mathrm{stripping}} = (10.6 \pm 0.5)\% \; . \tag{5.10}$$

5.6 Jet Energy Correction

Before any comparison can be made between MC and data and in order to define a fiducial cut on the p_{T} of the jets, an energy correction need to be made to account for energy loss due to undetected particles or wrong energy measurement and tracking.

BHadron Stripping line	Prescale factor
B2DXWithD2KPiPi0Merged	1.0
B2DXWithD2KPiPi0Resolved	1.0
B2DXWithD2Kshh	1.0
B2DXWithD2hhLine	1.0
B2DXWithD2hhWS	0.1
B2DXWithD2hhh	1.0
B2DXWithD2hhhWS	0.1
B2DXWithD2hhhh	1.0
B2DXWithLambda	1.0
B2DXWithUnbiasedB2DPi	0.1

Table 5.7: B2DX* lines of BHadron stripping and their prescale factor.

The idea is to calibrate the energy of the jets using generator level jets, already presented in Fig. 5.9. Here cone jets are built using detectable generated particles taking the B line of flight as direction of the cone. Fig. 5.18 shows the energy, momentum and p_{T} of these jets and of the corresponding B hadron. Since the trigger and stripping selections significantly distort the distributions of the selected B hadrons, the calibration has been performed directly comparing reconstructed signal jets to the MC *true* jet built around the corresponding B.

The ratio of the energy of true jets and the energy of reconstructed jets ($E_{\mathrm{jet}}^{\mathrm{true}}/E_{\mathrm{jet}}$) has been fitted in the overall jet energy range using the formula:

$$f_{corr}(E_{\mathrm{jet}}) = p_0 + \frac{p_1}{E_{\mathrm{jet}} + p_2} \ , \tag{5.11}$$

where p_i ($i = 1, 2, 3$) are free parameters. Results of the fit inside the fiducial η range are shown in Fig. 5.19 for two different values of R_{c}. Events after trigger and stripping have been used to obtain the parameters of the fitting function.

The jet energy has been then corrected applying the formula

$$E_{\mathrm{jet}}^{\mathrm{corr}} = E_{\mathrm{jet}} \cdot f_{\mathrm{corr}}(E_{\mathrm{jet}}) \ . \tag{5.12}$$

The result of the correction applied to reconstructed jets is shown in Fig. 5.20.

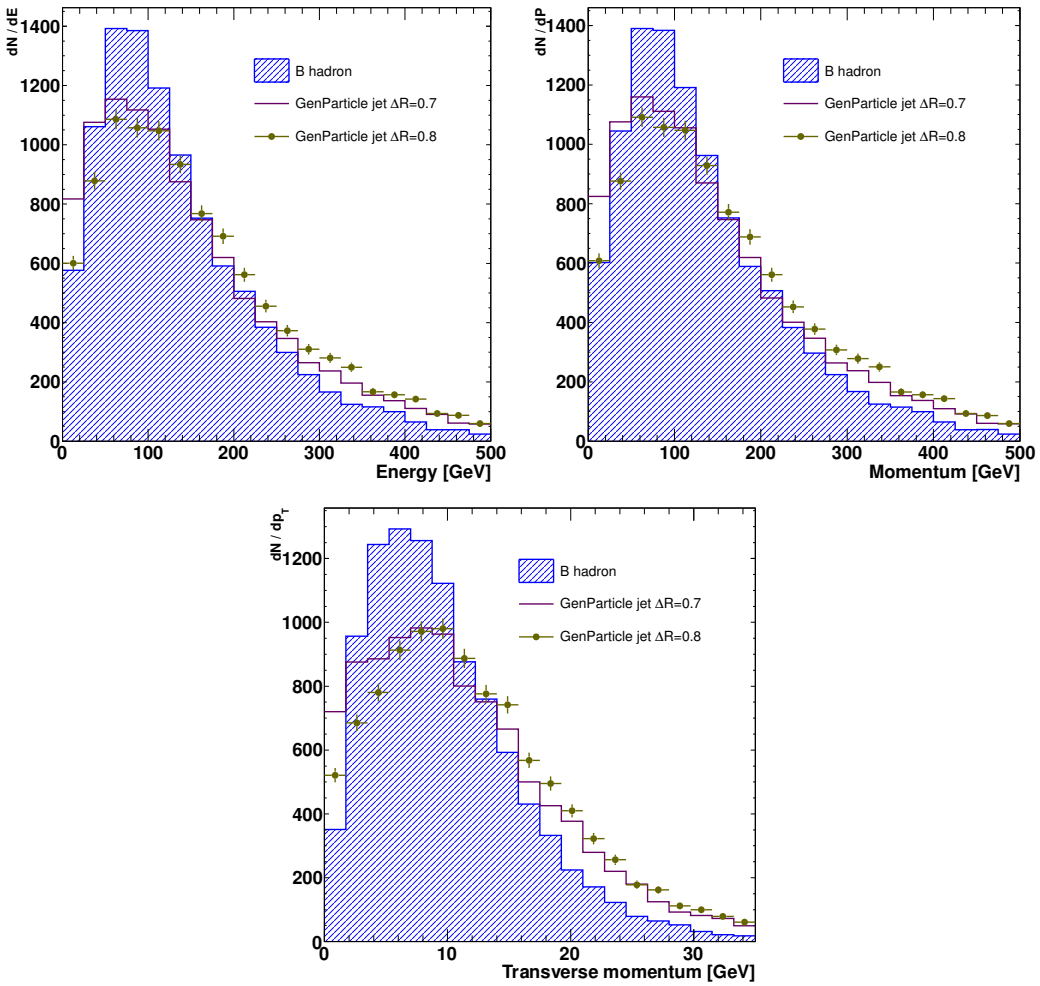

Figure 5.18: Energy, momentum and p_{T} of cone jets built around B flight direction with visible generated particles with different values of radius R_{c}. Correlated B hadron is also shown for comparison. B hadrons shown are associated to a reconstructed signal seed in events after the trigger. Event generator is Pythia 6.4.

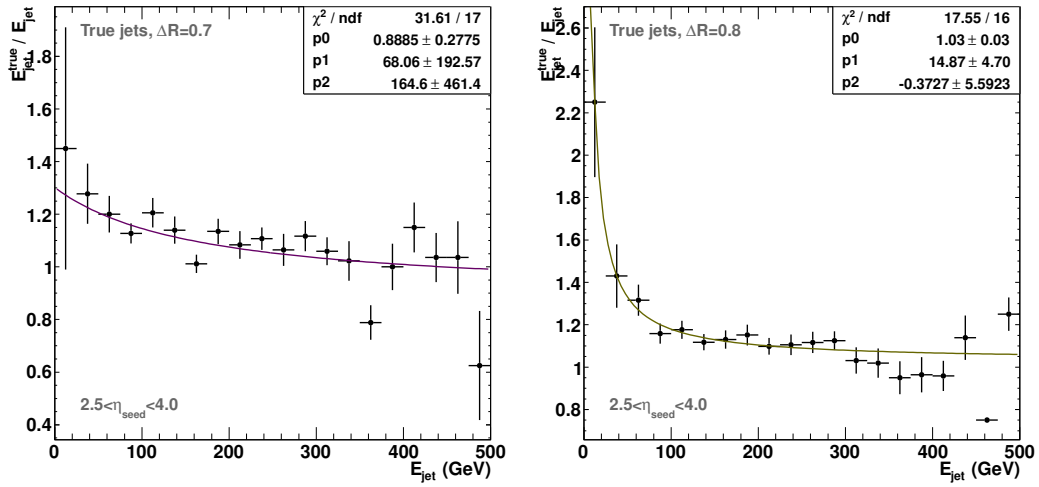

Figure 5.19: Results of the fit to $E_{\mathrm{jet}}^{\mathrm{true}}/E_{\mathrm{jet}}$ in the η fiducial range of the measurement with $R_{\mathrm{c}} = 0.7, 0.8$.

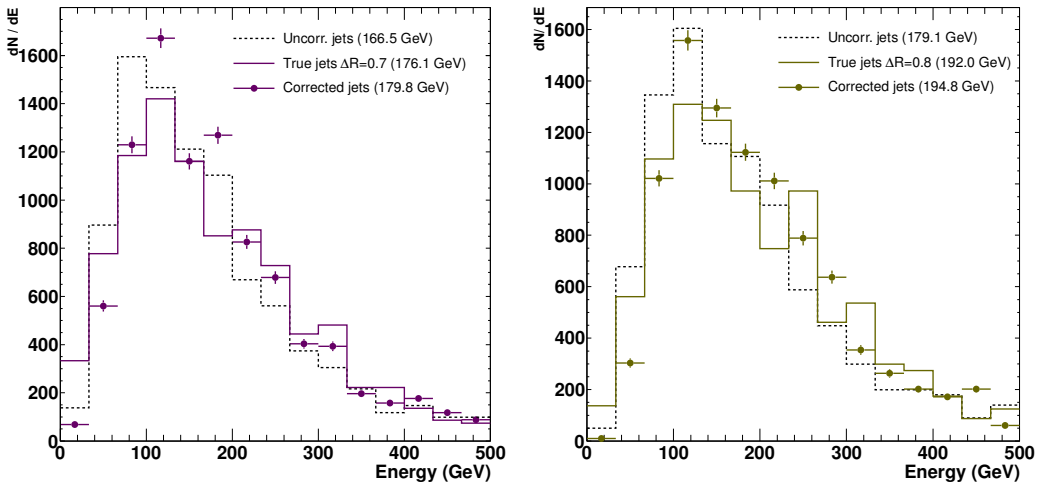

Figure 5.20: Energy of jets after the correction (coloured figures). Uncorrected jet (dashed line) and true jet energy (coloured line) distributions are also shown. In parentheses the mean value of each distribution. Left plot for jet with $R_{\mathrm{c}} = 0.7$, right plot for jets with $R_{\mathrm{c}} = 0.8$.

The momentum of the jet has been corrected using the calibrated seed energy:

$$p_{\text{jet}}^{\text{corr}} = \sqrt{(E_{\text{jet}}^{\text{corr}})^2 - M_B^2} \ , \tag{5.13}$$

where M_B is the mass of the B^0 meson. Finally, jet p_{T} has been calibrated with respect to the corrected jet momentum:

$$p_{T,\text{jet}}^{\text{corr}} = p_{\text{jet}}^{\text{corr}} \cdot \sin\theta \ , \tag{5.14}$$

where θ is the angle between the seed direction and the beam axis. Corrected jet p_{T} is shown in Fig. 5.21.

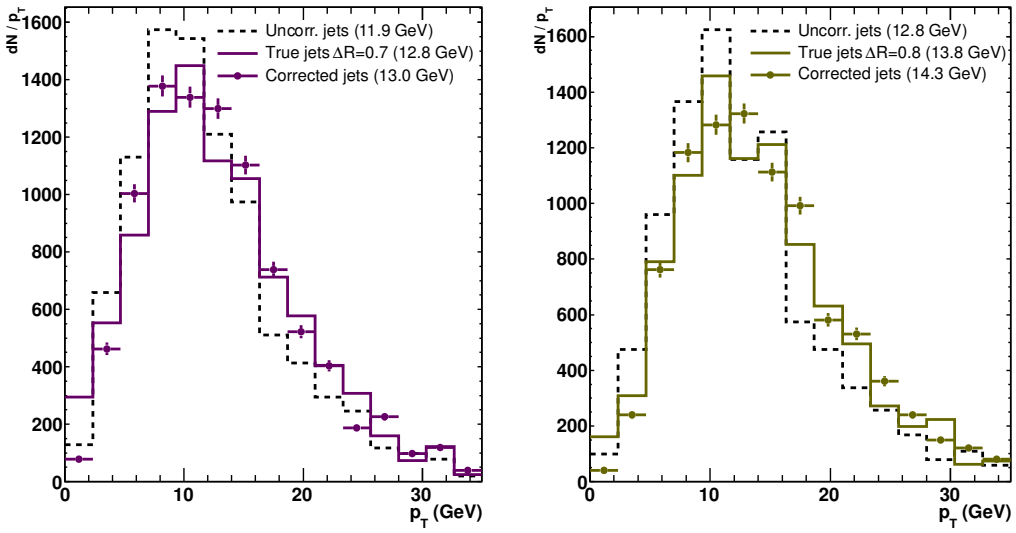

Figure 5.21: Transverse momentum of calibrated jets (coloured figures). Uncorrected jet (dashed line) and true jet energy (coloured line) distributions are also shown. In parentheses the mean value of each distribution.

The resolution $\frac{E_{\text{jet}}^{\text{corr}} - E_{\text{jet}}^{\text{true}}}{E_{\text{jet}}^{\text{true}}}$ of the jet energy after correction has been fitted with a Gaussian and the result is shown in Fig. 5.22. The energy resolution for $R_{\text{c}} = 0.7$ and $R_{\text{c}} = 0.8$ turns out to be $\sigma_{0.7} = 0.204 \pm 0.008$ and $\sigma_{0.8} = 0.196 \pm 0.008$ respectively.

In order to define a fiducial interval for the measurement in transverse momentum of jets, a cut at $p_{T,\text{jet}}^{\text{corr}} = 5\,\text{GeV}$ will be adopted.

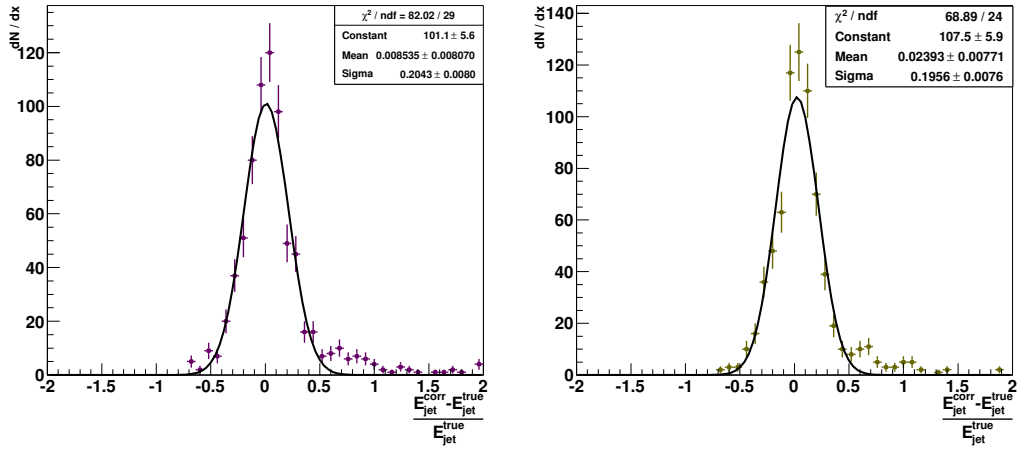

Figure 5.22: Resolution of the jet energy after correction for jets with $R_{\mathrm{c}} = 0.7$ (left) and $R_{\mathrm{c}} = 0.8$ (right).

6 Results

The aim of the analysis is to calculate the inclusive $b\bar{b}$ quark pair production cross section inside the Fiducial Volume (FV) $\eta \in (2.5, 4.0)$ using a formula such as:

$$\sigma_{\mathrm{FV}}^{b\bar{b}} = \frac{N^{\mathrm{obs}} - N^{\mathrm{bkg}}}{\mathcal{L} \times \epsilon^{b\bar{b}}} \ , \tag{6.1}$$

where N^{obs} is the number of event candidates found in real data, N^{bkg} is the sum of charm and light jet contribution estimated from Monte Carlo, $\mathcal{L}$ is the integrated luminosity of data sample and $\epsilon^{b\bar{b}}$ is the total efficiency of selected events calculated making use of MC10 inclusive $b\bar{b}$ simulation. Each of this terms will be detailed in the present chapter, which is also devoted to the systematic error evaluation.

The differential cross section can also be measured as a function of the pseudorapidity η, the di-jet invariant mass and the di-jets $\Delta\phi$ (or ΔR) with the formula:

$$\frac{d\sigma}{dx} = \frac{N_i^{b\bar{b}}}{\mathcal{L} \times \epsilon_i^{b\bar{b}} \times \Delta x} \ , \tag{6.2}$$

where $\mathcal{L}$ is the luminosity of the data set, $N_i^{b\bar{b}}$ is the number of events in the Δx interval width of the variable x studied, and $\epsilon_i^{b\bar{b}}$ the efficiency in the corresponding bin.

6.1 Real Data sample

The data analysed are those collected in 2010 run with collisions at $\sqrt{s} =$ 7 TeV. `Stripping12b` (see Sec. 3.6) data taken with TCK=0x2E002A, 0x2E002C

have been used, since these two trigger configurations have very similar conditions. The corresponding integrated luminosity is $\sim 17.7\,\mathrm{pb}^{-1}$, about $\frac{1}{2}$ of the total luminosity collected in 2010. Fig. 6.1 shows the TCK breakdown of the integrated luminosity collected in 2010. The quoted luminosity comes from an offline analysis procedure, which allows a more precise luminosity estimation [76, 77] than the online measurement performed by the LHC machine.

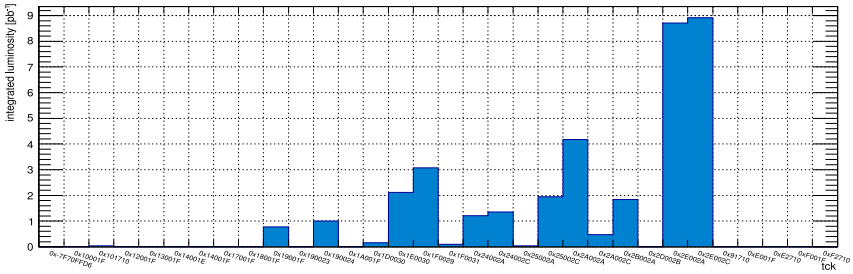

Figure 6.1: Integrated luminosity per TCK in 2010 data taking. TCKs 0x2E002A and 0x2E002C accounts for $\sim 50\%$ of collected luminosity.

Since there is no dedicated stripping selection for b-jet analyses, the extraction of the cross section has been made using real data events selected by a reduced set of stripping lines of the Bhadron stripping stream, the collection of inclusive selection lines which select events with B hadron candidates, as it has been illustrated in Sec. 5.5.2 where the related stripping efficiency has been computed.

Only events with exactly one reconstructed PV have been considered. One PV sample accounts for the $\sim 49\%$ of the whole data sample considered. The effective integrated luminosity resulting from this choice is calculated in the following section.

6.2 Effective Integrated Luminosity

The average number of interactions per bunch crossing, μ, in 2010 data varies run by run. Its evolution in the period considered is shown in Fig. 6.2. Since the analysis considers only bunch crossings with one reconstructed primary vertex, it is necessary to calculate which fraction of luminosity this cut corresponds to.

In order to estimate the effective integrated luminosity, one has to consider that in a run r, with an average number of interactions per bunch crossing μ_r,

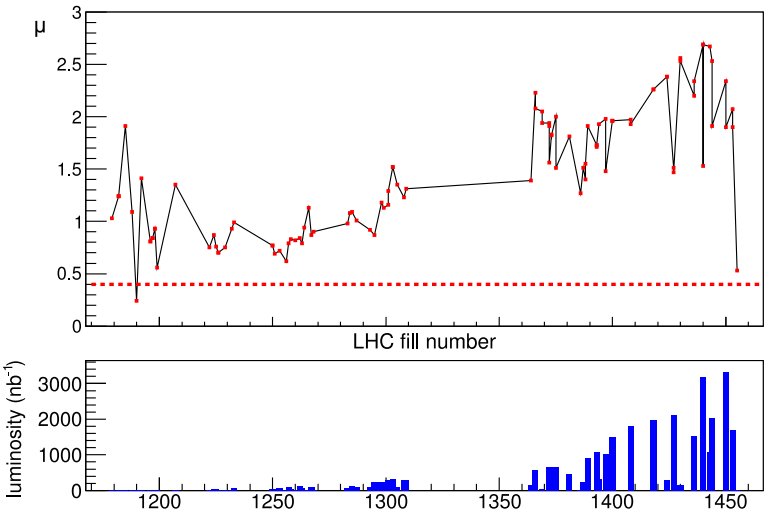

Figure 6.2: Evolution of μ per fill in 2010, compared to the design value (dashed line).

the number N_r of pp interactions is

$$N_r = \mathcal{L}_r \cdot \sigma_{pp} = n_r \cdot \mu_r \ , \tag{6.3}$$

where $\mathcal{L}_r$ is the integrated luminosity of the run, σ_{pp} the pp cross section and n_r the number of proton bunch crossings in the run. The total number of pp vertices is the sum of the number of pp interactions seen in each bunch crossing, this last number being distributed as a poisson of parameter μ_r. Selecting the bunch crossings with one PV one should be able to measure the same σ_{pp}, thus the number of bunch crossings with exactly one PV in the run r is

$$N_{1\mathrm{PV},r} = \mathcal{L}_{\mathrm{eff},r} \cdot \sigma_{pp} = n_r \cdot \mathcal{P}(1, \mu_r) \ , \tag{6.4}$$

where $\mathcal{L}_{\mathrm{eff},r}$ is the effective luminosity corresponding to the one PV sample, $\mathcal{P}(1, \mu_r)$ is the probability to obtain 1 from a poisson distribution whose characteristic parameter is μ_r. Dividing this equation by Eq. 6.3 one obtains the effective integrated luminosity of the run as a function of μ_r:

$$\mathcal{L}_{\mathrm{eff},r} = \mathcal{L}_r \cdot \frac{\mathcal{P}(1, \mu_r)}{\mu_r} \ . \tag{6.5}$$

The total effective luminosity can be obtained calculating $\mathcal{L}_{\mathrm{eff}} = \sum_r \mathcal{L}_{\mathrm{eff},r}$ over all considered runs. In order to put in a more explicit way the fraction of

luminosity that corresponds to the one PV cut, an average efficiency can be calculated averaging over all runs:

$$\epsilon_{1\mathrm{PV}} = \frac{\sum_r \mathcal{L}_{\mathrm{eff},r}}{\sum_r \mathcal{L}_r} \ . \tag{6.6}$$

Therefore, the total effective luminosity can be expressed as

$$\mathcal{L}_{\mathrm{eff}} = \epsilon_{1\mathrm{PV}} \cdot \mathcal{L} \ , \tag{6.7}$$

with $\mathcal{L} = \sum_r \mathcal{L}_r$.

Integrated and effective integrated luminosity for each TCK are reported in Tab. 6.1. The luminosity calculation has been performed using data from `MBNoBias` line of `MiniBias` stripping stream, in order to avoid any possible bias from the trigger. These values has been used for the measurement of $\sigma_{b\bar{b}}$.

	$\mathcal{L}$ (pb^{-1})	$\mathcal{L}_{\mathrm{eff}}$ (pb^{-1})	$\epsilon_{1\mathrm{PV}}$
0x2E002A	9.3 ± 0.3	1.59 ± 0.06	0.17 ± 0.01
0x2E002C	8.4 ± 0.3	1.06 ± 0.04	0.13 ± 0.01
Total	17.7 ± 0.6	2.65 ± 0.09	0.15 ± 0.02

Table 6.1: Integrated luminosity and effective integrated luminosity for the two TCK considered. The efficiency $\epsilon_{1\mathrm{PV}}$ is defined by Eq. 6.7.

6.3 Global Event Cuts

Effects of Global Event Cuts, implemented as conditions in the Level 0 trigger, have been studied for the two L0 lines considered in the analysis. These conditions are summarized in Tab. 6.2.

Global event cuts are applied on:

- highest E_{T} of L0 hadron clusters, required by the `L0Hadron` line;
- p_{T} of L0 highest-p_{T} muon candidate (Muon1), required by the `L0Muon` line;
- SPD hit multiplicity, required by both lines.

Condition	0x2E002A	0x2E002C
`L0Hadron`		
SPD hits	< 900	< 450
Hadron E_{T} (*ADC counts*)	> 180	> 180
`L0Muon`		
SPD hits	< 900	< 900
Muon1 p_{T} (*ADC counts*)	> 35	> 35

Table 6.2: Conditions of `L0Hadron` and `L0Muon` lines for the two TCKs considered.

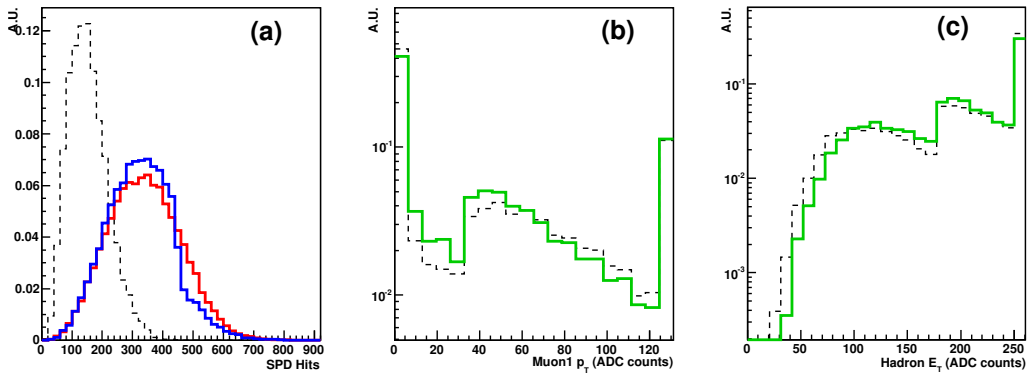

Figure 6.3: Distribution of Global Event Variables for MC $b\bar{b}$-inclusive (dashed line) and Bhadron data, for events accepted by `L0Hadron` or `L0Muon` lines. (a): SPD multiplicity, 0x2E002A data in red, 0x2E002C data in blue. (b): Muon1 p_{T}, data in green (c): Hadron E_{T}, data in green. Distribution are normalized to the same area.

The distribution of this variables for data and MC is shown in Fig. 6.3.

Hadron E_{T} and Muon1 p_{T} are well reproduced by MC and their effects have been studied comparing efficiencies in data to the MC prediction. The evaluation of possible biases introduced by the hadron E_{T} cut in the `L0Hadron` line has been performed using events after full selection, *i.e.* including trigger and stripping. `L0Muon` line accepts events regardless of the hadron cluster E_{T}. Let $N_{\texttt{L0Muon}}$ be the subsample with positive `L0Muon` decision, for which the E_{T} distribution turns out to be unaffected. The following fraction can then be

computed, both for data and MC:

$$\epsilon = \frac{N_{\texttt{L0Muon\&\&L0Hadron}}}{N_{\texttt{L0Muon}}} \ . \tag{6.8}$$

An analogue procedure has been applied to check the Muon1 p_{T} cut.

In both cases the fraction calculated for MC is well compatible with the one calculated with data, thus possible discrepancies between MC and data can be considered negligible.

MC cannot be used to study the impact of the cut on SPD multiplicity, since it is badly reproduced by MC. The study however can be performed using data itself: SPD hit multiplicity in TCK 0x2E002A is not affected by the cut at 900 hits implemented in both L0 lines as can be seen in Fig. 6.3a, thus this sample can be used to evaluate efficiency of the cut at 450 hits implemented in the Hadron line of TCK 0x2E002C. An average SPD cut efficiency has been evaluated and will enter directly in the cross section calculation to account for the event loss due to the cut. This efficiency is found to be:

$$\epsilon_{\mathrm{SPD}} = (95.22 \pm 0.06)\% \tag{6.9}$$

and it is meant to be applied to 0x2E002C sample only, while for 0x2E002A sample $\epsilon_{\mathrm{SPD}} = 1$ is implicitly assumed.

Such a correction may introduce an additional systematic error: it will be addressed in Sec. 6.7 .

6.4 Final selection

The whole selection applied to both data and MC samples can be summarised in the following consecutive steps:

1. *One PV selection*: events are kept if exactly one primary vertex has been reconstructed. This choice allows to avoid the difficulties originating from the ambiguous assignment of a track to one PV in the case multiple interactions. The accuracy of the measurement of variables such as the track impact parameter, which are crucial to identify B hadron decays, largely benefits from this choice;

2. *Seed reconstruction*: the seeding procedure is performed as illustrated in Sec. 5.3, long tracks are used to build two-track secondary vertices. Secondary vertices and their tracks are required to fulfil kinematic, topo-

logical and fit quality requirements. Events are dropped if no SV is reconstructed;

3. *Trigger and stripping*: a selection of trigger and stripping lines has been done pursuing the objective of keeping the inclusive trait of the analysis. Events are requested to be accepted by at least one line at any level of trigger and stripping. Details are exposed in Sec. 5.5; [1]

4. *Jet reconstruction*: further charged and neutral tracks are added to the seed if they fit in a cone with radius R_c. Such jets are merged according to an invariant mass criterium or splitted if they share an amount of energy beyond a certain threshold. Their energy is finally corrected using MC information. The jet reconstruction modifies the final efficiencies varying the number of jets of each events. This topic is covered in Sec. 5.4;

5. *Fiducial cuts*: jets are further required to lie in a fiducial volume defined in term of η of the seed position and p_T of the jet. In the pseudorapidity interval $\eta \in (2.5, 4.0)$, central in the η LHCb acceptance, the algorithm displays a reasonably stable trigger efficiency. This choice also avoid partial jet reconstruction due to the finite acceptance of the detector. A jet tranverse momentum cut at 5 GeV has been adopted to remove inefficiently reconstructed jets and to avoid the *infrared* inconsistency that a cone-like jet algorithm (as the one applied in the analysis) might have when used to reconstruct light-quark jets, which is not the case for b-quark jets.

6. Events with exactly two reconstructed jets are considered.

The efficiency of the one PV cut has been only considered to rescale the integrated luminosity of data accordingly. The total efficiencies for signal and background has been then calculated with respect to the number of events with one PV.

6.4.1 Total selection efficiency $\epsilon_{\rm FV}^{b\bar{b}}$

The total efficiency of selecting events in which a $b\bar{b}$ pair has been produced inside the FV can be expressed as a product of efficiencies:

$$\epsilon_{\rm FV}^{b\bar{b}} = \epsilon_{\rm 1seed} \cdot \epsilon_{\rm trigger} \cdot \epsilon_{\rm stripping} \cdot \epsilon_{\rm sel} \ , \tag{6.10}$$

[1] It is worth recalling that data are required to be accepted by the physical triggers and by at least one line of the proper stripping stream in order to be recorded. Here we refer to the trigger and stripping lines adopted for the analysis.

where the values of ϵ_{1seed}, $\epsilon_{\text{trigger}}$ and $\epsilon_{\text{stripping}}$ are given in Eq. 5.5, 5.7 and 5.9 respectively. The selection efficiency ϵ_{sel} accounts for the items 4 to 6 of the list given in the previous section.

In order to estimate $\epsilon_{\text{FV}}^{b\bar{b}}$, the MC10 $b\bar{b}$-inclusive sample have been used. A number of events $N_{\text{sel}}^{b\bar{b}}$ has been fully selected. Events with jets from combinatorial background have been further removed from this sample and each event has been checked to contain two jets each one originating from a b quark. Defining such pure sample as $N_{\text{true}}^{b\bar{b}}$, the purity of the selected sample is

$$p = \frac{N_{\text{true}}^{b\bar{b}}}{N_{\text{sel}}^{b\bar{b}}} = 0.58 \pm 0.04 \ . \tag{6.11}$$

The total efficiency of selecting such *pure* $b\bar{b}$ sample can be written as

$$\epsilon_{\text{FV}}^{b\bar{b}} = \frac{N_{\text{true}}^{b\bar{b}}}{N_{\text{1PV}}^{b\bar{b}} \cdot \epsilon_{\text{FV}}} \ , \tag{6.12}$$

where $N_{\text{1PV}}^{b\bar{b}}$ is the number of events with one PV in the MC sample and ϵ_{FV} is the fraction of events with two b quarks produced inside the FV out of $N_{\text{1PV}}^{b\bar{b}}$. Considering a factor $\epsilon_{\text{FV}} = 0.532$ established with the generator PYTHIA, $\epsilon_{\text{FV}}^{b\bar{b}}$ turns out to be

$$\epsilon_{\text{FV}}^{b\bar{b}} = (1.04 \pm 0.12) \times 10^{-4} \ . \tag{6.13}$$

6.5 Composition of selected data sample

The composition of the selected data sample in terms of b, c, light and combinatorial content can be determined directly from Monte Carlo. It is also possible to fit the total distribution of some variable for a sample of data to extract the relative fractions, where the individual distribution shapes are taken from Monte Carlo. The distributions taken from Monte Carlo are referred to as templates hereafter.

As it will be evident, the limited MC statistics available prevented a reliable description of data through templates. Fig. 6.4 shows an example of what could be done with the template fit of data. MC samples used in Fig. 6.4 are part of a selection that does not include the trigger filter to fit a distribution of fully selected data. This choice allows to have more MC statistics to perform the extraction of the relative fractions, nevertheless the trigger would bias significantly the shape of the variable thus affecting the validity of the template

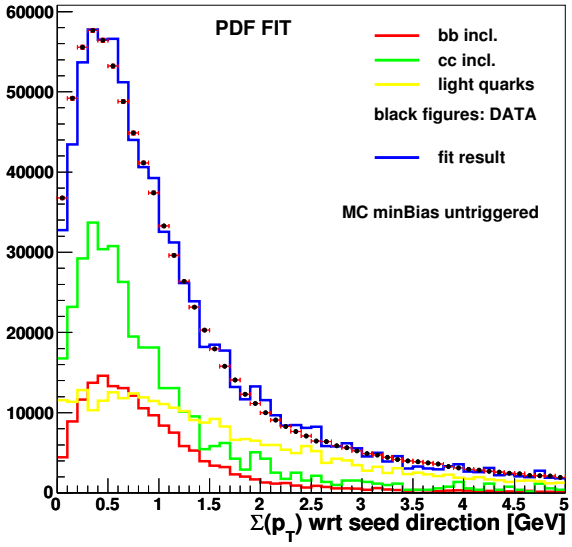

Figure 6.4: Example of variable fitted with shapes extracted from MC samples. The variable shown is the sum of seed tracks transverse momenta with respect to the seed direction, using a three-track seeding approach. The selection of MC events does not include the trigger. The bias that the trigger would introduce actually prevents to apply this template fit to fully selected data. Courtesy of M. Kucharczyk.

fit.

The approach followed is therefore to estimate the number of expected events for each background species in an integrated luminosity corresponding to the one of data, by means of selection efficiencies established with MC simulations.

6.5.1 Background expectation

The total selection efficiency for each background type have been calculated similarly to what done for $\epsilon_{\mathrm{FV}}^{b\bar{b}}$. Then the efficiencies are used to estimate the expected number of background events selected in an integrated luminosity $\mathcal{L}_{\mathrm{eff}}$ making use of the appropriate cross sections.

The MC10 $c\bar{c}$-inclusive sample has been used to estimate the total selection efficiency $\epsilon^{c\bar{c}}$. The number of events with one PV in this sample is $N_{1\mathrm{PV}}^{c\bar{c}} \sim 1.29 \times 10^6$. The number of $c\bar{c}$ events expected inside the FV is calculated with

the formula

$$N^{c\bar{c}}_{\text{exp}} = \mathcal{L}_{\text{eff}} \cdot \sigma^{c\bar{c}} \cdot \epsilon^{c\bar{c}}_{\text{gen}} \cdot \epsilon^{c\bar{c}} \ , \tag{6.14}$$

where $\mathcal{L}_{\text{eff}} = 2.65\,\text{pb}^{-1}$ is the effective luminosity of data sample, calculated in Sec. 6.2, $\sigma^{c\bar{c}}$ is the $c\bar{c}$ production cross section in full phase space measured by the LHCb experiment in 2010 [78] and found to be

$$\sigma^{c\bar{c}} = 6100 \pm 934\,\mu\text{b} \ , \tag{6.15}$$

where the total uncertainty is quoted, $\epsilon^{c\bar{c}}_{\text{gen}} = 0.456$ is the efficiency of the acceptance cut implemented in the Pythia generator to simulate $c\bar{c}$ events inside the LHCb detector.

After full selection, a number $N^{c\bar{c}}_{\text{sel}} = 5$ of $c\bar{c}$ events is left. The total efficiency $\epsilon^{c\bar{c}}$ is then found to be

$$\epsilon^{c\bar{c}} = \frac{N^{c\bar{c}}_{\text{sel}}}{N^{c\bar{c}}_{\text{1PV}}} = (4.6 \pm 0.2) \times 10^{-6} \ . \tag{6.16}$$

The expected number of $c\bar{c}$ events then is

$$N^{c\bar{c}}_{\text{exp}} \approx 34258 \pm 1489 \ . \tag{6.17}$$

To estimate the contribution from light jets, a sample of MC10 minimum bias with $N^{q\bar{q}}_{\text{1PV}} \sim 2.71 \times 10^7$ events with one PV has been used. The expected number of light jet events in the integrated luminosity $\mathcal{L}_{\text{eff}}$ is calculated as

$$N^{q\bar{q}}_{\text{exp}} = \mathcal{L}_{\text{eff}} \times \sigma^{\text{inel}} \times \epsilon^{q\bar{q}} \ , \tag{6.18}$$

where $\sigma^{\text{inel}} = 49.2 \pm 5.0\,\text{mb}$ is the inelastic pp cross section used by the Pythia generator and $\epsilon^{q\bar{q}}$ is the total selection efficiency of light jet events. If $N^{q\bar{q}}_{\text{sel}}$ is the number of light jet selected events, then $\epsilon^{q\bar{q}}$ is

$$\epsilon^{q\bar{q}} = \frac{N^{q\bar{q}}_{\text{sel}}}{N^{q\bar{q}}_{\text{1PV}}} \ . \tag{6.19}$$

After full selection, 9 events are left; 5 of them are $b\bar{b}$ events in which each b quark has been correctly tagged by one jet and have been excluded from the count. Analogously, one more event has been excluded, in which the two jets tagged a $c\bar{c}$ quark pair. Therefore assuming $N^{q\bar{q}}_{\text{sel}} = 3$, the efficiency $\epsilon^{q\bar{q}}$ turns out to be

$$\epsilon^{q\bar{q}} = (1.1 \pm 0.6) \times 10^{-7} \ . \tag{6.20}$$

The expected number of light jet events then is

$$N_{\text{exp}}^{q\bar{q}} \approx 14468 \pm 7837 \ . \tag{6.21}$$

6.6 Cross section calculation

A much larger MC statistics of $c\bar{c}$ and light quarks is necessary than the one available at present to use templates for different variables. This is also a mandatory step in order to be independent from the large uncertainty affecting the $\sigma^{c\bar{c}}$ measurement.

With the adopted strategy and according to how the efficiencies have been defined in the previous sections, the $b\bar{b}$ production cross section inside the FV can be calculated as follows:

$$\sigma_{\text{FV}}^{b\bar{b}} = \frac{(N_{\text{obs}}^{\text{DATA}} - N_{\text{exp}}^{c\bar{c}} - N_{\text{exp}}^{q\bar{q}}) \cdot p}{\mathcal{L}_{\text{eff}} \cdot \epsilon_{\text{FV}}^{b\bar{b}}} \ , \tag{6.22}$$

where $N_{\text{obs}}^{\text{DATA}}$ is the number of data events after full selection.

The number $N_{\text{obs}}^{\text{DATA}}$ is the sum of the observed events in the two TCKs 0x2E002A and 0x2E002C. In Sec. 6.3 a GEC factor has been established to correct the number of observed events in the 0x2E002C data sample. The total number of observed events is reported in Tab. 6.3.

TCK	$\epsilon_{\text{SPD}}^{i}$	Observed events
0x2E002A	1.0	53527
0x2E002C	0.9522	33864
$N_{\text{obs}}^{\text{DATA}}$	–	87391

Table 6.3: Observed events in data samples, after Global Event Cut correction. The correction factor is given for each TCK.

Using $N_{\text{obs}}^{\text{DATA}} = 87391$, the expected number of events for the two background species summarized in Tab. 6.4, the total selection efficiency $\epsilon_{\text{FV}}^{b\bar{b}}$ given in Eq. 6.13, the cross section $\sigma_{\text{FV}}^{b\bar{b}}$ turns out to be:

$$\sigma_{\text{FV}}^{b\bar{b}} = (80.6 \pm 1.2)\,\mu\text{b} \ , \tag{6.23}$$

where the statistical error is indicated.

	$c\bar{c}$	Minimum Bias
Cross section σ^i	$6100 \pm 934\,\mu$b	49.2 ± 5.0 mb
Selection efficiency ϵ^i	$(4.6 \pm 0.2) \times 10^{-6}$	$(1.1 \pm 0.6) \times 10^{-7}$
Number of expected events	34258 ± 1489	14468 ± 7837

Table 6.4: Cross section and efficiencies used to calculate the expected number of events in $2.65\,\text{pb}^{-1}$ luminosity inside the fiducial region.

6.7 Systematic errors

A number of systematic uncertainties have been examined. The revelant sources discussed in this section are:

- integrated luminosity;
- primary vertex reconstruction;
- the cross section $\sigma^{c\bar{c}}$;
- correction for SPD multiplicity cut;
- MC statistics;
- trigger and stripping efficiency;
- track multiplicity;
- tracking efficiency.

Other sources, such as the cuts on Hadron E_{T} and Muon1 p_{T} (Sec. 6.3), have been considered and found to be negligible. Tab. 6.5 summarizes all sources and their contribution to the total systematic error.

Integrated Luminosity

The integrated luminosity enters the $\sigma_{\text{FV}}^{b\bar{b}}$ calculation as a normalisation factor, therefore its uncertainty enters directly the cross section. The relative uncertainty of the luminosity measurement, calculated to be 3.5% [76, 77], is then considered as systematic error.

Source	Uncertainty (%)
Integrated luminosity	3.5
Cross section $\sigma^{c\bar{c}}$	9.0
SPD multiplicity cut	0.6
MC statistics	9.0
Trigger and stripping efficiency	3.0
Track multiplicity	3.6
Tracking efficiency	1.1
Total	14.1

Table 6.5: Sources of systematic errors and their estimated values.

Primary Vertex Reconstruction

The analysis selects bunch crossings with only one reconstructed primary vertex. Due to the primary vertex reconstruction algorithm, there is a very small inefficiency determining a loss of events or classifying a two-PV event into one-PV category (see [69]). This effect has been found to be negligible.

Cross section $\sigma^{c\bar{c}}$

LHCb measured in Ref.[78] the total $c\bar{c}$ cross-section to produce c-flavoured hadrons in the range $0 < p_{\mathrm{T}} < 8\,\mathrm{GeV}$ and $2 < y < 4.5$ and quoted the MC extrapolation to full phase space of Eq. 6.15, with a relative error of $\sim 15.3\%$. In order to evaluate the systematic error in $\sigma^{b\bar{b}}_{\mathrm{FV}}$ induced by the uncertainty in the $\sigma^{c\bar{c}}$ measurement, it has been made vary by one 1 σ around the central value and the $\sigma^{b\bar{b}}_{\mathrm{FV}}$ recomputed. The variation of $\sim 9.0\%$ has been considered as systematic uncertainty.

SPD multiplicity cut

The correction factor due to GECs (see Sec. 6.3) enters directly into the $\sigma^{b\bar{b}}_{\mathrm{FV}}$ calculation. The estimation of the systematic error due to ϵ_{SPD} has been performed in the following way: the cross section $\sigma^{b\bar{b}}_{\mathrm{FV}}$ has been calculated separately for the two TCKs considered, let the two calculations be $\sigma^{b\bar{b}}_{\mathrm{2A}}$ and $\sigma^{b\bar{b}}_{\mathrm{2C}}$. For the TCK affected by SPD hit multiplicity cut, 0x2E002C, the number of observed data events after the correction has been used. Then the following

quantity has been calculated: MC statistics

$$\delta = \frac{|\sigma^{b\bar{b}}_{2\mathrm{A}} - \sigma^{b\bar{b}}_{2\mathrm{C}}|}{\sigma^{b\bar{b}}_{\mathrm{FV}}} \ .$$

The uncertainty only affects 0x2E002C sample, which accounts for roughly $\frac{1}{3}$ of the total data sample. Weighting δ with this factor and taking the result as the estimation for this systematic error, it comes out to be below $\sim 0.6\%$.

Limited MC statistics

MC statistics is limited and causes efficiencies to have non negligible fluctuations. In order to estimate the corresponding systematic uncertainty, the number of expected events $N^{c\bar{c}}_{\mathrm{exp}}$ and $N^{q\bar{q}}_{\mathrm{exp}}$ and the total efficiency $\epsilon^{b\bar{b}}_{\mathrm{FV}}$ are varied one by one by their statistical errors and the $\sigma^{b\bar{b}}_{\mathrm{FV}}$ recomputed. The sum in quadrature of relative errors is taken as systematic uncertainty and is found to be $\sim 10.5\%$.

Trigger and Stripping Efficiency

The systematic uncertainties related to trigger and stripping efficiency estimation have been estimated making the corresponding efficiencies (Eqs. 5.7-5.9) vary by one sigma around their central value. A safe value of $\sim 3\%$ will be considered to account for both biases due to the trigger and to the not completely inclusive character of the stripping lines chosen.

6.7.1 Track multiplicity

The underestimation by the simulation models of the charged particle production, as found in 2010 data, is a known issue [79]. This is clear from Fig. 6.5, where the multiplicity of long tracks in 2010 data is compared with MC10 prediction.

This issue affects event properties such as seed multiplicity and consequently the seeding efficiency. In order to evaluate the related systematic error, MC $b\bar{b}$-inclusive and data events accepted by trigger and stripping have been considered. The data sample is used to get the multiplicity distribution of long tracks that fulfil the kinematic requirements for seed reconstruction, shown in Fig. 6.6. Each of the n bins of the distribution, which is normalized to unitary area, assumes the meaning of weight ω_i. The MC seeding efficiency is then

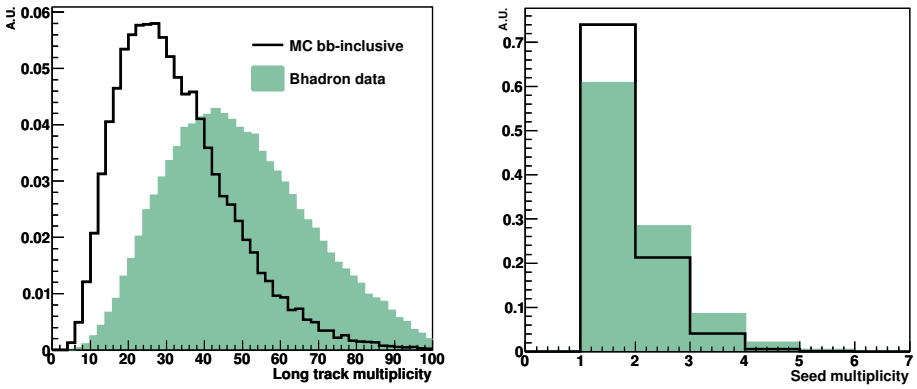

Figure 6.5: *Left*: Multiplicity of long tracks in 2010 data compared to the prediction in MC10 $b\bar{b}$. *Right*: seed multiplicity in data and MC.

computed in bins of the same charged track multiplicity, Fig. 6.7 [1]. Weight ω_i from data are used to calculated the corrected mean seeding efficiency:

$$\epsilon_{\text{seed}}^{\text{corr}} = \frac{\sum_i \epsilon_{\text{seed}}^i \cdot \omega_i}{n} \ ,$$

where ϵ_{seed}^i is the MC seeding efficiency in the corresponding bin of track multiplicity. The following quantity is computed:

$$\Delta\epsilon = |\langle\epsilon_{\text{seed}}\rangle - \epsilon_{\text{seed}}^{\text{corr}}| \ ,$$

where $\langle\epsilon_{\text{seed}}\rangle$ is the mean MC seeding efficiency evaluated without correction. The cross section $\sigma_{\text{FV}}^{b\bar{b}}$ is then recalculated making the seeding efficiency vary by $\Delta\epsilon$. The difference with the quoted measurement, $\sim 3.6\%$, is taken as systematic error due to the charged production underestimation.

Tracking efficiency

The efficiency of track reconstruction [80] has been considered as possible source of systematic uncertainty. The tracking perfomance in 2010 data taking is shown Fig. 6.8. Making the safe assumption that the error associated with the tracking efficiency converts into an equivalent fluctuation of the seeding

[1] The seeding efficiency quoted in Eq. 5.5 and used in the $\sigma_{\text{FV}}^{b\bar{b}}$ calculation cannot be compared to the values reported in the figure, since for the systematic error evaluation events after trigger and stripping selection have been used.

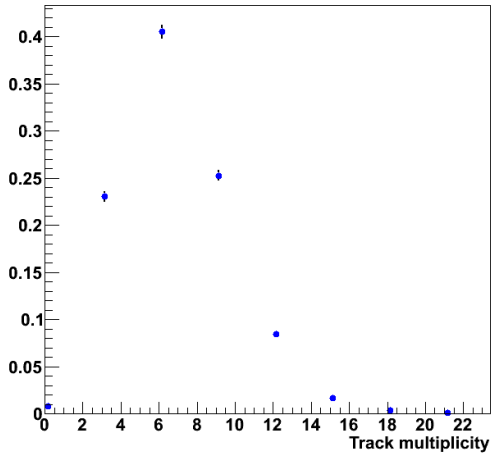

Figure 6.6: Track multiplicity in Bhadron data after track selection cuts, normalized to unitary area. Each bin assumes the meaning of weight ω_i in the systematic error evaluation.

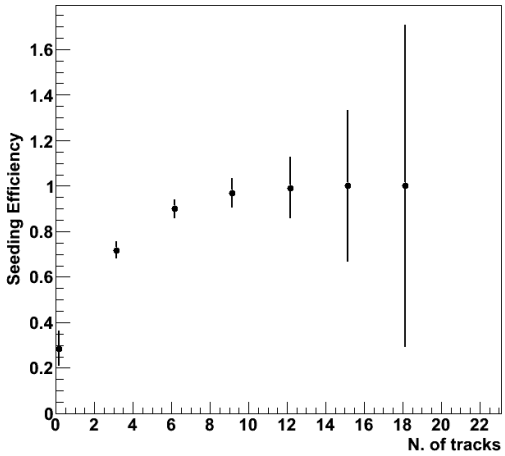

Figure 6.7: Seeding efficiency as a function of the number of tracks in MC $b\bar{b}$-inclusive. Tracks have been considered after applying the selection cuts as in the seeding procedure.

efficiency, the estimation leads to consider a 1.1% systematic error.

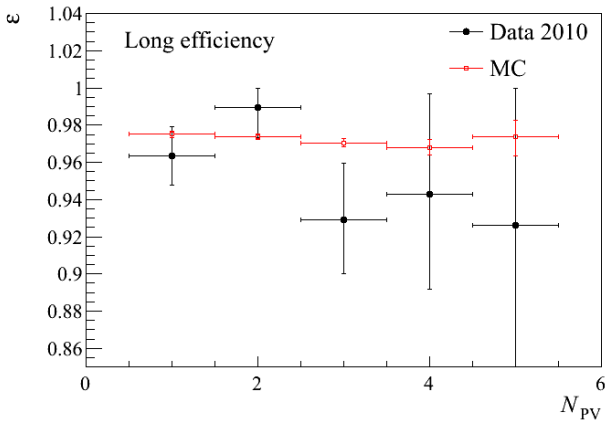

Figure 6.8: Tracking efficiency for long tracks as a function of the number of reconstructed PV.

6.8 Conclusions

The production cross section of $b\bar{b}$ pairs in pp collisions at $\sqrt{s} = 7\,\text{TeV}$ in the pseudorapidity region $\eta \in (2.5, 4.0)$ has been calculated to be

$$\sigma_{\text{FV}}^{b\bar{b}} = 80.6 \pm 1.2\ (\text{stat}) \pm 11.4\ (\text{syst})\,\mu\text{b}\ . \tag{6.24}$$

A NLO calculation made with POWHEG [81] using CTEQ6.6 PDFs yields $\sigma_{\text{NLO}}^{b\bar{b}} = (249.8 \pm 98)\,\mu\text{b}$ where the error contains the theoretical uncertainties due to PDF and scale variation. In order to compare with the measurement, one has to extrapolate the measurement to 4π: according to PYTHIA the factor is 3.93, yielding for the total $b\bar{b}$ cross section: $\sigma^{b\bar{b}} = 316.8 \pm 131.4\,\mu\text{b}$, which turns out to be compatible with the NLO calculation within 1 sigma. The experimental result is ~ 1.27 times bigger than the NLO calculation. A similar discrepancy between theoretical and experimental results has been published by the CMS collaboration [82].

The major contribution to the uncertainty of the measurement is given by the MC statistics: on the one hand its uncertainty enters directly in the measurement through the MC-based selection efficiencies as a systematic fluctuation; on the other hand a significantly higher statistics would allow to perform a template fit of data to get the relative fractions of the selected data sample, thus avoiding to make use of the measured $c\bar{c}$ cross section.

The analysis will take advantage of the forthcoming MC11 inclusive productions with trigger prefiltered events, thus allowing access to the huge amount

of data taken in 2011 and 2012. The incoming reprocessing of data will include a dedicated stripping line for the selection of inclusive b-jets, thus significantly reducing the uncertainties coming from the offline selection.

These improvements allow to set some prospects for the near future: 1) the measurement of the differential cross section $\frac{d\sigma^{b\bar{b}}}{dx}$, where x can be the pseudorapidity η, the di-jet invariant mass and the di-jets $\Delta\phi$; 2) the study of the $b\bar{b}$ angular correlations, Fig. 6.9 which will allow to investigate the $b\bar{b}$ production mechanisms.

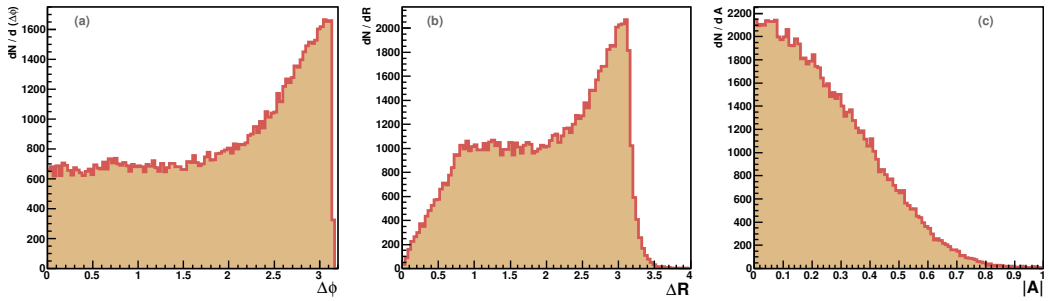

Figure 6.9: Di-jet angular correlations and p_{T} asymmetry as found in observed events in 2010 data. (a) and (b): $\Delta\phi$ and ΔR between the two jets; (c) jet p_{T} asymmetry $|A| = \frac{|p_{\mathrm{T}_1} - p_{\mathrm{T}_2}|}{p_{\mathrm{T}_1} + p_{\mathrm{T}_2}}$.

Appendix

The analysis relies on the LHCb standard Monte Carlo simulation campaign called MC10 [83]. This MC production properly describes the physical events collected during the 2010 run at $\sqrt{s} = 7\,\text{TeV}$. MC10 events are flagged according to the `Stripping12` [84] version of the LHCb stripping software. In this version, the Bhadron stream groups 65 stripping selection lines, with the aim of covering the widest possible range of b-flavoured hadron decays.

No dedicated stripping selection for b-jet analyses was implemented in 2010, therefore a choice of the most suitable stripping lines has been necessary, also to keep systematic uncertainties under control. The `B2DX*` group of stripping lines [85], accounting for almost the 80% of the MC10 $b\bar{b}$ inclusive events accepted by the whole Bhadron stream, has then been chosen. Tab. 6 summarized the stripping lines belonging to the `B2DX*` group, for each of which the corresponding prescale factor is shown. The lines with prescale factor different than 1 have not been taken into account, causing a further loss of efficiency of about 14%.

The `B2DX*` group collects the stripping lines devoted to the selection of decays of the form $B \to DX$, where $D = D^+, D^0, D_s^+$ and $X = \pi, K, K^*, \phi$. The allowed decay modes of the intermediates are listed in Tab. 7.

The default selection is based on a χ^2 cut on the impact parameters and flight significances (with respect to the offline selections). This selection deliberately uses no RICH information, since the channels in the $B \to DX$ family are kinematically identical to each other and are the dominant non-combinatoric backgrounds to each other. The signal efficiency for the various channels ranges between 80% and 95%.

BHadron Stripping line	Prescale factor
B2DXWithD2KPiPi0Merged	1.0
B2DXWithD2KPiPi0Resolved	1.0
B2DXWithD2Kshh	1.0
B2DXWithD2hhLine	1.0
B2DXWithD2hhWS	0.1
B2DXWithD2hhh	1.0
B2DXWithD2hhhWS	0.1
B2DXWithD2hhhh	1.0
B2DXWithLambda	1.0
B2DXWithUnbiasedB2DPi	0.1

Table 6: B2DX* lines of BHadron stripping and their prescale factor.

$K^* \to K\pi, \pi\pi$	to include the ρ
$\phi \to KK$	
$D^+ \to hhh$	$h = \pi, K$ all combinations except KKK
$D^s \to hhh$	$h = \pi, K$ all combinations except KKK
$D^0 \to hh$	$h = \pi, K$ all combinations
$D^0 \to hhhh$	$K\pi\pi\pi$, and $KK\pi\pi$ are considered
$D^0 \to K\pi\pi^0$	
$D^0 \to K^0_S hh$	$h = \pi, K$ all combinations

Table 7: Intermediate decay modes allowed in B2DX* stripping lines.

Cuts

A global event cut is applied on the number of long tracks, which are required to be < 100.

The cuts common to all charged daughters are summarized in Tab. 8, Tab. 9 show the cuts applied on K^*, ρ and ϕ, cuts on D and Λ_c candidate are in Tab. 10, finally Tab. 11 illustrates the cuts on the B candidates.

Cut	Value	Comment
PID cut	none	
χ^2	< 5	
p_{T}	$> 250\,\mathrm{MeV}$	for π daughters in $D \to hhhh$, $p_{\mathrm{T}} > 150\,\mathrm{MeV}$
p	$> 2000\,\mathrm{MeV}$	for K daughters in $D \to hhhh$, $p > 3000\,\mathrm{MeV}$

Table 8: Common cuts applied to charged daughters.

Cut	$K^* \to K\pi$	$\rho \to \pi\pi$	$\phi \to KK$
Daughter p_{T}	$> 300\,\mathrm{MeV}$	$> 250\,\mathrm{MeV}$	$> 250\,\mathrm{MeV}$
Vertex χ^2	< 12	< 12	< 12
χ^2 of separation from PV	> 4	> 4	> 4
p_{T}	$> 1000\,\mathrm{MeV}$	$> 1000\,\mathrm{MeV}$	$> 1000\,\mathrm{MeV}$
Mass window	$150\,\mathrm{MeV}$	$150\,\mathrm{MeV}$	$150\,\mathrm{MeV}$

Table 9: Common cuts applied to K^*, ρ and ϕ.

Cut	$D \to hh$	$D \to hhh$	$D \to hhhh$	$D \to K^0_S hh$	$D \to K\pi\pi^0$
Mass window	$\pm 100\,\text{MeV}$	$\pm 100\,\text{MeV}$	$\pm 100\,\text{MeV}$	$\pm 100\,\text{MeV}$	$\pm 150\,\text{MeV}$
Vertex χ^2	< 12	< 12	< 10	< 12	< 10
Vertex separation from the best PV	> 36	–	> 36	> 100	> 36
p_T	$> 1000\,\text{MeV}$	$> 1500\,\text{MeV}$	$> 2000\,\text{MeV}$	$> 1500\,\text{MeV}$	$> 2000\,\text{MeV}$
DIRA wrt best PV	> 0.9	> 0.9	> 0.9	> 0.9	> 0.9
DOCA	$< 1.5\,\text{mm}$	$< 1.5\,\text{mm}$	$< 1.5\,\text{mm}$	$< 1.5\,\text{mm}$	$< 1.5\,\text{mm}$
χ^2 IP separation from PV among dau's	> 40	> 40	> 40	–	> 40
K^0_S mass window	–	–	–	$30\,\text{MeV}$	–
K^0_S vertex χ^2	–	–	–	< 16	–
K^0_S flight distance χ^2	–	–	–	> 4	–
π^0 p_T	–	–	–	–	$> 600\,\text{MeV}$
π^0 p	–	–	–	–	$> 2000\,\text{MeV}$

Table 10: Cuts on D and Λ_c candidate.

Cut	All	$B \to D\pi$ unbiased
Bachelor p_{T}	$> 500\,\mathrm{MeV}$	$> 500\,\mathrm{MeV}$
Bachelor p	$> 5000\,\mathrm{MeV}$	$> 5000\,\mathrm{MeV}$
Bachelor χ^2 separation from PV	> 16	–
Vertex χ^2	< 12	< 12
χ^2 of IP to PV	< 25	< 250
Lifetime	> 0.2 ps	–
DIRA wrt best PV	> 0.9998	–
Mass window	$\pm 500\,\mathrm{MeV}$	$\pm 500\,\mathrm{MeV}$

Table 11: Cuts on B candidates.

Resum en Català

Durant l'últim segle, les teories i descobriments sobre l'estructura fonamental de la matèria han donat lloc a una declaració notable: tot el que és visible en l'Univers està compost de dotze components bàsics anomenats partícules fonamentals, governades per quatre forces fonamentals. La dinàmica d'aquestes partícules fonamentals sota la influència de la interacció electromagnètica, la interacció feble i forta està molt bé descrita per la teoria quàntica dels camps relativista coneguda com a Model Estàndard de la física de partícules elementals (SM).

S'ha explicat amb èxit un munt de resultats experimentals i predits amb precisió una àmplia varietat de fenòmens. No obstant això, el Model Estàndard està lluny de ser una teoria completa de les interaccions fonamentals ([6, 7, 8]).

Cromodinàmica Quàntica

La Cromodinàmica Quàntica (QCD) és la teoria de les interaccions fortes que uneixen als quarks entre ells. La QCD també intervé en les forces entre els hadrons i així controla la formació dels nuclis. Les propietats fonamentals de la QCD no poden ser provades directament, ja que és una teoria no lineal que no és analíticament solucionable, però hi ha molta evidència indirecta que dona suport a aquesta teoria. A diferència de teories quàntiques de camps com l'electromagnetisme, per la qual l'expansió pertorbativa en la força d'interacció dona resultats molt precisos, la interacció QCD és tan fort que aproximacions pertorbatives fallen sovint. En conseqüència, poques prediccions precises es poden fer amb la teoria.

El lagrangià de QCD defineix les interaccions dels quarks i dels gluons i els seus propagadors. Ni els quarks ni els gluons són observats com partícules lliures. Els hadrons són singlets de color (es a dir neutre en el color) combinacions de quarks, anti-quarks i gluons. Les regles de Feynman pels propagadors i els vèrtexs d'interacció son determinades directament pel lagrangià. Les regles són útils només dins del context de teoria pertorbativa, la qual requereix que la força del acoplament sigui petita.

Necessitem doncs de una escala de referència per decidir quan una la teoria de pertorbació pot ser aplicada. Una possibilitat òbvia és escollir l'escala a la que la constant d'acoplament α_s entra a un règim d'acoplament fort ($\alpha_s \sim 1$), on la teoria de les pertorbacions deixa de ser vàlida.

Si anomenem Λ_{QCD} l'escala de QCD que fa divergir $\alpha_s(\Lambda_{\mathrm{QCD}})$, processos com la producció de quarks pesats que ocorren a una escala d'energia significativament per sobre de Λ_{QCD} poden ser manejats amb métodes perturbatius. Una mitjana mundial recent [17] de diverses mesures de α_s dona $\alpha_s(M_{Z^0}) = 0.1184 \pm 0.0007$, el valor corresponent de l'escala QCD és $\Lambda^{(5)}_{\mathrm{QCD}} = (213 \pm 9)\,\mathrm{MeV}$, on l'índex (5) significa que cinc sabors de quarks (u, d, s, c i b) han estats considerats sense massa a la massa $M_{Z^0} = 91.2\,\mathrm{GeV}$ del bosó neutre Z^0.

A QCD els estats finals sempre consisteixen d'hadrons, mentre els càlculs perturbatius de QCD tracten partons. Físicament, un partó energètic es fragmenta a molts partons, els quals llavors, en una escala temporal més llarga, experimenten una transició a hadrons, la hadronització. La teoria de les pertorbacions captura només una part petita d'aquesta dinàmica. La hadronització se sol representar amb models, implementats en els generadors Monte Carlo (MC).

La característica que destaca més del b quark és el seu pes,

$$m_b \gg \Lambda_{\mathrm{QCD}} \tag{1}$$

que implica que els b quarks es produeixin de manera significativa en processos perturbatius [20].

Es poden considerar diversos mecanismes *Leading Order* i *Next to Leading Order* de producció de quarks pesats dins de col·lidors de hadrons. Es poden identificar tres classes: creació de sabor, excitació de sabor i el *gluon splitting*.

Tot i que els esdeveniments de les diverses categories no poden ser plenament separats, hi ha tres variables que es poden mesurar i utilitzar per determinar el tipus de mecanisme de producció. La primera és l'angle entre els quarks en el pla transvers a la direcció dels protons. La segona és l'angle

respecte a la direcció dels protons. La terçera és la diferència normalitzada dels dos moments transversos $|A| = \frac{|p_{T_1} - p_{T_2}|}{p_{T_1} + p_{T_2}}$.

A energies de LHC, els processos NLO representen 90% de la producció de quarks b.

L'experiment LHCb

L'Organització Europea per la Recerca Nuclear (CERN), és el laboratori de física de partícules més gran del món, situat a la frontera entre França i Suïssa, prop de Ginebra i va ser establert el any 1954. Ara al 2012, CERN és suportat per 20 estats membres europeus i, amb participació de més de 80 països, ha esdevingut el focus mundial per la recerca en la física fonamental.

El col·lidor d'hadrons superconductor LHC és l'accelerador de partícules d'energia més alta al món, actualment produint col·lisions de protons a un energia al centre de massa de $\sqrt{s} = 8\,\text{TeV}$ [34].

El LHC està dissenyat per assolir una energia de col·lisió de 14 TeV amb una lluminositat instantània, $\mathcal{L}$, de $10^{34}\,\text{cm}^{-2}\,\text{s}^{-1}$. La secció eficaç de producció de parelles $b\bar{b}$ prevista a 14 TeV és de $500\,\mu\text{b}$, així que a LHCb es produiran 50000 parelles per segon quan el LHC està corrent a les condicions de disseny.

Durant el 2010 l'LHC va córrer amb una energia per feix de 3.5 TeV i una energia al centre de massa de 7 TeV. La lluminositat a LHCb va assolir gairebé $2{\times}10^{32}\,\text{cm}^{-2}\,\text{s}^{-1}$. Com a resultat el número mitjà de interaccions protó-protó per encreuament μ va superar 2.5, presentant un repte seriós per l'experiment LHCb que va ser dissenyat per córrer amb $\mu = 0.4$. No obstant això LHCb va aconseguir una eficiència de 89%, recollint $37.66\,\text{pb}^{-1}$ d'un total de lluminositat subministrada per LHC de $42.15\,\text{pb}^{-1}$.

El detector LHCb [39] està situat al punt d'interacció 8 del accelarador LHC, anteriorment ocupat per l'experiment DELPHI [40]. És dedicat a l'estudi de física dels sabors pesats a l'LHC. El seu objectiu principal és buscar evidències indirectes de nova física en la violació *CP* i en els decaïments rars dels hadrons que contenen quarks b (i c).

LHCb ha de ser capaç d'explotar el gran nombre d'hadrons B produit. Això requereix un *trigger* eficaç, robust i flexible per tal de suportar el complexe entorn hadronic. El *trigger* ha de ser sensible a molts estats finals diferents. El *trigger* té un nivell hardware, L0, i dos nivells software, HLT 1 i HLT 2.

Una excel·lent resolució de vèrtex i de moment és essencial per obtenir una bona resolució del temps propi, necessari per estudiar la ràpida oscil·lació del sistema $B_s^0 - \overline{B}_s^0$ i també per la resolució de la massa invariant. Finalment,

un sistema d'adquisició de dades amb alta amplada de banda i un potent processament en línia de les dades és necessita per optimitzar la presa de dades.

LHCb és un espectròmetre d'un sol braç amb una cobertura angular cap endavant d'aproximadament de 10 mrad a 300(250) mrad. La disposició de l'espectròmetre LHCb es mostra a la Fig. 1.

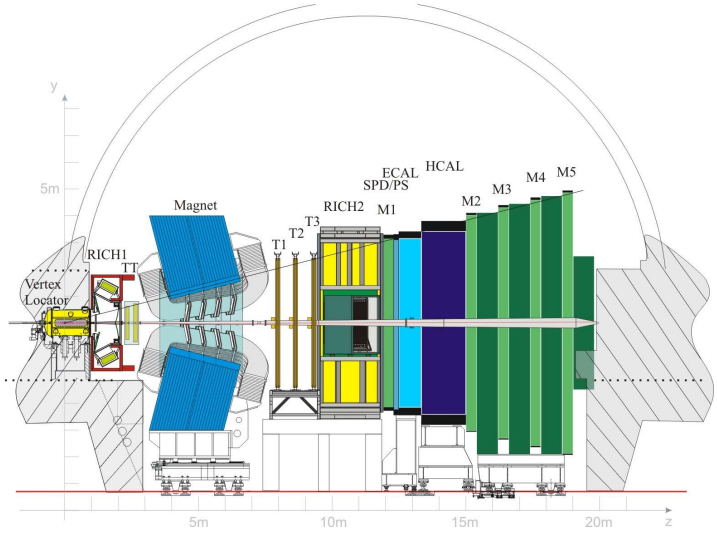

Figure 1: El detector LHCb.

La capacitat de LHCb per identificar vèrtexs desplaçats de decaïments de hadrons B es basa en un localitzador de traces de silici (VELO) posat al voltant del punt d'interacció [43]. Els productes de la desintegració dels hadrons B (hadrons que contenen quarks b) són detectats pels sistemes de *tracking* [1] i de calorimetria, i processos específics de desintegració es distingeixen amb la identificació (PID) de les espècies de partícules carregades amb el Ring Imaging Cherenkov (RICH) i els detectors de muons [44]. Els calorímetres proporcionen PID per fotons, electrons i els hadrons [45].

Caracterització del senyal

Una identificació eficient de *b-jets* (*jets* o dolls de partícules inicialitzats a partir de la fragmentació de un quark b) amb respecte a jets d'altres sabors

[1] El *tracking* és un sistema de detectors que reconstrueixen les trajectòries (traces) de partícules carregades que es produeixen com a conseqüència de la interacció inicial.

ha d'aprofitar necessàriament les propietats de producció i desintegració dels hadrons B.

Donat que l'objectiu de l'anàlisi és mesurar la secció eficaç de producció de *bottom* a LHCb usant estats finals inclusius amb sabor b, també és indispensable la investigació de les correlacions entre la producció del quark b i el corresponent hadró B, així com les correlacions entre la parella $b\bar{b}$ i la parella resultant de hadrons B. Prediccions Monte Carlo permeten estimar com les propietats del quark es modifiquen en passar al nivell d'hadró per processos com la fragmentació. El mètode aquí utilitzat s'espera que sigui menys afectat per efectes no pertorbatius que altres mesures basades en canals de decaïment exclusius.

S'han utilitzat produccions Monte Carlo d'esdeveniments completament simulats per estudiar les propietats dels quarks b i dels hadrons B, així com per a l'estudi dels quarks c i quarks lleugers. Aquests simulacions són de la campanya de producció 2010, anomenada MC10, en què les simulacions s'han realitzat amb les configuracions del detector i del trigger en ús en el 2010, a $\sqrt{s} = 7\,\text{TeV}$ i proporcionen una descripció coherent de les col·lisions recollides.

A la Fig. 2 es mostra la ratio entre el moment (i el p_{T}) del hadró B i del quark b. La forma dóna una indicació de la funció de fragmentació implementada en PYTHIA per la hadronització del quark b. El valor més probable és pròxim a la unitat, en la majoria dels casos el moment del hadró no es desvia significativament del moment del quark.

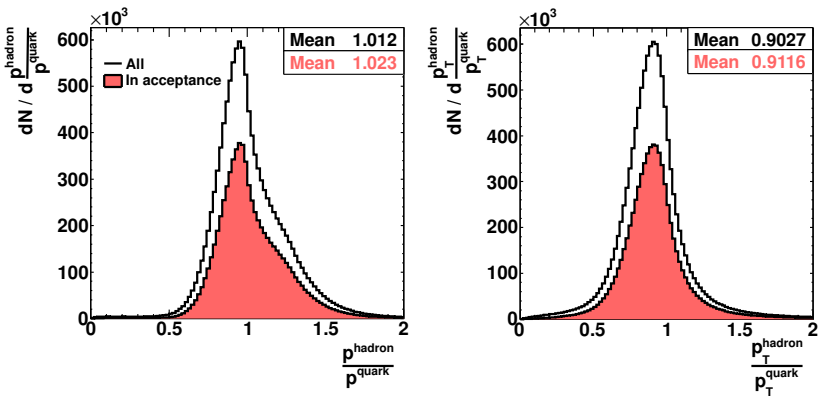

Figure 2: Ratio entre the p (p_{T}) del hadró B i el quark b corresponent, quan ambdós estàn dins de l'acceptància de LHCb.

La figura 3 mostra la distància entre els dos quarks d'una parella $b\bar{b}$ i entre els dos hadrons derivats d'ells, expressada en termes de la diferència en l'angle

azimutal $\Delta\phi$, la pseudorapidesa $\Delta\eta$, i $\Delta\mathrm{R} = \sqrt{\Delta\eta^2 + \Delta\phi^2}$. Per als nostres propòsits val la pena destacar com el hadró B conserva les propietats del quark b.

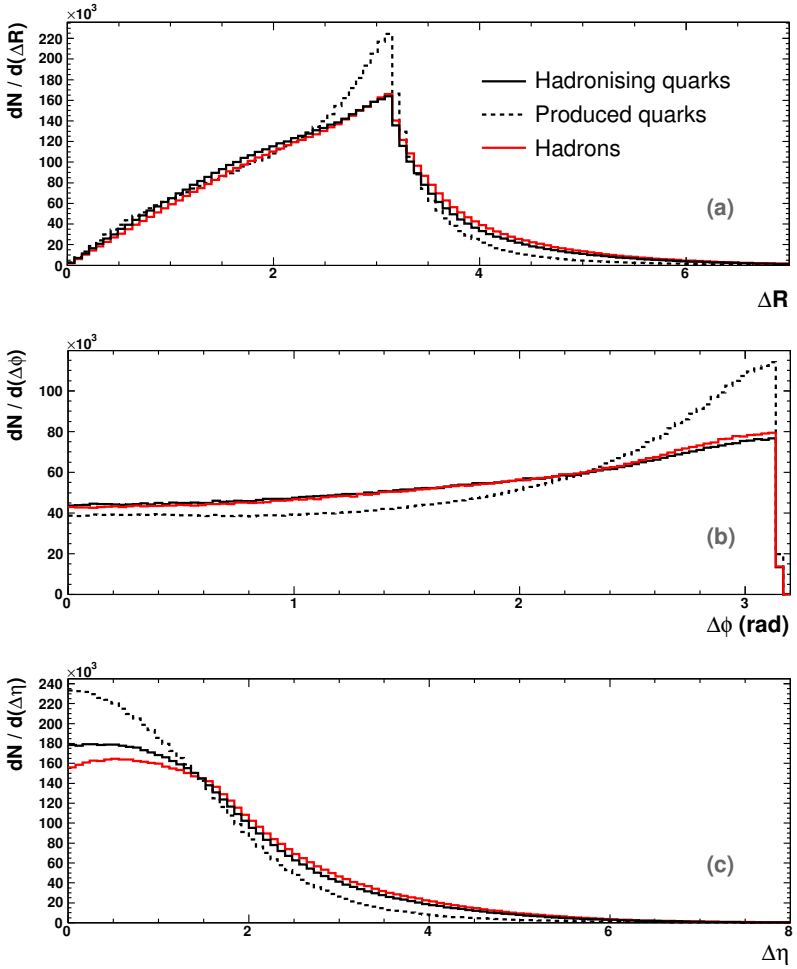

Figure 3: $\Delta\mathrm{R}$ (a), $\Delta\phi$ (b) and $\Delta\eta$ (c) entre el quark b i el $\bar{b}$. En vermell, distributions per les parelles de hadrons B.

El fons per l'anàlisi consisteix en una component física, principalment de jets d'hadrons que deriven de la hadronització de quarks *charm* i lleugers, i un fons combinatori, definit com els esdeveniments en què una parella $b\bar{b}$ ha estat efectivament produïda i l'algoritme reconstrueix jets no físicament associats als quarks de senyal. La part combinatòria requereix una definició de jet i es tractarà més endavant.

S'han utilitzat simulacions Monte Carlo de esdeveniments $c\bar{c}$ inclusius en col·lisions pp, amb els mateixos paràmetres de producció dea la producció de $b\bar{b}$ inclusiu.

Les figures 4 i 5 mostren respectivament el moment i el p_{T} de quarks c i de hadrons c. La forma d'aquestes distribucions es comparen amb les distribucions corresponents per quarks i hadrons *beauty*. El moment transvers del quark b és més o menys el doble del p_{T} del quark c. Aquesta diferència augmenta encara més en el cas dels hadrons. Buscar vèrtexs secundaris amb alt p_{T} (aquí també ens hi referirem com a *seeds*) té per tant un poder de discriminació també contra el fons de *charm*.

Selecció del senyal

Comparat amb altres experiments, el detector LHCb té una excel·lent capacitat per identificar vèrtexs secundaris desplaçats respecte al punt d'interacció. Aquest és un assoliment obligatori per la seva primera finalitat d'estudiar la violació de *CP* en el sistema dels mesons B i està assegurat per l'alta resolució del Localitzador de Vertex VELO.

LHCb també és capaç de proporcionar una mesura precisa de les trajectòries de les partícules i de les quantitats de moviment, gràcies a l'actuació del sistema de *tracking*. Moltes propietats cinemàtiques i de vida pròpia de la desintegració dels hadrons B estàn a la base de la identificació dels b-jets (b-*tagging*), de manera que el detector LHCb podria ser adequat per dur a terme estudis QCD basats sobre de jets de sabors pesats.

Altres propietats dels mesons B que poden ser explotades per al rebuig de fons són la seva gran massa i la multiplicitat de traces a l'estat final.

L'eina de *tagging* (o etiquetatge) desenvolupada per identificar els jets provinents de la hadronització del quark b és un algoritme de tipus *con*: la idea bàsica és prendre un vèrtex inclusiu secundari procedent de un hadró B com a *seed* (*llavor*) per a la reconstrucció del jet. La posició del seed respecte al vertex primari (PV) estableix la direcció d'un con d'obertura donada. El jet es construeix recollint les partícules carregades i neutres que es troben a l'interior del con. El radi del con s'expressa en termes del paràmetre adimensional R_{c}.

El mètode està físicament justificat pel fet que la massa del quark b és pesada, i per tant les propietats del hadró B estàn a prop de les del quark, depenent menys en el procés de fragmentació de mesures basades en canals de decaïment exclusius. Un avantatge d'aquest mètode és l'alta estadística que permet explorar correlacions angulars entre els parells $b\bar{b}$ i una regió cinemàtica

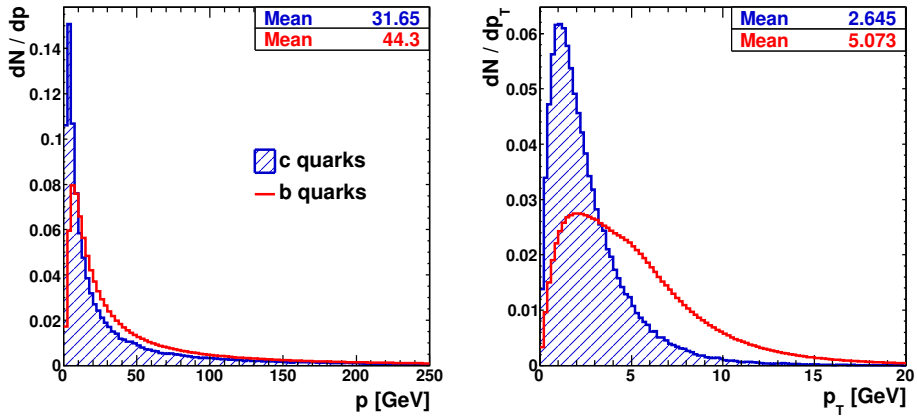

Figure 4: Moment (p) i moment transverse (p_{T}) dels quarks c (blau) comparat amb els quarks b.

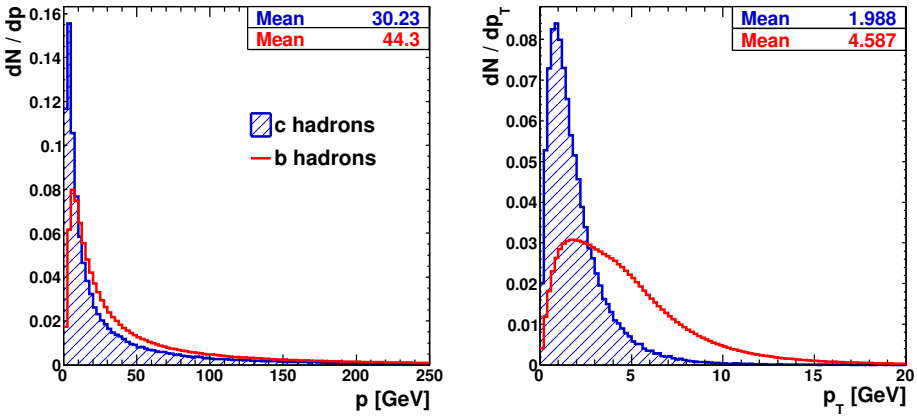

Figure 5: Moment (p) i moment transverse (p_{T}) dels hadrons c (blau) comparat amb els hadrons b.

més gran en comparació amb reconstruccions exclusives.

Selecció dels esdeveniments

Els esdeveniments candidats es seleccionen en primer lloc sobre la base de la decisió del trigger L0 i HLT. Els esdeveniments utilitzats estàn acceptats per la presència d'una partícula de alt p_{T} amb alt paràmetre d'impacte, i seleccionats a nivell de HLT per la possible presència d'una desintegració de hadrons B.

Ja que les dades reals per anàlisi de física han estat reprocessades i filtrades a través del procés de *stripping*, només estan disponibles en *streams* que són conjunts de línies de selecció exclusives. L'elecció per a aquesta anàlisi va caure de forma natural en el stream anomenat Bhadron. Per tal de canalitzar les incerteses sistemàtiques, només s'ha considerat un grup de línies Bhadron.

La selecció d'esdeveniments també requereix la reconstrucció d'un sol vèrtex primari, determinat per almenys 5 partícules carregades (veure [69] per obtenir detalls sobre la reconstrucció estàndard dels PV). Aquest requisit redueix significativament l'estadística. Per altra banda, rebutja esdeveniments en els que hi ha més d'una interacció pp, per tal d'evitar la dificultat d'assignar els seeds reconstituïts al PV corresponent.

Finalment als esdeveniments s'aplica el requisit de tenir almenys un vèrtex secundari reconstruït.

El algoritme de Seeding

El procediment és basa en la recerca d'un parell de traces que formin un bon vèrtex i que probablement siguin part dels productes de la desintegració d'un hadró B. Les traces carregades candidates és seleccionen entre traces *long*[1] amb requisits sobre l'impuls transvers, qualitat de la reconstrucció de les traces i significància del paràmetre d'impacte respecte al PV. Els talls aplicats es resumeixen en la taula Tab. 1. La bondat del vèrtex reconstruït és assegurada utilitzant els talls mostrats a la taula Tab. 2.

Els seeds reconstituïts descriuen bé la direcció dels hadrons B: la resolució ϕ i θ avaluats per els seeds de senyal resulta ser (15.8 ± 0.2) mrad i (1.82 ± 0.18) mrad respectivament.

Parells de seeds reconstruïts que tenen $\Delta\phi \sim 0$ és molt probable que procedeixen de la mateixa B o de la cadena $B \to D$. Dos seeds es fusionen en un sol seed si la massa invariant de totes les traces en els dos seeds està per sota

[1] Long tracks: traces llargues, definides com aquelles que creuen el sencer sistema de *tracking*.

	Cut
Track momentum	> 2.0 GeV
Track p_T	> 0.6 GeV
First track χ^2/ndf	< 2.5
Second track χ^2/ndf	< 3.0
IPS wrt PV	> 2.5

Table 1: Talls utilitzats per la selecció de les traces en el proces de seeding.

	Cut
Sum of tracks charge	0
Seed p_T	> 1.0 GeV
$z_{\rm PV} - z_{\rm SV}$	> 1 mm
Secondary vertex χ^2/ndf	50
DOCA	< 3 mm
ΔR_{ij}	< 1.4
$\lvert M_{\rm seed} - M_{K^0_{\rm S}}\rvert$	$> 10\,$MeV
$\lvert M_{\rm seed} - M_{\Lambda}\rvert$	$> 10\,$MeV

Table 2: Talls sobre els vèrtexs secundaris reconstruïts.

de 4.0 GeV. Al seed resultant se li assignen els millors paràmetres possibles. La fusió de seeds permet reduir significativament la fracció de seeds falsos que afecten fortament la regió amb petit $\Delta\phi$.

Per construcció, l'etiquetatge dels hadrons B de l'algoritme de reconstrucció del jet està implícit en el procediment: els vèrtexs secundaris són seleccionats tenint en compte les característiques que caracteritzen el decaïment del B. L'eficiència de tagging es calcula utilitzant el Monte Carlo i es defineix com el ratio entre el nombre de seeds de senyal i el nombre d'hadrons B generats en l'acceptància de LHCb. La eficiència mitjana de b-tagging és $(59.0 \pm 0.4)\%$.

Reconstrucció dels jets

La línia de vol dels hadrons B es reprodueix amb bona precisió per la posició del seed respecte al PV. Els jets es construeixen sumant al quadrimoment del seed altres partícules carregades i neutres que es troben dins d'un con amb l'eix que coincideix amb la trajectòria del seed. La figura 6 mostra la massa invariant i el $p_{\rm T}$ dels b-jets, comparats amb jets procedent de quark c o lleugers.

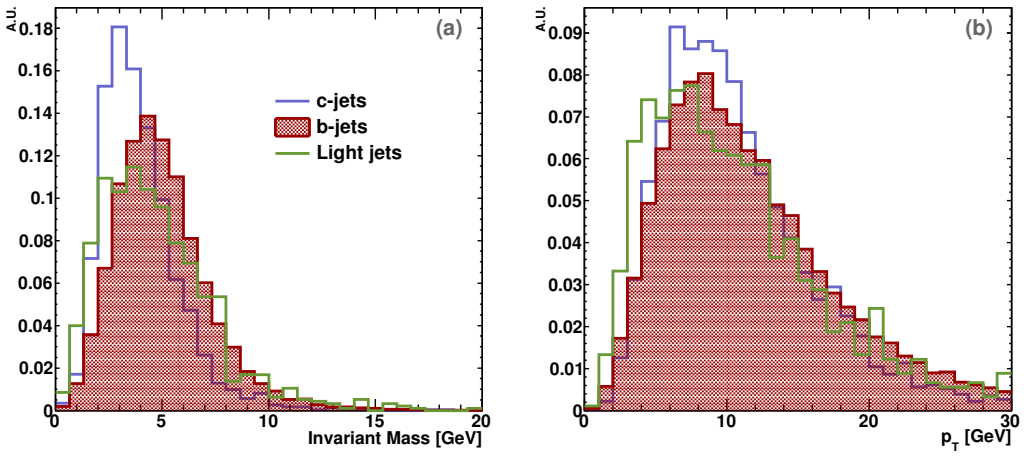

Figure 6: Massa invariant (a) i moment transverse (b) de b-, c- and jets lleugers. Les distribuccions són normalitzades a la mateixa àrea.

En el procediment de reconstrucció dels jets, les traces addicionals estan inicialment lliures de ser assignades a un o més jets, amb la finalitat d'estudiar la superposició dels jets. Com a conseqüència, ha de ser fixat un criteri per fusionar o dividir jets superposats. Dos jets es fusionen en un sol jet si la fracció d'energia compartida entre ells es $F_{E\text{shared},ij} > 0.4$.

L'últim pas del procediment de reconstrucció és la separació dels jets: partícules compartides per dos jets per els quals $F_{E\text{shared},ij} < 0,4$ són unívocament assignades al jet més a prop en ΔR.

Eficiències de trigger i stripping

Dues mostres de senyal que contenen els esdeveniments amb almenys un seed reconstruït i almenys dos seeds s'han obtingut a partir de $\sim$ 6M de esdeveniments MC $b\bar{b}$. La eficiència de reconstrucció de almenys un o dos seeds a partir de una mostra amb un vertex primari es:

$$\epsilon_{1\text{seed}} = (18.07 \pm 0.03)\% \quad (2)$$

$$\epsilon_{2\text{seed}} = (3.00 \pm 0.01)\% \ . \quad (3)$$

Les línies del trigger L0 més eficients per a les dues mostres de senyal resulten ser `L0Hadron` i `L0Muon`, per tant s'han utilitzat esdeveniments acceptats per una de aquestes dues línies.

A aquests esdeveniments es demana que tinguin resposta positiva per una

de les línies `Hlt1Track` del trigger HLT1. Les línies topològiques del trigger HLT2 han estat elegit per a la selecció d'esdeveniment a la etapa HLT2 del trigger de alt nivell de LHCb.

La eficiència global del trigger per a les mostres amb almeny un o dues seeds és:

$$\epsilon^{\text{1seed}}_{\text{trigger}} = (4.09 \pm 0.04)\% \tag{4}$$
$$\epsilon^{\text{2seeds}}_{\text{trigger}} = (11.3 \pm 0.2)\% \ . \tag{5}$$

la dependència de l'eficiència del trigger de η es mostra suficientment estable en el rang de $\eta \in [2.5, 4.0]$, de manera que la measura es limitarà a aquesta interval de η.

Com que no hi ha línies de stripping dedicades a l'anàlisi dels b-jets i $\sim 80\%$ dels esdeveniments acceptats per les línies de stripping Bhadron són acceptats per les línies `B2DX*`, s'ha utilitzat aquest grup de línies en l'anàlisi i se n'ha determinat l'eficiència respecte al número d'esdeveniments acceptats per el trigger:

$$\epsilon^{\text{1seed}}_{\text{stripping}} = (9.3 \pm 0.3)\% \tag{6}$$
$$\epsilon^{\text{2seeds}}_{\text{stripping}} = (10.6 \pm 0.5)\% \ . \tag{7}$$

Correcció de l'energia dels jets

Abans de qualsevol comparació entre MC i les dades i amb la finalitat de definir un tall fiduciari en p_{T} dels jets, cal fer una correcció de l'energia per tenir en compte la pèrdua d'energia a causa de partícules no detectades o per mesures no correctes de l'energia o del tracking.

La idea és calibrar l'energia dels jets utilitzant jets a nivell de generador Monte Carlo. Aquests jets es construeixen utilitzant partícules detectables generades i prenent la línia de vol del B com direcció del con. El ratio entre l'energia dels jets a nivell de generador i l'energia dels jets reconstruïts ($E_{\text{true}}/E_{\text{jet}}$) s'ha ajustat mitjançant la fórmula:

$$f_{corr}(E_{\text{jet}}) = p_0 + \frac{p_1}{E_{\text{jet}} + p_2} \ , \tag{8}$$

on els p_i són parametres lliures. L'energia dels jets s'ha corregit després aplicant la fórmula:

$$E^{\text{corr}}_{\text{jet}} = E_{\text{jet}} \cdot f_{\text{corr}}(E_{\text{jet}}) \tag{9}$$

La resolució de l'energia dels jets corregits utilitzant dos diferents valors $R_{\rm c} = 0.7$ i $R_{\rm c} = 0.8$, resulta $\sigma_{0.7} = 0.204 \pm 0.008$ i $\sigma_{0.8} = 0.196 \pm 0.008$ respectivament.

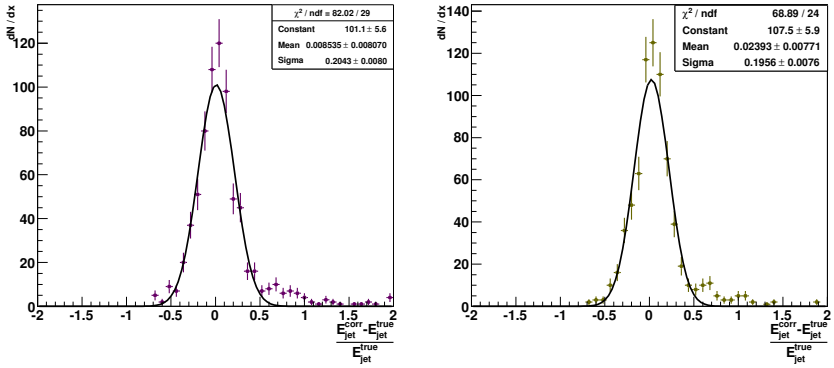

Figure 7: Resolució de l'energia dels jets corregits utilitzant dos diferents valors pel radi del con: $R_{\rm c} = 0.7$ i $R_{\rm c} = 0.8$.

Resultats

L'objectiu de l'anàlisi és calcular la secció eficaç de producció de parells $b\bar{b}$ dins el volum fiduciari (FV) $\eta \in (2.5, 4.0)$ utilitzant una fórmula com:

$$\sigma^{b\bar{b}}_{\rm FV} = \frac{N^{\rm obs} - N^{\rm bkg}}{\mathcal{L} \times \epsilon^{b\bar{b}}} \ , \tag{10}$$

on $N^{\rm obs}$ es el número de esdeveniments candidats trobats en les dades reals, $N^{\rm bkg}$ és la suma de les contribucions dels quarks *charm* i lleugers estimades amb el MC, $\mathcal{L}$ és la lluminositat integrada de les dades i $\epsilon^{b\bar{b}}$ es la eficiència total de selecció calculada utilitzant les simulacions MC $b\bar{b}$ inclusives.

Les dades analitzades són les recollides en el 2010 amb col·lisions a $\sqrt{s} = 7\,\text{TeV}$, preses amb dues configuracions del trigger molt similars. La lluminositat integrada corresponent és $\sim 17.7\,\text{pb}^{-1}$, la meitat de la lluminositat total recollida en el 2010. Ja que no hi ha cap selecció dedicada a l'anàlisi de jets, l'extracció de la secció eficaç s'ha realitzat utilitzant esdeveniments seleccionats per un conjunt reduït de línies de stripping del *stream* Bhadron.

Només els esdeveniments amb exactament un PV han estat considerats. La lluminositat integrada que resulta d'aquesta elecció es $\mathcal{L}_{\rm eff} = 2.65\,\text{pb}^{-1}$.

Selecció final

La selecció final aplicada a les dades i a les mostres de MC es pot resumir en les següents etapes consecutives:

1. Selecció de esdeveniments amb un PV;
2. Reconstrucció dels seeds i selecció de esdeveniments amb almenys un seeds reconstruït;
3. Trigger i Stripping;
4. Reconstrucció dels jets, on els processos de fusió y separació influeixen en el número de jets per esdeveniment;
5. Talls fiduciaris: η dels jets $\in (2.5, 4.0)$ i p_{T} del jet més gran que $5\,\mathrm{GeV}$;
6. Selecció final de esdeveniments amb exactament dos jets reconstruïts.

Eficiència de selecció $\epsilon_{\mathrm{FV}}^{b\bar{b}}$

L'eficiència total de la selecció d'esdeveniments en què ha estat produït un parell $b\bar{b}$ dins del FV es pot expressar com producte de les eficiències:

$$\epsilon_{\mathrm{FV}}^{b\bar{b}} = \epsilon_{\mathrm{1seed}} \cdot \epsilon_{\mathrm{trigger}} \cdot \epsilon_{\mathrm{stripping}} \cdot \epsilon_{\mathrm{sel}} \ , \tag{11}$$

on el terme ϵ_{sel} ten en compte le reconstrucció del jets, el talls fiduciaris i la selecció de esdeveniments amb exactament dos jets reconstruïts. El valor calculat per $\epsilon_{\mathrm{FV}}^{b\bar{b}}$ es

$$\epsilon_{\mathrm{FV}}^{b\bar{b}} = (1.04 \pm 0.12) \times 10^{-4} \ . \tag{12}$$

Composició de la mostra de dades seleccionada

La composició de la mostra de dades seleccionada en termes de contingut b, c i quarks lleugers, s'ha determinat directament amb Monte Carlo. L'eficiència de selecció de cada tipus de fons s'ha calculat de manera similar a $\epsilon_{\mathrm{FV}}^{b\bar{b}}$. Les eficiències s'utilitzen per estimar el número esperat d'esdeveniments de fons seleccionats en una lluminositat integrada $\mathcal{L}_{\mathrm{eff}}$, fent servir les seccions eficaçes apropiades. El número d'esdeveniments $c\bar{c}$ esperats dins del FV es calcula amb la fórmula

$$N_{\mathrm{exp}}^{c\bar{c}} = \mathcal{L}_{\mathrm{eff}} \cdot \sigma^{c\bar{c}} \cdot \epsilon_{\mathrm{gen}}^{c\bar{c}} \cdot \epsilon^{c\bar{c}} \ , \tag{13}$$

on $\sigma^{c\bar{c}} = 6100\,\mu$b és la secció eficaç a 4π mesurada per LHCb [78], $\epsilon^{c\bar{c}}_{\text{gen}}$ és la eficiència del tall de acceptància del generador PYTHIA, $\epsilon^{c\bar{c}}$ és la eficiència de selecció calculada amb MC $c\bar{c}$ inclusiu. El número de esdeveniments esperat per la lluminositat $\mathcal{L}_{\text{eff}}$ corresponent a les dades reals s'ha estimat en

$$N^{c\bar{c}}_{\text{exp}} \approx 34258 \pm 1489 \ . \tag{14}$$

De manera similar s'ha calculat la contribució de jets de quark lleugers i gluons. El número esperat per aquest tipus d'esdeveniments es

$$N^{q\bar{q}}_{\text{exp}} \approx 14468 \pm 7837 \ . \tag{15}$$

Càlcul de la secció eficaç

Amb l'estratègia adoptada, la secció eficaç de producció $b\bar{b}$ dins del FV es pot calcular de la manera següent:

$$\sigma^{b\bar{b}}_{\text{FV}} = \frac{(N^{\text{DATA}}_{\text{obs}} - N^{c\bar{c}}_{\text{exp}} - N^{q\bar{q}}_{\text{exp}}) \cdot p}{\mathcal{L}_{\text{eff}} \cdot \epsilon^{b\bar{b}}_{\text{FV}}} \ , \tag{16}$$

on $N^{\text{DATA}}_{\text{obs}} = 87312$ és el número d'esdeveniments seleccionats en les dades reals agafades en el 2010, p es un factor que té en compte la puresa de la mostra seleccionada. La secció eficaç mesurada doncs és

$$\sigma^{b\bar{b}}_{\text{FV}} = (80.6 \pm 1.2)\,\mu\text{b} \ , \tag{17}$$

on s'ha indicat el error estadístic.

Errors Sistemàtics

S'han evaluat diverses fonts d'error sistemàtic resumides a la taula 3

Conclusions

La secció eficaç de producció de parells $b\bar{b}$ dins del Volum Fiduciari resulta

$$\sigma^{b\bar{b}}_{\text{FV}} = 80.6 \pm 1.2\ (\text{stat}) \pm 11.4\ (\text{syst})\,\mu\text{b} \ . \tag{18}$$

Un càlcul NLO fet fent servir el generador POWHEG [81] que utilitza les PDFs CTEQ6.6 ha donat $\sigma^{b\bar{b}} = (249.8 \pm 0.4)\,\mu$b, on l'error no conté les incerteses teòriques. Per poder comparar la predicció, cal extrapolar la mesura a 4π:

Font	Incertesa (%)
Lluminositat integrada	3.5
Secció eficaç $\sigma^{c\bar{c}}$	9.0
Talls Globals de Esdeveniment	0.6
Estadística MC	9.0
Eficiència del trigger i del stripping	3.0
Multiplicitat de traces	3.6
Eficiència del tracking	1.1
Total	14.1

Table 3: Fonts de error sistemàtic.

segons el generador PYTHIA el factor és 3.93. Per tant la secció eficaç total resulta ser $\sigma^{b\bar{b}} = 316.8 \pm 49.5\,\mu$b. El resultat experimental és ~ 1.27 vegades més gran que el càlcul a NLO. Una discrepància similar entre els resultats teòrics i experimentals ha estat publicat per la col·laboració CMS [82].

La principal contribució a la incertesa de la mesura està donada per la estadística MC: d'una banda la seva incertesa entra directament en la mesura a través de les eficiències de selecció basades en MC com una fluctuació sistemàtica, per altra banda una estadística significativament més alta permetria realitzar un ajust de les de dades per obtenir les fraccions relatives de la mostra de dades seleccionada, evitant així de fer servir la secció eficaç mesurada $\sigma^{c\bar{c}}$.

L'anàlisi aprofitarà de les pròximes produccions MC11 inclusives amb esdeveniments prefiltrats pel trigger, permetent així l'accés a l'enorme quantitat de dades preses al 2011 i 2012. A més a més el reprocessament de dades inclourà una línia dedicada per a la selecció b-jets inclusius, reduint així significativament les incerteses que vénen de la selecció offline.

Aquestes millores permeten establir algunes perspectives per al futur pròxim: 1) la mesura de la secció diferencial $\frac{d\sigma^{b\bar{b}}}{dx}$, on x pot ser η, la massa invariant del dos jets i el $\Delta\phi$; 2) l'estudi de les correlacions angulars entre els dos quarks $b\bar{b}$, que permeten investigar els mecanismes de producció dels parells $b\bar{b}$.

Resùmene in Sardu

In s'ùrtimu sèculu, is teorias e is iscobertas a pitzu de s'istrutura fundamentale de sa matèria ant donadu logu a una decraratzione notàbile: totu su chi est visìbile in s'Universu est cumpostu dae dòighi cumponentes de base, is partìculas[1] fundamentales, guvernadas dae bator fortzas fundamentales. Sa dinàmica de custas partìculas fundamentales suta s'influèntzia de s'interatzione eletromagnètica, s'interatzione dèbile e forte est descrita cun pretzisione dae sa teoria cuantìstica de is campos relativìstica connota comente Modellu Istandard de sa fìsica de is partìculas elementares (SM).

Si sunt ispricados meda resurtados isperimentales e previdìdos cun pretzisione una variedade ampra de fenòmenos. Nointames, su Modellu Istandard no est una teoria cumprida de is interatziones fundamentales ([6, 7, 8]).

Cromodinàmica Cuantìstica

Sa Cromodinàmica Cuantìstica (QCD) est sa teoria de is interatziones fortes chi aunint is quarks intre issos. Sa QCD interbenit fintzas in is fortzas intre is adrones e tando controllat sa formatzione de is nùcleos. Is propiedades fundamentales de sa QCD no podent èssere cuntrobadas a manera dereta, ca est una teoria non lineare chi no est resorvìbile in forma analìtica, b'at peroe evidèntzias deretas chi donant suportu a custa teoria. A diferèntzia de teorias

[1] Dae inoghe a in antis s'at a adotare su latinismu *partìcula*, issèberu idènticu a su de limbas che s'ispannolu e su cadalanu (e fintzas de s'inglesu, cun *particle*), istransende duncas s'impreu de su diminutivu *partighedda*, o de vocàbulos patrimoniales de orìgine latina comente *cantu, cantzu* (dae QUANTUM).

cuantìsticas de campos che a sa eletromagnètica, in ue s'espansione perturbativa in sa fortza de interatzione donat resurtados pretzisos meda, s'interatzione QCD est aici forte chi is aprossimatziones perturbativas fatu fatu faddint. In cunsighèntzia, pagas preditziones pretzisas si podent fàghere cun sa teoria.

Sa Lagrangiana de sa QCD definit is interatziones de is quarks e de is gluones e is propagadores issoro. Ne is quarks ne is gluones si podent annotare comente partìculas lìberas. Is adrones sunt singuletes de colore (est a nàrrere nèutros in sa càrriga de colore) cumbinatziones de quarks, anti-quarks e gluones. Is règulas de Feynman pro is propagadores e is bèrtighes de interatzione sunt determinados in manera dereta dae sa Lagrangiana. Is règulas faghet a ddas impreare petzi in intro de su cuntestu de sa teoria perturbativa, chi recheret chi sa fortza de acrobamentu siat pitica.

Tando bisongiamus de un'iscala de referèntzia pro dissinire cando sa teoria de is perturbatziones podet èssere aplicada. Una possibilidade òvia est de isseberare s'iscala in ue sa costante de acrobamentu α_s intrat in unu regime de acrobamentu forte ($\alpha_s \sim 1$), in ue sa teoria de is perturbatziones sessat de èssere vàlida.

Si naramus Λ_{QCD} s'iscala de sa QCD chi faghet divèrgere $\alpha_s(\Lambda_{\mathrm{QCD}})$, a is protzessos comente sa produtzione de quarks graes, chi acontessent a un'iscala de energia a subra de Λ_{QCD} in manera sinnificativa, faghet a ddos manigiare cun mètodos perturbativos. Una mèdia mundiale reghente, [17] de diferentes mesuras de α_s donat $\alpha_s(M_{Z^0}) = 0.1184 \pm 0.0007$, su valore de s'iscala QCD chi currespondet est $\Lambda^{(5)}_{\mathrm{QCD}} = (213 \pm 9)\,\mathrm{MeV}$, in ue s'ìndighe (5) sinnìficat chi chimbe sabores de quarks (u, d, s, c e b) sunt istados cunsiderados sena massa a sa massa $M_{Z^0} = 91.2\,\mathrm{GeV}$ de su bosone nèutru Z^0.

In QCD is istados finales cunsistent semper de adrones, mentras chi is càrculos perturbativos de sa QCD manigiant partones. Unu partone energèticu si frammentat in meda partones, chi, in un'iscala temporale prus longa, isperimentant una transitzione a adrones, s'adronizatzione. Sa teoria de is perturbatziones tenturat isceti una parte minore de custa dinàmica. S'adronizatzione si costumat a representare cun modellos, implementados in is generadores Monte Carlo (MC).

Sa caraterìstica chi si ponet prus in evidèntzia de su quark b est su pesu suo,

$$m_b \gg \Lambda_{\mathrm{QCD}} \tag{1}$$

chi ìmplicat chi is quarks b si produent in manera sinnificativa in protzessos perturbativos [20].

Si podent cunsiderare mecanismos diferentes *Leading Order* e *Next to Lead-*

ing Order de produtzione de quarks graes in intro de is collisores de adrones. Si podent dessinire tres classes: creatzione de sabore, etzitatzione de sabore e *gluon splitting*.

Mancari chi is eventos de is tres categorias diferentes no si podent ischertare in prenu, b'at tres variàbiles chi si podent medire e impitare pro istabilèssere sa genia de mecanismu de produtzione. Sa prima est s'àngulu intre is quarks in su pranu travessu a sa diretzione de is protones. Sa segunda est s'àngulu respetu a sa diretzione de is protones. Sa de tres est sa diferèntzia normalizada de is duos momentos travessos $|A| = \frac{|p_{\mathrm{T}_1} - p_{\mathrm{T}_2}|}{p_{\mathrm{T}_1} + p_{\mathrm{T}_2}}$.

A is energias de LHC, is protzessos NLO representant su 90% de sa produtzione de quarks b.

S'esperimentu LHCb

Su Tzentru Europeu pro sa Chirca Nucleare (CERN), est su laboratòriu de fisica de is partìculas prus mannu de su mundu, situadu in sa làcana intre Frantza e Svìtzera, acanta de Ginevra, e est istadu istabilèssidu in s'annu 1954. In su 2012, su CERN est suportadu dae 20 istados membros europeos e, cun sa partitzipatzione de prus de 80 paisos, s'est fatu su focus mundiale pro sa chirca in sa fisica fundamentale.

Su collisore adrònicu supercundutore LHC est s'atzeleradore de partìculas de energia prus arta in su mundu, oe in die produende collisiones de protones a un'energia in su tzentru de massa de $\sqrt{s} = 8\,\mathrm{TeV}$ [34].

Su LHC est disinnadu pro lòmpere a un'energia de collisione de 14 TeV cun una luminosidade istantànea, $\mathcal{L}$, de $10^{34}\,\mathrm{cm}^{-2}\,\mathrm{s}^{-1}$. Sa setzione de rugradura[1] de produtzione de crobas $b\bar{b}$ previdida a 14 TeV est de 500 μb, gai chi in LHCb s'ant a produère 5000 crobas a segundu cando LHC est currende cunforma sas cunditziones de progetu.

In s'annu 2010 s'LHC at curtu a un'energia pro cada fasche de protones de 3.5 TeV e un'energia in su tzentru de massa de 7 TeV. Sa luminosidade in LHCb at segudadu agiumai su valore de $2{\times}10^{32}\,\mathrm{cm}^{-2}\,\mathrm{s}^{-1}$. Nde resurtat chi su nùmeru mèdiu de interatziones protone-protone pro rugradura, μ, at coladu 2.5, presentende unu disafiu mannu pro s'esperimentu LHCb chi fiat desinnadu pro cùrrere a $\mu = 0.4$. Mancari aici, LHCb at cunsighidu un'efitzièntzia de

[1] Tradutzione dereta dae s'inglesu *cross section*, definitzione impreada pro sa prima bia dae Ernest Rutherford ("*Radiation of the α Particle from Radium in passing through Matter*", Philosophical Magazine (12, p 134-46)), duncas preferìbile pro resones istòricas a sa tradutzione dereta dae s'italianu *setzione d'urto*.

89%, regollende 37.66 pb^{-1} de unu totale de luminosidade sumministrada dae LHC de 42.15 pb^{-1}.

Su reveladore LHCb [39] est assentadu in su puntu de interatzione 8 de s'atzeleradore LHC, chi in antis fiat ocupadu dae s'esperimentu DELPHI [40]. Est dedicadu a s'istùdiu de sa fisica de is sabores graes in LHC. S'obietivu suo est chircare evidèntzias indiretas de fisica noa in sa violatzione *CP* e in is decadessimentos raros de is adrones chi cuntenent quarks b (e c).

LHCb depet èssere capatzu de bogare profetu dae su nùmeru mannu de adrones produìdos. Custu recheret un *trigger* eficatze, robustu e flessìbile, chi potzat poderare sa cumplessidade de s'ambiente adrònicu. Su *trigger* bolet sensìbile a meda istados finales diferentes. Su *trigger* de LHCb tenet unu livellu hardware, L0, e duos livellos software, HLT 1 e HLT 2.

Una resolutzione de bèrtighe e de momentu estremada est essentziale pro otènnere una resolutzione bona de su tempus pròpiu, netzessàriu pro istudiare s'oscillatzione lestra de su sistema $B_s^0 - \overline{B}_s^0$ e fintzas pro sa resolutzione de sa massa invariante. In fines, unu sistema de achirimentu de datos con amprària de banda manna e unu protzessamentu in lìnia poderosu sunt rechertos pro otimizare sa leada de datos.

LHCb est un'ispetròmetru a bratzu sìngulu, cun cobertura angulare fache a in antis de pagu prus o mancu 10 mrad a 300(250) mrad. S'assentu de s'ispetròmetru LHCb est mustradu in sa Fig. 1.

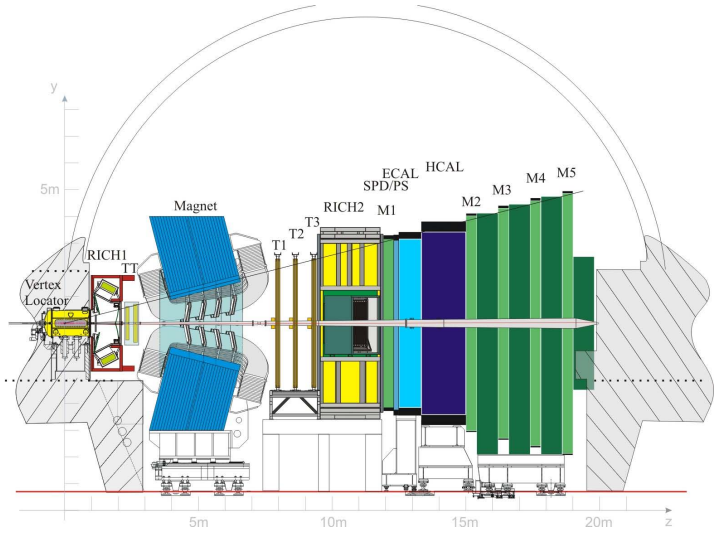

Figure 1: Su reveladore LHCb.

Sa capatzidade de LHCb de identificare bèrtighes istagiados de decadessimentu de adrones B si basat in unu localitzadore de trassas de silìtziu (VELO)

postu a inghìriu de su puntu de interatzione [43]. Is produtos de su decadessimentu de is adrones B sunt agatados dae is sistemas de *tracking*[1] e de calorimetria, e protzessos ispetzìficos de decadessimentu si distinghent cun s'identificatzione (PID) de is genias de partìculas càrrigas cun su Ring Imaging Cherenkov (RICH) e is reveladores de muones [44]. Is calorìmetros frunint su PID pro fotones, eletrones e is adrones [45].

Caraterizatzione de su sinnale

Un'identificatzione efitziente de *b-jets* (*jets* o tzurros de partìculas inghitzados moende dae sa frammentatzione de unu quark b) cunforma a jets de àteros sabores depet bogare profetu dae is propiedades de produtzione e decadessimentu de is adrones B.

Sende chi s'obietivu de s'anàlisi est sa mesura de sa setzione de rugradura de produtzione de *bottom* in LHCb impreende istados finales inclusivos cun sabore b, est pretzisu a iscumbatare fintzas is currelatziones intre sa produtzione de quark b e su currespondente adrone B, aici comente is currelatziones intre sa croba $b\bar{b}$ e sa croba de adrones resurtante $B\overline{B}$. Preditziones Monte Carlo permitent de istimare comente is propiedades de su quark mudant colende a su nivellu de adrone peri protzessos che sa frammentatzione. Su mètodu impitadu inoghe s'isetat chi siat prus pagu fertu dae efetos non perturbativos chi non àteras mesuras basadas in canales de decadessimentu esclusivos.

Sunt istadas impitadas produtziones Monte Carlo de eventos simulados a cumpretu pro istudiare is propiedades de is quarks b e de is adrones B, aici comente pro s'istùdiu de is quarks c e de quarks lèbios. Custas simulatziones sunt de sa campagna de produtzione 2010, numenada MC10, in ue is simulatziones sunt realizadas cun is cunfiguratziones de su reveladore e de su trigger impreados in su 2010 a $\sqrt{s} = 7\,\text{TeV}$ e frunint una descritzione coerente de is collisiones regortas.

In Fig. 2 si mustrat su raportu intre su momentu (e su p_{T}) de s'adrone B e de su quark b. Sa forma donat inditos a subra de sa funtzione de frammentatzione implementada in Pythia pro s'adronizatzione de su quark b. Su valore prus probàbile est a probe de s'unidade, in sa parte bona de is casos su momentu de s'adrone no istraviat in manera sinnificativa dae su momentu de su quark.

Sa figura 3 mustrat sa distàntzia intre is duos quarks de una croba $b\bar{b}$ e intre

[1] Su *tracking* est unu sistema de reveladores chi recostruent is trajetorias (trassas) de is partìculas càrrigas chi si produent in cunsighèntzia de sa desintregratzione initziale.

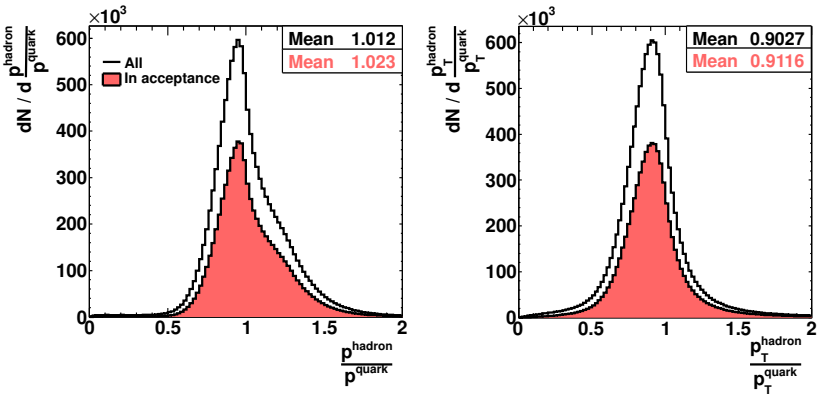

Figure 2: Raportu intre p (p_{T}) de s'adrone B e su quark b currespondente, cando ambosduos sunt in intro de s'atzetàntzia geomètrica de LHCb.

is duos adrones originados dae issos, espressada in tèrminos de sa diferèntzia in s'àngulu azimutale $\Delta\phi$, de sa pseudolestresa (*pseudorapidity*) $\Delta\eta$, e $\Delta\mathrm{R} = \sqrt{\Delta\eta^2 + \Delta\phi^2}$. In custu cuntestu meressit de èssere postu in evidèntzia comente s'adrone B cunservat is propiedades de su quark b.

Su fundu pro custa anàlisi cunsistet in una cumponente fisica, chi a primàrgiu est cumposta dae jets de adrones chi aproghilant dae s'adronizatzione de quarks c e lèbios, e unu fundu cumbinatòriu, dessinidu comente is eventos in ue sa croba $b\bar{b}$ est istada prodùida e s'algoritmu reconstruet jets non fisicamente assotziados a is quarks de sinnale. Sa parte cumbinatòria recheret una definitzione de jets e at a èssere argumentada prus in antis.

Sunt istadas impitadas simulatziones Monte Carlo de eventos $c\bar{c}$ inclusivos in collisiones pp, cun is matessi paràmetros de produtzione de sa produtzione de $b\bar{b}$ inclusivu.

Is figuras 4 e 5 mustrant de pare a pare su momentu e su p_{T} de su quark c e de s'adrone c. sa forma de custas distributziones si cumparat cun is distributziones currespondentes pro quarks e adrones *beauty*. Su momentu travessu de su quark b est prus o mancu su dòpiu de su p_{T} de su quark c. Custa diferèntzia creschet galu de prus in su casu de is adrones. A chircare bèrtighes segundàrios cun p_{T} artu (inoghe nos nche referimus a custos comente *seeds* puru) tenet duncas unu podere de discriminatzione fintzas contra a su fundu de *charm*.

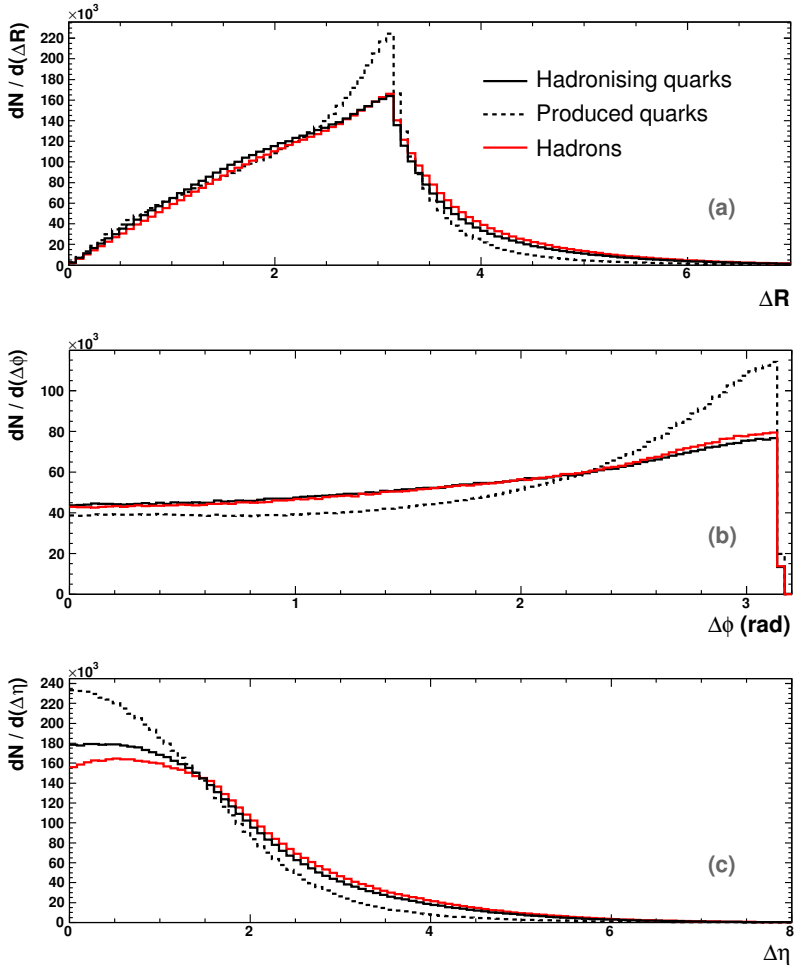

Figure 3: ΔR (a), $\Delta\phi$ (b) e $\Delta\eta$ (c) intre su quark b e su quark $\bar{b}$. In ruju, distributziones pro is crobas de adrones B.

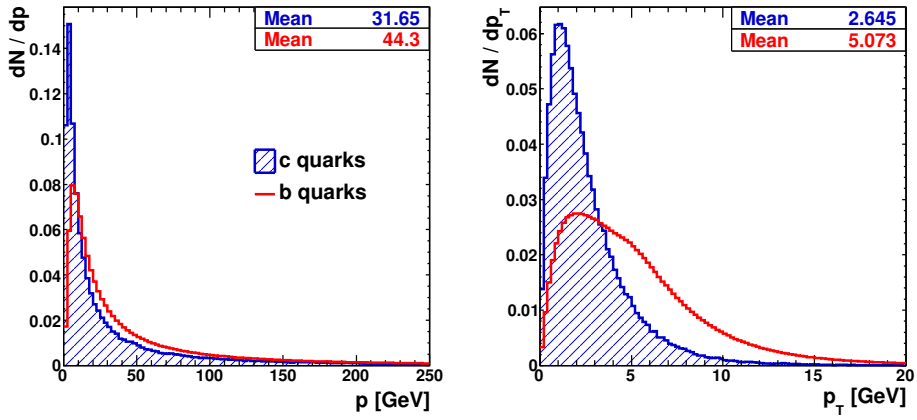

Figure 4: Momentu (p) e momentu travessu (p_{T}) de is quarks c (biaitu) acaradu cun is quarks b.

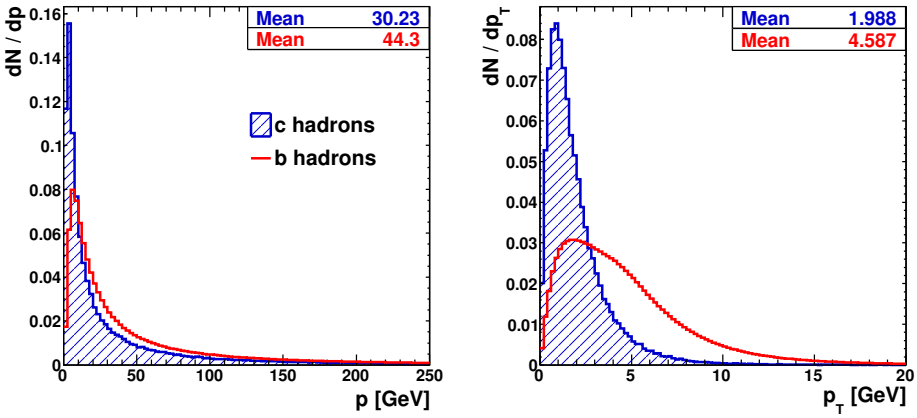

Figure 5: Momentu (p) e momentu travessu (p_{T}) de is adrones c (biaitu) acaradu cun is adrones b.

Seletzione de su sinnale

Acaradu cun àteros isperimentos, su reveladore LHCb tenet una capatzidade estremada de identificare bèrtighes segundàrios istagiados respetu a su puntu de interatzione. Custu est unu resurtadu obligatòriu pro sa finalidade primàrgia sua de istudiare sa violatzione de *CP* in su sistema de is mesones B e est asseguradu dae sa resolutzione arta meda de su Localizadore de Bèrtighes VELO.

LHCb est fintzas capatzu de frunire una mesura pretzisa de is trajetòrias de is partìculas e de is cantidades de movimentu, gràtzias a su sistema de *tracking*. Meda propiedades tzinemàticas de vida pròpia de su decadessimentu de is adrones B sunt sa base pro s'identificatzione de is b-jets (b-*tagging*), in manera chi su reveladore LHCb diat pòdere èssere adecuadu a giùghere istùdios QCD basados a subra de jets dae quarks graes.

Àteras propiedades de is mesones B chi podent èssere impreadas pro su refudu de su fundu sunt sa massa manna sua e sa multiplitzidade de trassa alta in s'istadu finale.

S'aina de *tagging* isvilupada pro identificare is jets chi benint dae s'adronizatzione de su quark b est un'algoritmu de tipu *conu*: s'idea de base est sa de leare unu bèrtighe inclusivu segundàriu chi bèngiat dae un'adrone B comente *seed* (sèmene) pro sa recostrutzione de su jet. Sa positzione de su seed cunforma a su bèrtighe primàrgiu (PV) istabilessit sa diretzione de unu conu de una tzerta abertura. Su jet si recostruet regollende is partìculas càrrigas e nèutras chi s'agatant in intro de su conu. Su ràdiu de su conu s'espressat in tèrminos de su paràmetru adimensionale R_{c}.

Su mètodu est giustificadu fisicamente dae su fatu chi sa massa de su quark b est grae, tando is propiedades de s'adrone B sunt a curtzu de sas de su quark, dipendende prus pagu in su protzessu de frammentatzione respetu a mesuras basadas in canales de decadessimentu esclusivos.

Seletzione de is eventos

Is eventos candidados s'issèberant in primu logu cunforma a sa detzisione de su trigger L0 e HLT. Is eventos impreados sunt atzetados gràtzias a sa presèntzia de una partìcula de momentu travessu e parametru de impatu artos, e seletzionados a livellu de HLT pro sa presèntzia possìbile de unu decadessimentu de adrones B.

Giai chi is datos reales pro s'anàlisi de fisica sunt istados reprotzessados e filtrados peri su protzessu de *stripping*, sunt disponìbile isceti in *streams* chi sunt fileras de lìnias de seletzione esclusivas. S'issèberu pro custa anàlisi

est rutu in manera naturale a subra de su stream numenadu Bhadron. Cun sa finalidade de redùere is intzertesas sistemàticas, isceti unu chemu de lìnias Bhadron est istadu cunsideradu.

Sa seletzione de eventos recheret puru sa recostrutzione de unu bèrtighe primàrgiu isceti, sende custu determinadu dae nessi 5 partìculas càrrigas (si castit [69] pro otènnere prus detàllios a pitzu de sa recostrutzione istàndard de is PV). Custu rechisitu mìnimat in manera sinnificativa s'istadìstica. In càmbiu, refudat eventos in ue b'at prus de un'interatzione pp, in manera de istransire sa dificultade de assinnare is seeds recostrùidos a su PV currespondente.

In fines, a is eventos est rechertu de tènnere a su mancu unu bèrtighe segundàriu recostrùidu.

S'algoritmu de Seeding

Su protzedimentu si basat in sa chirca de crobas de trassas chi forment unu bèrtighe bonu e chi siant cun una tzerta probabilidade parte de is produtos de sa desintegratzione de un'adrone B. Is trassas càrrigas candidadas s'issèberant intre is trassas *long*[1] cun rechisitos subra su momentu travessu, calidade de recostrutzione de is trassas e sinnificàntzia de su paràmetru de impatu respetu a su PV. Is sestos aplicados si resument in sa tàula Tab. 1. Sa bonesa de su bèrtighe recostrùidu est assegurada impitende is sestos mustrados in sa tàula Tab. 2.

	Cut
Track momentum	> 2.0 GeV
Track p_T	> 0.6 GeV
First track χ^2/ndf	< 2.5
Second track χ^2/ndf	< 3.0
IPS wrt PV	> 2.5

Table 1: Sestos impitados pro sa seletzione de is trassas in su protzessu de seeding.

Is seed recostrùidos descrient bene sa diretzione de is adrones B: sa resolutzione ϕ e θ carculada pro is seeds de sinnale resurtat (15.8 ± 0.2) mrad e (1.82 ± 0.18) mrad de pare a pare.

[1]Long tracks: trassas longas, dessinidas comente cussas chi traessant su sistema de tracking intreu.

	Cut
Sum of tracks charge	0
Seed p_T	> 1.0 GeV
$z_{\mathrm{PV}} - z_{\mathrm{SV}}$	> 1 mm
Secondary vertex χ^2/ndf	50
DOCA	< 3 mm
ΔR_{ij}	< 1.4
$\lvert M_{\mathrm{seed}} - M_{K^0_{\mathrm{S}}} \rvert$	$> 10\,\mathrm{MeV}$
$\lvert M_{\mathrm{seed}} - M_{\Lambda} \rvert$	$> 10\,\mathrm{MeV}$

Table 2: Sestos a subra de is bèrtighes segundàrios recostrùidos.

Crobas de seeds recostrùidos chi tenent $\Delta\phi \sim 0$ est meda probàbile chi bèngiant dae sa matessi B o dae sa cadena $B \to D$. Duos seeds si fundent in un'ùnicu seed si sa massa invariante de totu is trassas in is duos seeds est minore de 4.0 GeV. A su seed chi nde resurtat si assinnant is mègius paràmetros possìbiles. Sa fusione de seeds permitet de redùere in manera sinnificativa sa fratzione de seeds farsos chi interessat mescamente sa regione cun $\Delta\phi$ piticu.

Pro costrutzione, su tagging de is adrones B de s'algoritmu de recostrutzione de jets est implìtzitu in su protzedimentu: is bèrtighes segundàrios sunt isseberados tenende in cunsideru is piessinnos chi caraterizant su decadessimentu de su B. s'efitzièntzia de tagging si càrculat impitende su Monte Carlo e si definit comente su raportu intre su nùmeru de seeds de sinnale e su nùmeru de adrones B generados in intro de s'atzetàntzia de LHCb. S'efitzièntzia mèdia de b-tagging agatada est $(59.0 \pm 0.4)\%$.

Recostrutzione de is jets

Sa lìnia de bòlidu de is adrones B est reprodùida cun pretziones bona dae sa positzione de su seed cunforma a su PV. Is jets si costruent summende a su cuadrimomentu de su seed is àteras partìculas càrrigas e nèutras chi s'agatant in intro de unu conu chi s'asse suo cointzidet cun sa trajetòria de su seed. Sa figura 6 mustrat sa massa invariante e su p_{T} de is b-jets, cumparadu cun jets chi benint dae quarks c o lèbios.

In su protzedimentu de recostrutzione de is jets, is trassas annuntiles a printzìpiu sunt lìberas de èssere assinnadas a unu o prus jets, cun sa finalidade de istudiare sa subrapositzione ispatziale e energètica de is jets. In cunsighèntzia, unu critèriu pro fùndere o partzire is jets cheret fissadu. Duos

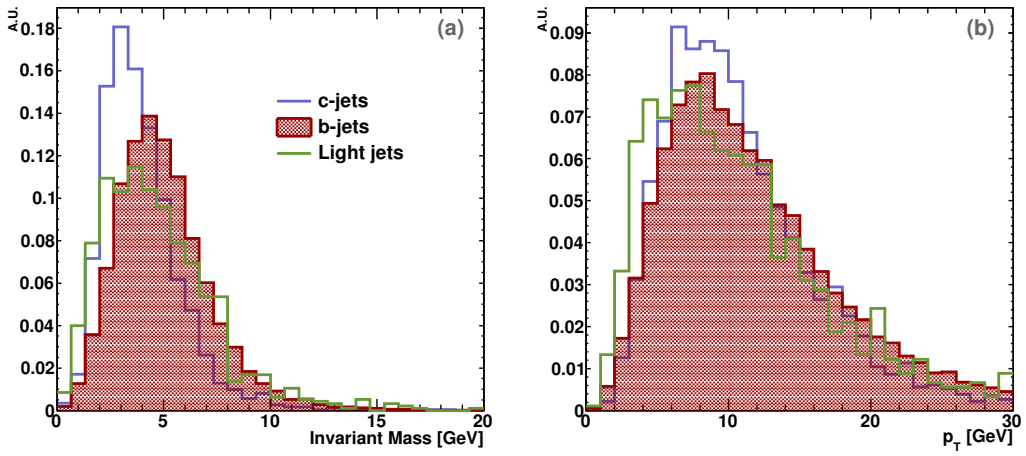

Figure 6: Massa invariante (a) e momentu travessu (b) de is b-jets, c-jets e jets lèbios. Is distributziones sunt normalizadas a sa pròpia area.

jets si fundent in unu isceti si sa fratzione de energia cumpartzida intre issos est $F_{E\text{shared},ij} > 0.4$.

S'ùrtimu passu de su protzedimentu de recostrutzione est s'iscrobadura de is jets: partìculas cumpartzidas dae duos jets in ue balet $F_{E\text{shared},ij} < 0,4$ sunt assinnadas in manera unìvoca a su jet prus a curtzu in ΔR.

Efitzièntzias de trigger e stripping

Duas mustras de sinnale chi cuntenent is eventos cun nessi unu/duos seed recostrùidos si sunt otentas moende dae $\sim$ 6M de eventos MC $b\bar{b}$. S'efitzièntzia de recostrutzione de a su nessi unu/duos seeds dae una mustra de eventos cun unu bèrtighe primàrgiu resurtat èssere:

$$\epsilon_{1\text{seed}} = (18.07 \pm 0.03)\% \quad (2)$$

$$\epsilon_{2\text{seed}} = (3.00 \pm 0.01)\% \ . \quad (3)$$

Is lìnias de trigger L0 prus efitzientes pro is duas mustras de sinnale si demustrant èssere `L0Hadron` e `L0Muon`, tando si sunt impreados eventos atzetados dae custas duas lìnias.

A custos eventos si recheret chi tèngiant resposta positiva pro una de is lìnias `Hlt1Track` de su trigger HLT1. Is lìnias topològicas de su trigger HLT2 sunt istadas isseberadas pro sa seletzione de eventos in sa fase HLT2 de su trigger de livellu artu de LHCb.

S'efitzièntzia globale de su trigger pro is mustras cun nessi unu/duos seeds est:

$$\epsilon_{\text{trigger}}^{\text{1seed}} = (4.09 \pm 0.04)\% \tag{4}$$
$$\epsilon_{\text{trigger}}^{\text{2seeds}} = (11.3 \pm 0.2)\% \ . \tag{5}$$

Sa dipendèntzia de s'efitzièntzia de su trigger dae η si mustrat bastante istàbile in su tretu $\eta \in [2.5, 4.0]$, duncas sa mesura at a èssere alindada a custu tretu in η.

Sende chi non b'at lìnias de stripping dedicadas a s'anàlisi de is b-jets e $\sim 80\%$ de is eventos atzetados dae is lìnias de stripping Bhadron sunt atzetadas dae is lìnias `B2DX*`, custa filera de lìnias est istada impitada in s'anàlisi e si nd'at determinadu s'efitzièntzia cunforma a su nùmeru de eventos atzetados dae su trigger:

$$\epsilon_{\text{stripping}}^{\text{1seed}} = (9.3 \pm 0.3)\% \tag{6}$$
$$\epsilon_{\text{stripping}}^{\text{2seeds}} = (10.6 \pm 0.5)\% \ . \tag{7}$$

Curretzione de s'energia de is jets

In antis de cale si siat cumparatzione intre MC e datos e cun sa finalidade de dissinire unu sestu fidutziàriu in p_{T} de is jets, est pretzisu a aplicare una curretzione de s'energia pro tènnere in contu sa pèrdida de energia pro more de partìculas no reveladas o pro mesuras non curretas de s'energia o de su tracking.

S'idea est sa de calibrare s'energia de is jets impitende jets fraigados a livellu de generadore Monte Carlo. Custos jets si costruent impreende partìculas revelàbiles generadas e leende sa lìnia de bòlidu de su B comente diretzione de su conu. Su raportu intre s'energia de is jets a livellu de generadore e s'energia de is jets recostrùidos ($E_{\text{true}}/E_{\text{jet}}$) est istada currègida cun sa fòrmula:

$$f_{corr}(E_{\text{jet}}) = p_0 + \frac{p_1}{E_{\text{jet}} + p_2} \ , \tag{8}$$

in ue is p_i sunt paràmetros lìberos. S'energia de is jets est istada currègida aplichende sa fòrmula:

$$E_{\text{jet}}^{\text{corr}} = E_{\text{jet}} \cdot f_{\text{corr}}(E_{\text{jet}}) \ . \tag{9}$$

Sa resolutzione de s'energia de is jets currègidos impitente duos valores

diferentes $R_{\mathrm{c}} = 0.7$ e $R_{\mathrm{c}} = 0.8$, resurtat $\sigma_{0.7} = 0.204 \pm 0.008$ e $\sigma_{0.8} = 0.196 \pm 0.008$ de pare a pare.

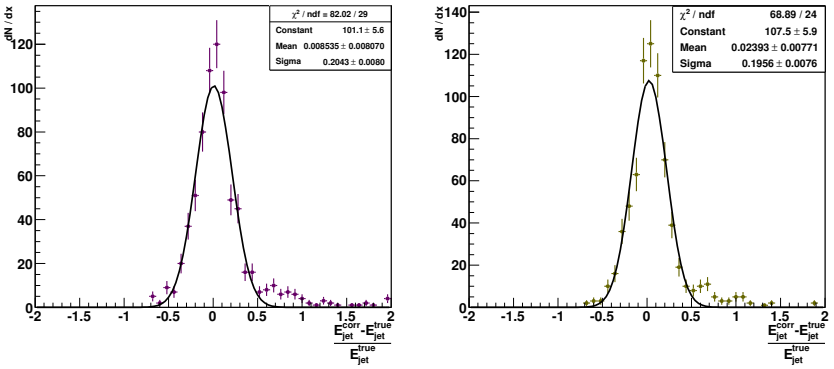

Figure 7: Resolutzione de s'energia de is jets currègidos impitende duos valores diferentes pro su ràdiu de su conu: $R_{\mathrm{c}} = 0.7$ e $R_{\mathrm{c}} = 0.8$.

Resurtados

S'obietivu de s'anàlisi est carculare sa setzione de rugradura de produtzione de crobas $b\bar{b}$ in intro de unu volùmene fidutziàriu (FV) $\eta \in (2.5, 4.0)$ impitende una fòrmula comente sa chi sighit:

$$\sigma_{\mathrm{FV}}^{b\bar{b}} = \frac{N^{\mathrm{obs}} - N^{\mathrm{bkg}}}{\mathcal{L} \times \epsilon^{b\bar{b}}} \ , \tag{10}$$

in ue N^{obs} est su nùmeru de eventos candidados agatados in is datos reales, N^{bkg} est sa summa de is contributziones de is quarks *charm* e lèbios istimadas cun su MC, $\mathcal{L}$ est sa luminosidade integrada de is datos, e $\epsilon^{b\bar{b}}$ est s'efitzièntzia totale de seletzione carculada impreende is simulatziones MC $b\bar{b}$ inclusivas.

Is datos analizados sunt sos collidos in su 2010 cun collisiones a $\sqrt{s} = 7\,\mathrm{TeV}$, pigadas cun duas cunfiguratziones de su trigger simigiantes meda. Sa luminosidade integrada currespondente est $\sim 17.7\,\mathrm{pb}^{-1}$, sa mitade de sa luminosidade totale regorta in su 2010. Sende chi non b'at peruna seletzione dedicada a s'anàlisi de jets, s'estratzione de sa setzione de rugradura est istada realizada impitende eventos seletzionados dae unu nùmeru redùidu de lìnias de stripping de su *stream* Bhadron.

Sunt istados leados in cunsideru petzi is eventos cun unu PV recostrùidu. Sa luminosidade integrada chi resurtat dae custa issèberu est $\mathcal{L}_{\mathrm{eff}} = 2.65\,\mathrm{pb}^{-1}$.

Seletzione finale

Sa seletzione finale aplicada a is datos e a is mustras de MC si podet resùmere in is passos imbenientes:

1. Seletzione de eventos cun unu PV;
2. Recostrutzione de is seeds e seletzione de eventos cun nessi unu seeds reconstrùidu;
3. Trigger e Stripping;
4. Recostrutzione de is jets, in ue is protzessos de fusione e iscrobadura influint in su númeru de jets pro cada eventu;
5. Sestos fidutziàrios: η de is jets $\in (2.5, 4.0)$ e p_{T} de su jet majore de $5\,\mathrm{GeV}$;
6. Seletzione finale de eventos cun pretzisamente duos jets reconstrùidos.

Efitzièntzia de seletzione $\epsilon_{\mathrm{FV}}^{b\bar{b}}$

S'efitzièntzia total de sa seletzione de eventos in ue est istada prodùida una croba $b\bar{b}$ in intro de su FV si podet espressare comente produtu de is efitzièntzias:

$$\epsilon_{\mathrm{FV}}^{b\bar{b}} = \epsilon_{\mathrm{1seed}} \cdot \epsilon_{\mathrm{trigger}} \cdot \epsilon_{\mathrm{stripping}} \cdot \epsilon_{\mathrm{sel}} \ , \tag{11}$$

in ue su tèrmine ϵ_{sel} tenet in contu sa recostrutzione de jets, is sestos fidutziàrios e sa seletzione de eventos cun pretzisamente duos jets recostrùidos. Su valore carculadu pro $\epsilon_{\mathrm{FV}}^{b\bar{b}}$ est

$$\epsilon_{\mathrm{FV}}^{b\bar{b}} = (1.04 \pm 0.12) \times 10^{-4} \ . \tag{12}$$

Cumpositzione de sa mustra de datos seletzionada

Sa cumpositzione de sa mustra de datos seletzionada in tèrminos de cuntènnidu b, c e de quarks lèbios, est istada determinada deretu dae su Monte Carlo. S'efitzièntzia de seletzione de cada genia de fundu est istada carculada in manera simigiante a $\epsilon_{\mathrm{FV}}^{b\bar{b}}$. Is efitzièntzias s'impreant posca pro istimare su nùmeru abetadu de eventos de fundu seletzionados in una luminosidade $\mathcal{L}_{\mathrm{eff}}$, impitende is setziones de rugradura apropiadas. Su nùmeru de eventos $c\bar{c}$ abetadu in intro de FV si càrculat cun sa fòrmula

$$N_{\mathrm{exp}}^{c\bar{c}} = \mathcal{L}_{\mathrm{eff}} \cdot \sigma^{c\bar{c}} \cdot \epsilon_{\mathrm{gen}}^{c\bar{c}} \cdot \epsilon^{c\bar{c}} \ , \tag{13}$$

in ue $\sigma^{c\bar{c}} = 6100\,\mu$b est sa setzione de rugradura in 4π medida dae LHCb [78], $\epsilon^{c\bar{c}}_{\text{gen}}$ est s'efitzièntzia de su sestu de atzetàntzia de su generadore PYTHIA, $\epsilon^{c\bar{c}}$ est s'efitzièntzia de seletzione carculada cun MC $c\bar{c}$ inclusivu. Su nùmeru de eventos abetados pro sa luminosidade $\mathcal{L}_{\text{eff}}$ currespondente a is datos reales s'est istamada in

$$N^{c\bar{c}}_{\text{exp}} \approx 34258 \pm 1489 \ . \tag{14}$$

In manera simigiante s'est carculadu sa contributzione de jets dae quarks lèbios e gluones. Su nùmeru abetadu pro custa casta de eventos est

$$N^{q\bar{q}}_{\text{exp}} \approx 14468 \pm 7837 \ . \tag{15}$$

Càrculu de sa setzione de rugradura

Cun su mètodu adotadu, sa setzione de rugradura de produtzione $b\bar{b}$ in intro de su FV si podet carculare in sa manera chi sighit:

$$\sigma^{b\bar{b}}_{\text{FV}} = \frac{(N^{\text{DATA}}_{\text{obs}} - N^{c\bar{c}}_{\text{exp}} - N^{q\bar{q}}_{\text{exp}}) \cdot p}{\mathcal{L}_{\text{eff}} \cdot \epsilon^{b\bar{b}}_{\text{FV}}} \ , \tag{16}$$

in ue $N^{\text{DATA}}_{\text{obs}} = 87312$ est su nùmeru de eventos seletzionados in is datos reales pigados in su 2010, p est unu fatore chi tenet contu de sa puresa de sa mustra seletzionada. Sa setzione de rugradura medida tando resurtat

$$\sigma^{b\bar{b}}_{\text{FV}} = (80.6 \pm 1.2)\,\mu\text{b} \ , \tag{17}$$

in ue s'errore inditadu est s'istadìsticu.

Errores Sistemàticos

Si sunt avaloradas fontes de errore sistemàticu diferentes, resùmidas in sa tàula 3.

Concruos

Sa setzione de rugradura de produtzione de crobas $b\bar{b}$ in intro de su Volùmene Fidutziàriu resurtat

$$\sigma^{b\bar{b}}_{\text{FV}} = 80.6 \pm 1.2\ (\text{stat}) \pm 11.4\ (\text{syst})\,\mu\text{b} \ . \tag{18}$$

Unu càrculu NLO fatu impitende su generadore POWHEG [81] chi impreat

Font	Intzertesa (%)
Luminosidade integrada	3.5
Setzione de rugradura $\sigma^{c\bar{c}}$	9.0
Sestos globales de s'eventu	0.6
Istadìstica MC	9.0
Efitzièntzia de su trigger e de su stripping	3.0
Multiplitzidade de trassas	3.6
Efitzièntzia de su tracking	1.1
Totale	14.1

Table 3: Fontes de errore sistemàticu.

is PDFs CTEQ6.6 at donadu $\sigma^{b\bar{b}} = (249.8 \pm 0.4)\,\mu$b, in ue s'errore no tenet in contu is intzertesas teòricas. Pro pòdere cumparare sa preditzione, est pretzisu a estrapolare sa mesura a 4π: cunforma a su generadore PYTHIA su fatore est 3.93. Tando sa setzione de rugradura totale resurtat èssere $\sigma^{b\bar{b}} = 316.8 \pm 49.5\,\mu$b. Su resurtadu isperimentale est ~ 1.27 bortas prus mannu de su càrculu teòricu NLO. Un'iscuncordàntzia simigiante intre resurtadu teòricu e isperimentale est istada publicada dae sa collaboratzione CMS [82].

Sa contributzione printzipale a s'intzertesa de sa mesura si depet a s'istadìstica MC: a un'ala s'intzertesa sua intrat deretu in sa mesura peri is efitzièntzias de seletzione basadas in su MC comente flutuatzione istadìstica, a s'àter'ala un'istadìstica prus manna in manera sinnificativa diat permìtere de realizare un'acontzu de is datos pro otènnere is fratziones relativas de sa mustra de datos seletzionada, istransende aici s'impreu de sa setzione de rugradura $\sigma^{c\bar{c}}$, chi tenet intzertesa manna.

In su tempus benidore s'anàlisi at a bogare profetu dae is produtziones imbeniente inclusivas MC11, cun eventos prefiltrados dae su trigger, permitende aici s'atzessu a sa cantidade istremenada de datos leados in su 2011 e 2012. In prus, su reprotzessamentu de datos at a inclùere una lìnia dedicada pro sa seletzione de b-jets inclusivos, reduende aici in manera sinnificativa is intzertesas qui benint dae sa seletzione offline.

Custa megioras permitent de istabilèssere calicunas prospetivas pro su tempus benidore: 1) sa mesura de sa setzione de rugradura diferentziale $\frac{d\sigma^{b\bar{b}}}{dx}$, in ue x podet èssere η, sa massa invariante de is duos jets e $\Delta\phi$; 2) s'istùdiu de is currelatziones angulares intre is duos quarks $b\bar{b}$, chi permitent de iscumbatare is mecanismos de produtzione de is crobas $b\bar{b}$.

Bibliography

[1] ATLAS Collaboration, G. Aad *et al.*, *Observation of a new particle in the search for the Standard Model Higgs boson with the ATLAS detector at the LHC*, Phys. Lett. **B716** (2012) 1, arXiv:1207.7214. 2

[2] CMS Collaboration, S. Chatrchyan *et al.*, *Observation of a new boson at a mass of 125 GeV with the CMS experiment at the LHC*, Phys. Lett. **B716** (2012) 30, arXiv:1207.7235. 2

[3] B.-Q. Ma, *Neutrino Oscillations: from Standard and Non-standard Viewpoints*, Int. J. Mod. Phys. Conf. Ser. **1** (2011) 291, arXiv:1109.5276. 3

[4] A. Franke and C. Mariani, *Review of Reactor Neutrino Oscillation Experiments*, Mod. Phys. Lett. **A27** (2012) 1230010, arXiv:1201.6665. 3

[5] D. A. Petyt, *A Review of Long-Baseline Neutrino Oscillation Experiments*, Acta Physica Polonica B **40** (2009) 2629. 3

[6] P. J. Peebles and B. Ratra, *The cosmological constant and dark energy*, Reviews of Modern Physics **75** (2003) 559, arXiv:astro-ph/0207347. 3, 111, 127

[7] H.-Y. Cheng, *The strong cp problem revisited*, Physics Reports **158** (1988), no. 1 1 . 3, 111, 127

[8] G. Burdman, *New solutions to the hierarchy problem*, Braz. J. Phys. **37** (2007) 506, arXiv:hep-ph/0703194. 3, 111, 127

[9] S. Glashow, *Partial Symmetries of Weak Interactions*, Nucl. Phys. **22** (1961) 579. 4

[10] J. Goldstone, A. Salam, and S. Weinberg, *Broken Symmetries*, Phys. Rev. **127** (1962) 965. 5

[11] P. W. Higgs, *Spontaneous Symmetry Breakdown Without Massless Bosons*, Phys. Rev. **145** (1966) 1156. 5

[12] M. Kobayashi and T. Maskawa, *CP Violation in the Renormalizable Theory of Weak Interaction*, Prog. Theor. Phys. **49** (1973) 652. 5

[13] K. Symanzik, *Small distance behaviour in field theory and power counting*, Communications in Mathematical Physics **18** (1970) 227, 10.1007/BF01649434; C. G. Callan, *Broken scale invariance in scalar field theory*, Phys. Rev. D **2** (1970) 1541. 7

[14] W. E. Caswell and F. Wilczek, *On the Gauge Dependence of Renormalization Group Parameters*, Phys. Lett. **B49** (1974) 291. 7

[15] D. Gross and F. Wilczek, *Ultraviolet Behavior of Nonabelian Gauge Theories*, Phys. Rev. Lett. **30** (1973) 1343. 7

[16] S. R. Coleman and D. J. Gross, *Price of asymptotic freedom*, Phys. Rev. Lett. **31** (1973) 851. 8

[17] S. Bethke, *The 2009 World Average of alpha(s)*, Eur. Phys. J. **C64** (2009) 689, arXiv:0908.1135. 9, 112, 128

[18] K. Chetyrkin, B. A. Kniehl, and M. Steinhauser, *Strong coupling constant with flavor thresholds at four loops in the MS scheme*, Phys. Rev. Lett. **79** (1997) 2184, arXiv:hep-ph/9706430. 10

[19] T. van Ritbergen, J. Vermaseren, and S. Larin, *The Four loop beta function in quantum chromodynamics*, Phys. Lett. **B400** (1997) 379, arXiv:hep-ph/9701390. 10

[20] B. Andersson, G. Gustafson, G. Ingelman, and T. Sjöstrand, *Parton fragmentation and string dynamics*, Physics Reports **97** (1983), no. 2-3 31 . 10, 15, 112, 128

[21] T. Mannel, *Heavy-quark effective field theory*, Reports on Progress in Physics **60** (1997), no. 10 1113. 10

[22] C. Peterson, D. Schlatter, I. Schmitt, and P. M. Zerwas, *Scaling Violations in Inclusive e+ e- Annihilation Spectra*, Phys. Rev. **D27** (1983) 105. 11

[23] A. Efremov and A. Radyushkin, *Factorization and Asymptotical Behavior of Pion Form-Factor in QCD*, Phys. Lett. **B94** (1980) 245. 11

[24] S. Frixione, *Bottom production*, arXiv:hep-ph/0408317. 12

[25] W. Beenakker *et al.*, *QCD corrections to heavy quark production in hadron hadron collisions*, Nucl. Phys. **B351** (1991) 507. 12

[26] T. Sjostrand, S. Mrenna, and P. Z. Skands, *PYTHIA 6.4 Physics and Manual*, JHEP **0605** (2006) 026, arXiv:hep-ph/0603175. 13, 17, 26, 46

[27] M. Cacciari and P. Nason, *Is there a significant excess in bottom hadroproduction at the Tevatron?*, Phys. Rev. Lett. **89** (2002) 122003, arXiv:hep-ph/0204025. 15

[28] B. Webber, *A QCD model for jet fragmentation including soft gluon interference*, Nuclear Physics B **238** (1984), no. 3 492 . 17

[29] G. Corcella *et al.*, *HERWIG 6.5 release note*, arXiv:hep-ph/0210213. 17

[30] CDF II Collaboration, A. Abulencia *et al.*, *Measurement of the inclusive jet cross section using the k(t) algorithm in p anti-p collisions at* $\sqrt{s}$ *= 1.96-TeV.*, Phys. Rev. Lett. **96** (2006) 122001, arXiv:hep-ex/0512062. 18

[31] H1 Collaboration, F. Aaron *et al.*, *Jet Production in ep Collisions at High Q**2 and Determination of alpha(s)*, Eur. Phys. J. **C65** (2010) 363, arXiv:0904.3870. 18

[32] F. Hasert *et al.*, *Observation of neutrino-like interactions without muon or electron in the Gargamelle neutrino experiment*, Physics Letters B **46** (1973), no. 1 138 . 21

[33] G. Arnison *et al.*, *Experimental observation of isolated large transverse energy electrons with associated missing energy at* $\sqrt{s}$ = 540 *GeV*, Physics Letters B **122** (1983), no. 1 103 ; G. Arnison *et al.*, *Experimental observation of lepton pairs of invariant mass around 95* GeV/c^2 *at the CERN SPS collider*, Physics Letters B **126** (1983), no. 5 398 . 21

[34] L. Evans and P. Bryant, *LHC Machine*, JINST **3** (2008) S08001. 22, 113, 129

[35] LHC Higgs Cross Section Working Group, S. Dittmaier *et al.*, *Handbook of LHC Higgs Cross Sections: 1. Inclusive Observables*, arXiv:1101.0593, Long author list - awaiting processing. 22

[36] ATLAS Collaboration, G. Aad *et al.*, *The ATLAS Experiment at the CERN Large Hadron Collider*, JINST **3** (2008) S08003. 24

[37] CMS Collaboration, R. Adolphi *et al.*, *The CMS experiment at the CERN LHC*, JINST **3** (2008) S08004. 24, 25

[38] ALICE Collaboration, K. Aamodt *et al.*, *The ALICE experiment at the CERN LHC*, JINST **3** (2008) S08002. 24, 25

[39] LHCb Collaboration, A. Augusto Alves Jr *et al.*, *The LHCb Detector at the LHC*, JINST **3** (2008), no. S08005 . 25, 113, 130

[40] DELPHI Collaboration, P. Aarnio *et al.*, *The DELPHI detector at LEP*, Nucl. Instrum. Meth. **A303** (1991) 233. 25, 113, 130

[41] LHCb Collaboration, S. Amato *et al.*, *LHCb*, CERN-LHCC-98-04. 26

[42] LHCb Collaboration, R. Aaij *et al.*, *Measurement of* $\sigma(pp \to b\bar{b}X)$ *at* $\sqrt{s} = 7$ *TeV in the forward region*, Phys. Lett. **B694** (2010) 209, arXiv:1009.2731. 27

[43] LHCb Collaboration, P. R. Barbosa-Marinho *et al.*, *LHCb VELO (VErtex LOcator): Technical Design Report*, CERN-LHCC-2001-0011. 28, 29, 32, 114, 131

[44] LHCb Collaboration, S. Amato *et al.*, *LHCb RICH: Technical Design Report*, CERN-LHCC-2000-037. 28, 29, 37, 114, 131

[45] LHCb Collaboration, S. Amato *et al.*, *LHCb Calorimeters*, CERN-LHCC-2000-0036. 28, 30, 39, 114, 131

[46] LHCb Collaboration, R. Antunes-Nobrega *et al.*, *LHCb reoptimized detector design and performance: Technical Design Report*, CERN-LHCC-2003-030. 29

[47] LHCb Collaboration, P. R. Barbosa-Marinho *et al.*, *LHCb inner tracker: Technical Design Report*, CERN-LHCC-2002-029. 29, 34

[48] LHCb Collaboration, P. R. Barbosa-Marinho *et al.*, *LHCb outer tracker: Technical Design Report*, CERN-LHCC-2001-024. 29, 34

[49] LHCb Collaboration, S. Amato *et al.*, *LHCb magnet: Technical Design Report*, CERN-LHCC-2000-007. 29

[50] LHCb Collaboration, P. R. Barbosa-Marinho *et al.*, *LHCb muon system: Technical Design Report*, CERN-LHCC-2001-010. 30, 43

[51] LHCb Collaboration, R. Antunes-Nobrega *et al.*, *LHCb Trigger System Technical Design Report*, CERN-LHCC-2003-031. 30, 43, 77

[52] The LHCb Collaboration, *Roadmap for selected key measurements of LHCb*, arXiv:hep-ex/0912.4179. 31

[53] LHCb-VELO, S. Borghi, *First results from the LHCb vertex locator*, PoS **ICHEP2010** (2010) 030. 34

[54] M. Calvo-Gomez, *Backsplash studies for the SPD subdetector of LHCb*, PoS **HEP2005** (2006) 383. 41

[55] G. Barrand *et al.*, *GAUDI — A software architecture and framework for building HEP data processing applications*, Comput. Phys. Commun. **140** (2001) 45, See also: http://proj-gaudi.web.cern.ch/proj-gaudi/. 46

[56] R. Brun and F. Rademakers, *Root - an object oriented data analysis framework*, in *AIHENP'96 Workshop, Lausanne*, vol. 389, pp. 81–86, 1996. 46

[57] I. Belyaev *et al.*, *Simulation application for the LHCb experiment*, arXiv:physics/0306035, See also: http://lhcb-release-area.web.cern.ch/LHCb-release-area/DOC/gauss/. 46

[58] D. J. Lange, *The EvtGen particle decay simulation package*, Nucl. Instrum. Meth. A **462** (2001), no. 1-2 123. 46

[59] S. Agostinelli *et al.*, *Geant4—a simulation toolkit*, Nuclear Instruments and Methods in Physics Research Section A: Accelerators, Spectrometers, Detectors and Associated Equipment **506** (2003), no. 3 250 . 46

[60] The LHCb Collaboration, *The* Boole *Project*, lhcb-release-area.web.cern.ch/LHCb-release-area/DOC/boole/. 46, 47

[61] The LHCb Collaboration, *The* Moore *Project*, lhcb-release-area.web.cern.ch/LHCb-release-area/DOC/moore/. 47

[62] The LHCb Collaboration, *The* DaVinci *Project*, lhcb-release-area.web.cern.ch/LHCb-release-area/DOC/davinci/. 47

[63] T. Sjostrand, S. Mrenna, and P. Z. Skands, *A Brief Introduction to PYTHIA 8.1*, Comput. Phys. Commun. **178** (2008) 852, arXiv:0710.3820. 55

[64] M. Dobbs and J. B. Hansen, *The HepMC C++ Monte Carlo event record for High Energy Physics*, Computer Physics Communications **134** (2001), no. 1 41 . 55

[65] Torbjorn Sjostrand, *Private communication.* 55

[66] S. Catani *et al.*, *New clustering algorithm for multi - jet cross-sections in e+ e- annihilation*, Phys. Lett. **B269** (1991) 432. 61

[67] M. Cacciari, G. P. Salam, and G. Soyez, *The Anti-k(t) jet clustering algorithm*, JHEP **0804** (2008) 063, arXiv:0802.1189. 61, 73

[68] OPAL Collaboration, R. Akers *et al.*, *QCD studies using a cone based jet finding algorithm for e^+e^- collisions at LEP*, Z. Phys. **C63** (1994) 197. 61

[69] M. Krasowski *et al.*, *Primary vertex reconstruction*, Tech. Rep. LHCb-2007-011. CERN-LHCb-2007-011, CERN, Geneva, Sep, 2007. 64, 99, 119, 136

[70] The LHCb Collaboration, *LHCb Vertex Fitters*, https://twiki.cern.ch/twiki/bin/view/LHCb/VertexFitters. 64

[71] A. Camboni *et al.*, *Measurement of $\sigma(b\bar{b})$ with inclusive b final states in LHCb*, LHCb-ANA-2012-022. 71, 78

[72] G. P. Salam, *Towards Jetography*, Eur. Phys. J. **C67** (2010) 637, arXiv:0906.1833. 71

[73] The LHCb Collaboration, *The Trigger Configuration Key*, https://twiki.cern.ch/twiki/bin/view/LHCb/TCK. 77

[74] M. Williams *et al.*, *The HLT2 Topological Lines*, Tech. Rep. LHCb-PUB-2011-002. CERN-LHCb-PUB-2011-002, CERN, Geneva, Jan, 2011. 78

[75] The LHCb Collaboration, *The TriggerTisTos tool*, https://twiki.cern.ch/twiki/bin/view/LHCb/TriggerTisTos. 78

[76] Y. Amhis *et al.*, *Absolute luminosity measurements at* $\sqrt{s} = 7$ *TeV*, Tech. Rep. LHCb-INT-2011-018. CERN-LHCb-INT-2011-018, CERN, Geneva, May, 2011. 88, 98

[77] The LHCb Collaboration, *LHCb Luminosity Project*, https://twiki.cern.ch/twiki/bin/viewauth/LHCbPhysics/LuminosityMeasurements. 88, 98

[78] The LHCb Collaboration, *Prompt charm production in pp collisions at* $\sqrt{s} = 7$ *TeV*, CERN-LHCb-CONF-2010-013. 96, 99, 125, 142

[79] LHCb Collaboration, R. Aaij *et al.*, *Measurement of charged particle multiplicities in pp collisions at* $\sqrt{s} = 7\,TeV$ *in the forward region*, Eur. Phys. J. **C72** (2012) 1947, arXiv:1112.4592. 100

[80] The LHCb Collaboration, *LHCb Luminosity Project*, https://twiki.cern.ch/twiki/bin/view/LHCb/LHCbTracking. 101

[81] *POWHEG NLO calculation framework*, http://powhegbox.mib.infn.it/. 103, 125, 142

[82] CMS Collaboration, V. Khachatryan *et al.*, *Inclusive b-hadron production cross section with muons in pp collisions at* $\sqrt{s} = 7$ *TeV*, JHEP **1103** (2011) 090, arXiv:1101.3512. 103, 126, 143

[83] The LHCb Collaboration, *LHCb MC10 simulation statistics*, http://lhcb-release-area.web.cern.ch/LHCb-release-area/DOC/STATISTICS/MC10STAT/index.html. 105

[84] The LHCb Collaboration, *LHCb Stripping12*, twiki.cern.ch/twiki/bin/view/LHCb/StreamDefinitionStripping12. 105

[85] The LHCb Collaboration, *LHCb B2DX Stripping lines*, twiki.cern.ch/twiki/bin/viewauth/LHCbPhysics/B2DXStripping. 105